THE HENRYK NIEWODNICZAŃSKI
INSTITUTE OF NUCLEAR PHYSICS
POLISH ACADEMY OF SCIENCES

Application of mono-, bi- and trimetallic gold (Au NPs), platinum (Pt NPs) and palladium-based (Pd NPs) nanoparticles to enhance the proton irradiation effect on cancer cells *in vitro*

mgr inż. Bartosz Klębowski

PhD thesis for the degree of Doctor of Philosophy in physics

Supervisors:

prof. dr hab. inż. Magdalena Parlińska-Wojtan

dr hab. Jarosław Baran, prof. UJ CM

Auxiliary supervisor:

dr inż. Joanna Depciuch

Kraków, 2022

Acknowledgements

First of all, I would like to express my gratitude to my Supervisors: prof. dr hab. inż. Magdalena Parlińska-Wojtan, dr hab. Jarosław Baran, prof. Jagiellonian University Medical College and dr inż. Joanna Depciuch for introducing me to the world of science and invaluable help at every stage of my research. Scientific work under Your supervision is a pleasure !

A special thanks to those of you who helped me in my research, especially prof. dr hab. Jerzy Mietelski, dr Agnieszka Panek, mgr inż. Wiktor Komenda and mgr inż. Dawid Krzempek from Institute of Nuclear Physics Polish Academy of Sciences and Dr Małgorzata Stec from Jagiellonian University Medical College.

My gratitude goes also to the all my colleagues from the Division of Condensed Matter Physics and from the Department for Functional Nanomaterials for your indescribable support.

I would like to express my special gratitude to my family and friends, who motivated and supported me, also in these difficult times.

Table of contents

Abstract

Cancers are one of the most common, life-threatening civilization diseases. Unfortunately, currently available treatment methods such as surgery, chemo-, radio- or even targeted immunotherapy often do not give satisfactory results. Therefore, it is extremely important to find new, more effective strategies to fight cancer. Consequently, taking from one side an anticancer therapy that may save normal cells and tissues, and recent developments of nanotechnology from the other, in this dissertation a potential enhancement of antitumor effect of proton beam irradiation (PIr) using noble metal nanoparticles (NPs) was investigated. For this purpose, mono-, bi- and trimetallic NPs composed of atoms with high-Z number (gold – Au NPs, platinum – Pt NPs, palladium – Pd NPs) were synthesized and added to the cultures of cancer and non-cancer reference cell lines, to find out, if a higher PIr effect can be achieved, in comparison with the same irradiation dose, but without the presence of NPs. Hence, an ***interdisciplinary approach was presented, where the knowledge of the chemical preparation of NPs and their growth mechanisms were combined with the physical properties of the obtained nanostructures having a direct biological effect on the cells. This study tries to answer the question, which of the mechanisms: chemical-biological or physical, is responsible for the increased death of cancer cells cultured with NPs and irradiated with a proton beam***. Moreover, in this dissertation a large number of physical, chemical and biological methods, including charged-particle (proton) activation analysis (ChPAA), transmission electron microscopy (TEM), energy-dispersive X-ray spectroscopy (EDS), selected area electron diffraction (SAED), X-ray diffraction (XRD), ultraviolet-visible (UV-Vis) spectroscopy, zeta potential measurement, nanoparticle tracking analysis (NTA), 3D holotomographic microscopy, MTS (3-(4,5-dimethylthiazol-2-yl)-5-(3-carboxy-methoxy-phenyl)-2-(4-sulfophenyl)-2H-tetrazolium) test and flow cytometry were used to verify the research hypotheses that had been set.

Au NPs, Pt NPs, Pd NPs and bi- or ternary combinations of these NPs were laboratory synthesized using wet chemistry methods. The NPs were chosen on the basis of properties such as: high-Z number, size below 50 nm, crystalline structure and used stabilizers. The obtained NPs were added to the cultures of three colon cancer cell lines with different aggressiveness and metastatic potential to determine, what kind of NPs possess the most pronounced cytotoxicity against cancer cell after PIr. Furthermore, long term, non-invasive, real-time observations of NPs accumulation dynamics in cells were performed using a 3D holotomographic microscopy (Nanolive). Importantly, to show the combined effect of NPs and PIr on the cells, first, by cell viability assessment (MTS test), the non-toxic NPs concentrations and non-destructive proton beam dose for each cell line were determined. In both cases the threshold was below 20 % of dead cells. Next, the NPs, in the established concentrations, were added to the cultures of the respective cell lines, which were subsequently irradiated, and checked for cell viability (MTS test and flow cytometry analysis of Annexin-V binding).

The obtained results showed, that PIr of cells cultured with NPs resulted in a better cytotoxic effect against cancer cells, when compared to PIr without NPs. This observation confirmed the purpose and effectiveness of applying nanoradiosensitizers in anticancer

therapies. However, the final effect of combined PIr seems not to be dependent on the type of the metal used, but rather on the size and nanostructure (porosity) of the NPs. It was shown that ultra-small Pt NPs and Pd NPs possessed the strongest radiosensitizing effect compared to the others. The small size of NPs provides a highly developed surface area, and thus – more effective radiosensitizing properties. In this context, the ultra-small Pd NPs seem to be the most promising radiosensitizers, as their maximum non-toxic concentration was lower than for ultra-small Pt NPs, and the final cytotoxic effect of Pd NPs on cancer cells was similar to Pt NPs. The effect of NPs porosity was compared using two AuPd NPs structures: AuPd CSs with continuous palladium shell, and AuPd nano-raspberries (AuPd) NRs coated by a porous palladium shell. Importantly, both NPs had a similar outer diameter, consisted of the same metals, and were also obtained using the same reagents and synthesis method. Clearly better radiosensitizing properties were shown for porous AuPd NRs, which provide a highly developed surface and thus a better contact with cells. 3D holotomographic images showed, that the NPs penetrate the cells and locate in the nucleus. In all cell lines studied, the cellular volume occupied by Pd NPs increased linearly with time of culture, albeit with different, cell specific, magnitude - being most pronounced for the SW620 cells. This means, that the absorption dynamics of the Pd NPs was different for the respective cell lines. ***Very important finding for medical applications, is that cells from all three cancer cell lines were more sensitive to PIr, NPs and combined actions of PIr and NPs, compared to normal cells.***

Finally, the mechanisms leading to cell death induced by NPs addition and proton beam irradiation were studied. The results of the ChPAA showed that the gamma radiation, characteristic for nuclides/isotopes, which could arise from a nuclear reaction of gold, platinum or palladium, was not observed, suggesting, that ***the physical effect of radiosensitization is likely to play a negligible role in the cell death***. Therefore, it is hypothesized that radiosensitization involves rather the biological-chemical effect of e.g. generating reactive oxygen species (ROS) and/or inhibiting the cell cycle in the G2/M phase, when the cells are most radiosensitive.

Summarizing, in the dissertation, the enhancement of the irradiation effect of proton beam on cancer cells by the use of noble metal NPs was documented and analyzed in relation to the size, structure, chemical compositions and value of zeta potentials of NPs. It has been shown, which of the radiosensitization mechanisms play a major role in causing cell death, in particular of cancer cells, cultured with NPs and after PIr. The obtained results show that the synthesized NPs added in non-toxic concentration to cancer cell lines significantly improve the anticancer effect induced by irradiating them with the proton beam only.

Streszczenie

Nowotwory należą do jednych z najczęstszych i najbardziej zagrażających życiu chorób cywilizacyjnych. Niestety, dostępne metody leczenia, takie jak chirurgia, chemioterapia, radioterapia, a nawet immunoterapia często nie dają satysfakcjonujących rezultatów. W związku z tym, niezmiernie ważne jest znalezienie nowych, bardziej efektywnych strategii zwalczania nowotworów. W niniejszej rozprawie doktorskiej zbadano wzmocniony, przeciwnowotworowy efekt napromieniania wiązką protonów (PIr) w obecności nanocząstek, będący rezultatem terapii wykorzystującej rozwój nanotechnologii i niepowodującej wyraźnych uszkodzeń prawidłowych komórek i tkanek, z jednoczesnym działaniem przeciw-nowotworowym. W tym celu zsyntezowano mono,- bi- oraz trimetaliczne nanocząstki (NPs) zbudowane z atomów o wysokiej liczbie atomowej Z (złota – Au NPs, platyny – Pt NPs, palladu – Pd NPs), które dodawano do rakowych oraz referencyjnych linii komórkowych, aby wykazać czy osiągnięty zostanie lepszy efekt PIr w porównaniu do PIr o takiej samej dawce promieniowania, ale bez dodatku NPs do komórek. Zatem, *w niniejszej rozprawie wykorzystano interdyscyplinarne podejście, w którym wiedzę o chemicznej syntezie nanocząstek oraz mechanizmach ich wzrostu połączono z właściwościami fizycznymi otrzymanych nanostruktur mającymi bezpośredni efekt biologiczny na komórki. Badania te miały odpowiedzieć także na pytanie, jaki mechanizm: chemiczno-biologiczny czy fizyczny jest odpowiedzialny za zwiększenie śmiertelności komórek rakowych hodowanych z NPs i naświetlanych wiązką protonów*. W rozprawie doktorskiej zastosowano wiele fizycznych, chemicznych i biologicznych metod w celu zweryfikowania zawartych w pracy hipotez: analizę aktywacyjną cząstkami (protonami) naładowanymi (ChPAA), transmisyjną mikroskopię elektronową (TEM), spektroskopię dyspersji energii promieniowania rentgenowskiego (EDS), dyfrakcję elektronową wybranego obszaru (SAED), dyfrakcję rentgenowską (XRD), spektroskopię w zakresie nadfioletu i światła widzialnego (UV-Vis), pomiar potencjału zeta, analizę śledzenia nanocząstek (NTA), mikroskopię holotomograficzną 3D, test MTS (sól 3-(4,5-dimetylotiazol-2-ylo)-5-(3-karboksymetoksyfenylo)-2-(4-sulfofenylo)-2H-tetrazolowa) oraz cytometrię przepływową.

W warunkach laboratoryjnych otrzymano metodą mokrej syntezy monometaliczne Au NPs, Pt NPs, Pd NPs oraz bi- i trójskładnikowe kombinacje tych NPs. Wyżej wymienione rodzaje NPs zostały wybrane ze względu na ich właściwości, takie jak wysoka liczba atomowa Z, rozmiar poniżej 50 nm, krystaliczna struktura oraz odpowiednio dobrane stabilizatory. Otrzymane NPs były dodawane do hodowli trzech linii komórkowych raka jelita grubego, cechujących się różną agresywnością i potencjałem przerzutowania, aby określić, który rodzaj NPs powoduje największą cytotoksyczność po PIr. Następnie przeprowadzono długoterminowe obserwacje komórek w czasie rzeczywistym, stosując nieinwazyjną technikę mikroskopii holotomograficznej 3D (Nanolive), uzyskując informacje na temat miejsc akumulacji NPs oraz spowodowanych akumulacją zmian gęstości NPs we wnętrzu komórek. Do wykazania kumulatywnego efektu NPs oraz PIr względem komórek, w pierwszym etapie za pomocą testu MTS wyznaczono nietoksyczne stężenia poszczególnych rodzajów NPs oraz dawki promieniowania protonowego dla wszystkich linii komórkowych. W obu przypadkach dopuszczalnym progiem było stężenie/dawka, które powodowało

śmiertelność nie wyższą niż 20 % komórek. Następnie, NPs w takim wyznaczonym stężeniu dodawano do hodowli do odpowiednich linii komórkowych, które następnie naświetlono, po czym w różnych odstępach czasu oceniono ich żywotność za pomocą testu MTS oraz cytometrii przepływowej.

Wyniki badań pokazały, że PIr komórek hodowanych z NPs daje większy efekt cytotoksyczny, w porównaniu do PIr bez wykorzystania NPs. Potwierdza to celowość i skuteczność stosowania nanoradiouczulaczy w terapiach antynowotworowych. Jednakże, końcowy efekt PIr zależy nie tyle od rodzaju metalu wchodzącego w skład NPs, ale bardziej od rozmiaru oraz nanostruktury (porowatości) NPs. Wykazano, że ultra małe Pt NPs oraz Pd NPs mają lepsze właściwości radiouczulające w porównaniu do pozostałych NPs. Niewielki rozmiar NPs zapewnia silnie rozwiniętą powierzchnię, a co za tym idzie – warunkuje lepsze właściwości radiouczulające. Najbardziej obiecujące wydają się tu ultra małe Pd NPs, gdyż maksymalne nie-toksyczne stężenie tych NPs było mniejsze niż ultra małych Pt NPs, a końcowy efekt działania Pt NPs i Pd NPs był zbliżony. Porównano także efekt porowatości dwóch struktur AuPd typu rdzeń-otoczka: AuPd CSs z ciągłą palladową otoczką oraz nanomalin (AuPd NRs) z porowatą palladową otoczką. Istotne jest, że oba typy NPs mają zbliżoną zewnętrzną średnicę, składają się z tych samych metali oraz to, że zostały otrzymane za pomocą takich samych reagentów w analogicznej metodzie syntezy. Wyraźnie lepsze właściwości radiouczulające wykazano dla porowatych AuPd NRs, co jest spowodowane przez silniej rozwiniętą powierzchnię tych NPs, co zapewnia lepszy kontakt z komórkami. Zdjęcia z mikroskopii holotomgraficznej 3D pokazały, że Pd NPs akumulują się w jądrach komórkowych. Dla wszystkich badanych linii komórkowych objętość zajmowana przez NPs w komórkach wzrastała liniowo wraz z czasem hodowli i zależała od linii komórkowej – najbardziej widoczne zmiany zaobserwowano dla linii SW620. Oznacza to, że dynamika wnikania Pd NPs była różna dla poszczególnych linii komórkowych. ***Ważnym dla zastosowań medycznych jest fakt, że komórki wszystkich linii nowotworowych były bardziej wrażliwe na PIr, NPs oraz łączoen działanie PIr z NPs, w porównaniu z komórkami prawidłowymi.***

Zbadano także mechanizmy interakcji komórek z wiązką protonów i NPs, które prowadzą do śmierci komórek. Wyniki ChPAA wykazały, brak występowania promieniowania gamma charakterystycznego dla nuklidów/izotopów, które mogłyby powstać w wyniku reakcji jądrowej na złocie, platynie lub palladzie, co sugeruje, ***że fizyczny efekt radiouczulania pełni znikomą rolę w śmierci komórek.*** W tym kontekście należy oczekiwać, że w radiouczulanie zaangażowany jest głównie efekt biologiczno-chemiczny opierający się na generowaniu m.in. reaktywnych form tlenu (ROS) i/lub hamowaniu podziałów komórki w fazie G2/M, w której komórki cechują się najwyższą wrażliwością na promieniowania.

Podsumowując, w niniejszej rozprawie sprawdzono wpływ rozmiaru, struktury, składu chemicznego oraz wartości potencjału zeta NPs na wzmacnianie efektu napromieniowania komórek rakowych oraz prawidłowych. Wykazano, który mechanizm radiouczulania pełni kluczową role w indukcji śmierci komórek nowotworowych, poddanych działaniu NPs oraz PIr. Uzyskane wyniki pokazały, że dodatek zsyntezowanych NPs w nietoksycznym stężeniu do komórek nowotworowych, znacząca zwiększa ich śmiertelność na skutek oddziaływania NPs z wiązką protonów.

List of abbreviations

ANOVA – Analysis of Variance
ATP – Adenozine Triphosphate
BNCT – Boron Neutron Capture Therapy
ChPAA – Charged-Particle Activation Analysis
CTAB – Cetyltrimethylammonium Bromide
CNR – Coulomb Nanoradiator
DMEM – Dulbecco's Modified Eagle Medium
DNA – Deoxyribonucleic Acid
DSBs – Double-Strand Break
EDS – Energy–Dispersive X-ray Spectroscopy
EMEM – Eagle's Minimum Essential Medium
FACS – Fluorescence-Activated Cell Sorting
FBS – Fetal Bovine Serum
fcc – face-centered cubic
FEG – Field Emission Gun
FITC – Fluorescein Isothiocyanate
FSD – Forward Scatter Detector
HAADF – High-Angle Annular Dark-Field
HR(S)TEM – High Resolution-(Scanning) Transmission Electron Microscopy
HPGE – High Purity Germanium
LET – Linear Energy Transfer
MTS – 3-(4,5-dimethylthiazol-2-yl)-5-(3-carboxymethoxyphenyl)-2-(4-sulfophenyl)-2H-tetra-zolium
MRI – Magnetic Resonance Imaging
NIR – Near-Infrared
NTA – Nanoparticle Tracking Analysis
NPs – Nanoparticles
NPs-PIr – Nanoparticle-Assisted Proton Irradiation (defined as irradiation with 225 MeV proton beam with a total dose of 15 Gy of cell lines cultured with the synthesized NPs. After irradiation the cells were cultured for another 18 h and subsequently all tests were performed)
PBS – Pencil Beam Scanning
PCR-ELISA – Polymerase Chain Reaction-Enzyme Linked Immunosorbent Assay
PD – Photodynamic Therapy
PEG – Polyethylene Glycol
PI – Propidium Iodide
PIr – Proton Beam Irradiation
PS – Phosphatydyloserine
PT – Proton Therapy
PTT – Photothermal Therapy
RBE – Relative Biological Effectiveness
RI – Refractive Index
ROS – Reactive Oxygen Species

SAED – Selected Area Electron Diffraction
SSBs – Single-Strand Break
SSD – Side Scatter Detector
(S)TEM – (Scanning) Transmission Electron Microscopy
UV-Vis – Ultraviolet-Visible
XRD – X-Ray Diffraction

Introduction

There is no doubt that cancers are one of the biggest challenges for current medicine – in 2020 about 10 million people died from cancers worldwide [1]. For many types of cancer, surgical interventions are ineffective. In turn, radio- or chemotherapy alone, have limited possibilities, because cancer cells relatively often quickly become resistant to this type of treatment [2]. What is more, such a treatment is also harmful to normal tissues, which is often associated with severe side effects [3]–[5]. On the other hand, immunotherapy although characterized by selectivity of action, is not a routine form of the treatment and still has limited effectiveness.

Recently, a high hope is proton radiotherapy (PT), which gives the possibility to precisely irradiate the tumor, even in hard-to-reach locations in human body. The specificity of the proton beam makes it possible to minimize the side effects, because most of the radiation dose goes directly to the tumor, sparing the surrounding normal tissues [6]. Protons interacting with water, the main component of cells cause its radiolysis. As a result, reactive oxygen species (ROS) are created, which destabilize DNA (deoxyribonucleic acid), leading to cell apoptosis. The effectiveness of PT can be further enhanced by using so-called nanoradiosensitizers, which are added at non-toxic concentrations into the cancer cells, to render them more sensitive to subsequent irradiation. These radiosensitizers, interacting with the proton beam, also generate ROS and consequently disrupt the life cycle of cancer cells [7], [8].

Among the various types of NPs, noble metal NPs possess the greatest potential as radiosensitizers. These NPs are biocompatible, stable, allow to functionalize their surface and are easy to synthesize (often without the need of using organic solvents) [9]. It is already known that the radiosensitizing properties of synthesis method [10]–[12]. By far, the most common NPs used as radiosensitizers in radiation-based anticancer therapies (e.g. X-ray radiotherapy, PT, photothermal- or photodynamic therapy) are gold nanoparticles (Au NPs) [13]–[17]. Despite having undoubted benefits e.g. large surface, simplicity to obtain Au NPs with different sizes and shapes, and excellent photothermal properties, a significant disadvantage is the high cost of synthesis of such NPs (high price of the gold precursor – chloroauric acid). For this reason, it is important to find new noble metal based nanoradiosensitizers with a lower production cost.

Motivation

This doctoral thesis is realized in the frame of the InterDokMed Program, which is assumed to be interdisciplinary under the guidance of two co-supervisors from two different fields. Thus, the performed research connects the fields of physics and medical biology into a study of physical properties of NPs investigated by physical techniques, and their effect after being added to culture of cancer cells – analyzed by biological methods.

Carrying out a thorough literature review, it was shown that effective radiosensitizers can be, among others, platinum (Pt NPs) and palladium (Pd NPs)-based nanomaterials, because their potential application in other branches of biomedicine has been documented [18]–[23].

In particular, Pd NPs are interesting because their production cost is several times lower than the production of Au NPs. In addition, so far only one paper on the application of Pd NPs, as potential radiosensitizers in X-ray radiotherapy has been published [24]. However, there is no information in the literature on the use of Pd NPs as radiosensitizers in PT. Thus, as part of the PhD thesis, it was planned to obtain ultra-small (≈ 2-3 nm) Pd NPs and Pt NPs, as well as spherical ≈ 16 nm Au NPs and compare their radiosensitizing performance. Moreover, due to the growing use of multicomponent NPs in medicine [25]–[27], it seemed interesting to assess the potential of bimetallic (AuPd and AuPt) and ternary (AuPdPt) NPs, and compare their radiosensitizing effectiveness with monometallic NPs. Importantly, multicomponent NPs had a gold core (also ≈ 16 nm) covered with ultra-small palladium and/or platinum. Moreover, an unexplored aspect is the effect of the porosity of such NPs, so in this thesis it was also decided to compare radiosensitizing properties of the two types of AuPd nanostructures with different porosity of the palladium shell. An important issue was to establish, if the effect of increased mortality of cancer cells after PIr in the presence of NPs occurs, and if so, is it related to the generation of ROS (biological effect) or, is it also a physical effect, related to nuclear reactions, occurring in metal NPs, induced by the interaction with the proton beam.

This dissertation has been divided into six main parts. The first chapter, entitled „**Literature review**", discusses the basics of nanotechnology, with a particular focus on noble metal NPs. The synthesis methods of these NPs and properties, determining their application in biomedicine have been also discussed. Next, the Reader is introduced to the topics of cancer development and radiation-based anticancer therapies, with particular emphasis on the physical basis of PT and the interaction of proton beam with noble metals. At the end of this chapter, the noble metal nanosystems, studied so far for enhancing the effect of cancer radiotherapy have been discussed. The second chapter, „**Materials and methods**" contains detailed information about the synthesis of NPs, and a description of all research techniques used in this study. The third chapter, „**Results**" is divided into two parts: the physical and the biological one. The first, presents physical characterization of the synthesized mono-, bi-, and trimetallic NPs based on gold, platinum and palladium. Furthermore, aspects of the nuclear reactions induced by proton beam in the NPs are presented. The combination of physics and biology is done by real-time observations of living cells and their interaction with NPs. The accumulation of the latter ones in cancer cells has been analyzed using a cutting-edge, first instrument in Poland, the Nanolive 3D holotomographic microscopy. In the biological part of this chapter the results of the anticancer effect caused by PIr, NPs and PIr combined with NPs have been presented and discussed. The fourth chapter, „**Discussion**", explains the obtained results, comparing them with other reports. Then, the obtained results have been summarized and the conclusions provided („**Summary and conclusions**"). Lastly, „**Supplementary information**" containing additional data (figures and tables) on the carried out experiments is presented.

Chapter 1: Literature review

1.1. Gold, platinum, palladium, mono, bi-, and trimetallic NPs: synthesis, properties and interaction with living cells

1.1.1. Synthesis methods of NPs

NPs are defined as materials ranging in size from 1-100 nm, although some definitions extend the upper size limit to 1000 nm (1 µm) [28], [29]. In order to obtain NPs of a desired size, shape, chemical composition, it is necessary to manipulate the parameters of the NPs synthesis reaction. The selection of the correct reagents, temperature, pH, time etc. is crucial to obtain NPs for a dedicated application.

There are two stages of NPs synthesis: **nucleation** and **growth**. During nucleation, the seeds (nuclei) are templates for crystal growth. In this process, zero-valence atoms are formed, as a result of breaking the bonds of the used metal precursor. Next, these atoms collide with each other to form clusters (so-called nuclei). In the event that these nuclei overcome the energy barrier, they will be able to continue their growth [30]. For spherical shape of the nuclei, nucleation can be described as follows:

$$\Delta G = 4\pi r^2 \gamma + \frac{4}{3}\pi r^3 \Delta G_v \qquad (1)$$

where ΔG – crystal free energy; r – radius of the particle; γ – surface energy and ΔG_V – free energy of the bulk crystal, which is defined in equation (2):

$$\Delta G_v = \frac{-k_B T \ln(s)}{v} \qquad (2)$$

where: T – temperature; k_B – Boltzmann constant; S – supersaturation of the solution; v – molar volume of the solution.

Considering that γ is always positive and ΔG – negative, it is possible to determine the non-toxic free energy (ΔG_{crit}), assuming that $d\Delta G/dr = 0$ (equation 3).

$$\Delta G_{crit} = \frac{4}{3}\pi r_{crit}^2 \qquad (3)$$

wherein r_{crit} is the minimum size of the particle in the solution, which will not be redissolved.

Generally, the NPs growth process consists of two stages: diffusion, taking place according to Fick's first law (equation 4) and the surface process, in which the incorporation of growth species into the solid structure occurs.

$$J = 4\pi x^2 D \frac{dC}{dX} \qquad (4)$$

where J – is the flux of growth species passing through a spherical surface with radius x; D – diffusion coefficient; C – concentration.

At the steady state (J = const.) the above equation takes an approximate form, where δ is the thickness of the diffusion layer; C_b – supersaturated growth species concentration; C_i – growth species concentration at the particle interface; r – radius of particle.

$$J = \frac{4\pi D r(r+\delta)}{\delta}(C_b - C_i) \qquad (5)$$

And the flux is equal to the consumption rate of the growth species at the surface of the particles:

$$J = 4\pi r^2 k_d(C_i - C_r) \qquad (6)$$

where k_d – rate constant of a simple first order deposition reaction; C_r – solubility of the particle with a radius r [31].

There are many methods of producing noble metal NPs. Generally, the NPs synthesis methods can be divided into **bottom-up** (or **wet chemistry methods**) and **top-down** methods. Both methods are compared in Figure 1.
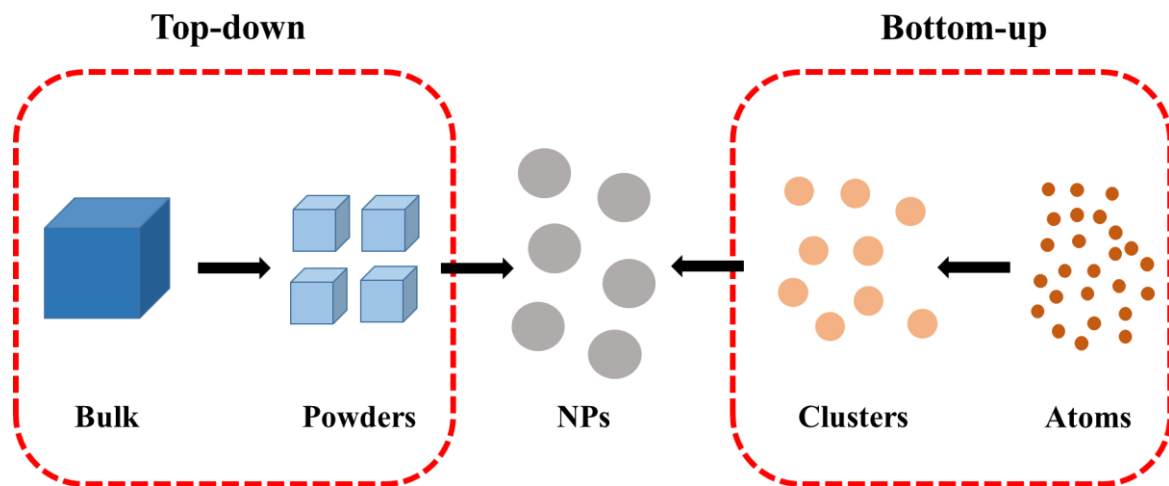
Figure 1. *General scheme of top-down and bottom-up synthesis of NPs. Modifed from* [32]*.*

Top-down is a physical method of obtaining NPs by reducing the seed size and grinding of particles into nanosized materials. Top-down techniques include e.g. sputtering, chemical etching, thermal or laser ablation and explosion process [33]. Conversely to the top-down techniques, in the bottom-up methods, NPs are synthesized by means of chemical reactions among the atoms, ions or molecules. In the present study, only simple wet chemistry synthesis methods were used, thus only those are described in the ,,Materials and Methods'' section. Bottom-up methods enable the control of the NPs growth and controlled obtaining of NPs with a specific morphology. The most common wet methods for NPs preparation are briefly discussed below.

1) **Sol-gel** – is the method where during the synthesis of NPs, the precursor of NPs is transformed into a ,,sol'' and subsequently into a network structure called ,,gel''. Then, during the aging process, water and organic solvents are removed from the gel, followed by a calcination process to obtain dried NPs (Figure 2). In the first stage, the **hydrolysis** of the precursors takes place in the presence of oxygen, which

is supplied by water or organic solvents. This process is finished and aqueous- or non-aqueous sol-gel, depending on the used solvent is obtained. The next stage is **condensation**. At this stage, adjacent molecules condense, water or alcohol is eliminated, metal oxide bonds are formed and polymeric networks grow to colloidal dimensions in the liquid state. Finally, condensation increases the viscosity of solvent forming a porous structure containing a liquid phase, called gel. Then, in the **aging** process, continuous changes in the structure of the gel occur. There is a decrease of porosity and thickness increase of the colloid containing particles. The **drying** process is complex, because water and organic phase are detached to form gel, disturbing its structure. Various drying processes can be distinguished: supercritical drying, thermal drying and freeze drying, having different implications on the structure of the gel network. Finally, thanks to drying process, it is possible to obtain aerogel, xerogel or cryogel. The final step is calcination, which allows to remove water particles or other undesirable residues. The disadvantage of this method is undoubtedly the multi-stage synthesis process, during which it is often necessary to use organic solvents. It can only be used to obtain metal oxide NPs. Furthermore, there is often a large volume shrinkage and cracking during drying process [34].
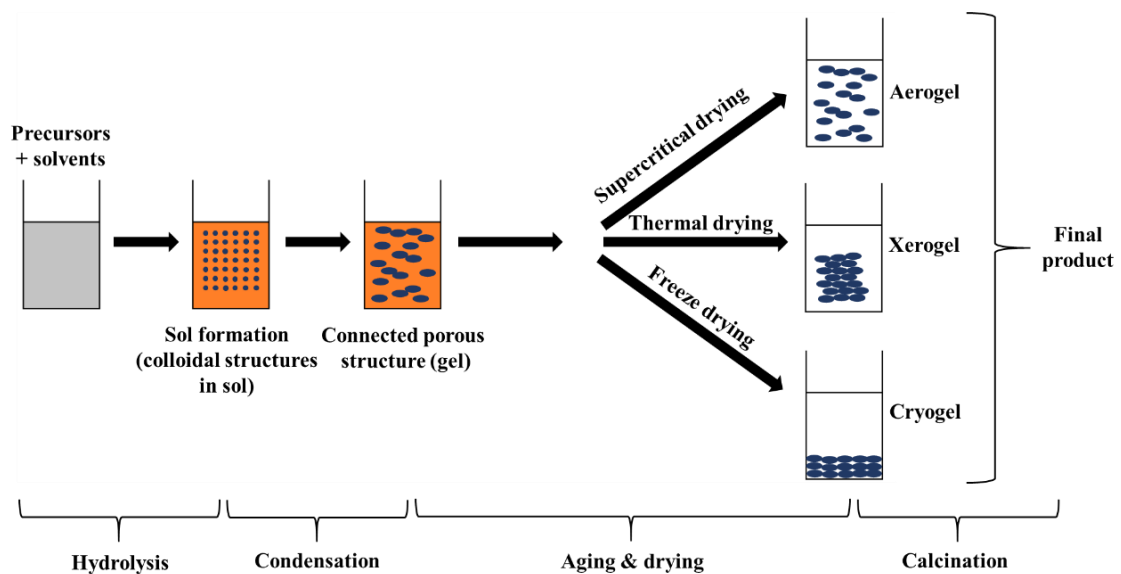

Figure 2. *Sol-gel process to synthesize NPs. Modified from* [35].

2) **Microemulsion -** in this method, two microemulsions containing a precursor (metal salt) and a reducing agent are mixed (Figure 3). After that, there is an exchange of reagents between the micelles during the collision of water droplets resulting, among others, from Brownian motions and Van der Waals forces [36]. These collisions lead to coalescence, fusion and efficient mixing of the precursor and metal salt, resulting in the formation of metal nuclei.
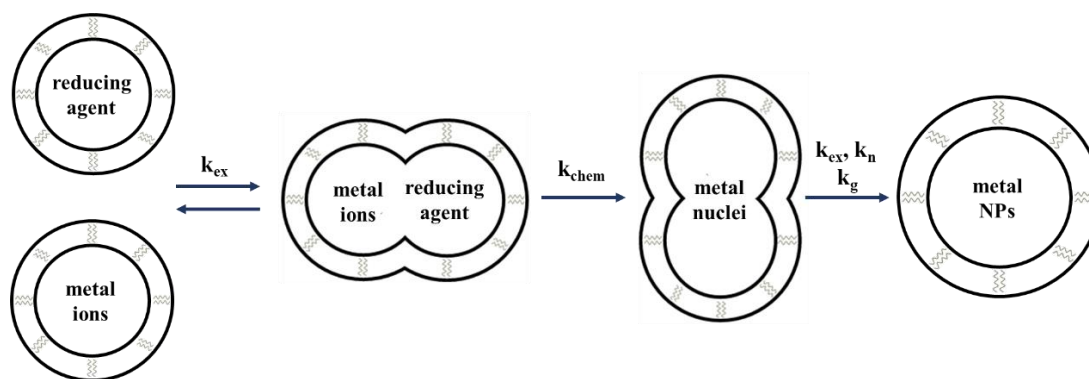
Figure 3. *Scheme of NPs synthesis using microemulsion techniques. k_{chem} – the rate constant for chemical reaction; k_{ex} – the rate constant for intermicellar exchange dynamics; k_n – the rate constant for nucleation; k_g – the rate constant for particle growth. Modified from* [36].

At the end, growth occurs around these metal nuclei. The nucleation reaction and NPs growth takes place within the micelles. The morphology of prepared NPs depends on the morphology (size and shape) of the nanodroplets, as well as the type of surfactant, whose role is to hinder further growth of NPs and ensure their stability. It is a relatively new method, giving the possibility to control the morphology of the obtained NPs [37]). The disadvantage of this method is, similar to the sol-gel method, the need to use of toxic organic solvents, as well as the relatively long reaction time.

3) **Microwave-assisted synthesis methods** - here microwaves with wavelengths from 0.01 to 1 m are used. Microwaves are able to induce nucleation and growth of nanomaterials – not only of small NPs, but also of more complex nanomaterials, such as nanotubes, platelets, film coatings etc. During reaction, the microwaves interact with polar molecules, leading to the rotation and vibrational motion of these molecules, and finally – generating heat within the material. In conventional processes, the heat transfer occurs from surface to bulk. This radiation causes rapid, local overheating of the reaction mixture and ultra-fast synthesis of monodisperse NPs. It is a reliable, highly reproducible and fast method, which allows to easily control the morphology of NPs, without using organic solvents [38].

4) **Reduction of metal ions in solution** - is the most popular and easy method of obtaining NPs. The metal precursor (usually salt or acid) is reduced with appropriate reducing agents in the presence of stabilizers, which prevent the agglomeration of the synthesized NPs [39]. In the first step of the reaction, the metal salt is reduced to obtain zero-valent metal atoms. Then, these atoms can meet with other atoms or metal ions. This results in the formation of e.g. critical nuclei, the stability of which is sufficient not to dissolve in the solution. The size of this critical nuclei is usually small (about 1 nm), depending on the strength of the metal-metal interaction and the redox potential difference between the precursor and reducing agents [40]. In turn, in nano-alloys, synthesis is achieved by co-reduction. In co-reduction, two or more metal precursors, with only a slight difference in redox potential, are simultaneously reduced. Thus, as a result

of this reaction, nano-alloys are formed, without phase segregation of the individual elements. Natural compounds (e.g. plant extracts) can be also used as reducers, resulting in green chemistry methods. Thanks to these methods, it is possible to obtain monodisperse NPs with different morphology (shape and size), as well as surface charge by selecting appropriate types and concentrations of precursors, reducing agents, stabilizers and non-toxic solvents, as well as the time and temperature of the synthesis reaction. All NPs types synthesized during the PhD dissertation were obtained using this method. A detailed description of the mechanism of individual NPs synthesis reaction can be found in the „Materials and methods" section.

There are also bottom-up techniques for obtaining multicomponent NPs. They are mainly based on the above-described methods for the preparation of monometallic NPs. In order to prepare multicomponent NPs by wet chemistry methods, one of the following three strategies should be used:

- **Deposition of NPs** (forming the shell) **on the previously synthesized NPs** (core) – it is a multi-stage reaction depending on the number of NPs components. In the first stage of the reaction, the core NPs (e.g. Au NPs) are obtained and then, in the next step, a second metal is deposited on the surface of previously synthesized NPs [41], [42]. Then, such bimetallic core-shell NPs can be covered with a third metal. In this method, it ought to be remembered that the stabilizers/reducing agents used in the preparation of the core, may hinder or even prevent the reduction of further nano-metals (potential shell). Moreover, the deposited metal precursor should be well soluble in the solution of previously synthesized NPs. As a part of this PhD thesis, two types of bimetallic AuPd NPs were synthesized using this synthesis route,

- **One-step synthesis of multicomponent NPs** – compared to the previous method, this reaction takes place in one step. At the same time, the precursors of two or more metals are mixed in the solution and reduced under appropriate reaction conditions [43], [44]. It should be noted that this strategy will only work, if all precursors can be reduced by the same agent. Furthermore, when the electrochemical potential of individual metals is only slightly different, nano-alloy structures can be obtained, instead of core-shell structures. In this dissertation, bimetallic AuPt and ternary AuPdPt NPs were fabricated applying this method,

- **The use of the electrostatic interaction (zeta potential theory)** – first, the individual NPs are synthesized, followed by determination of the zeta potential values (more about the zeta potential can be found in paragraph 2.3.6.). If the measured zeta potential values have different signs (negative and positive), it is enough to only mix two solutions of different NPs, as the NPs will be attracted by electrostatic interactions. It is worth noting that the value of the zeta potential depends on the pH of the NPs solution [45].

1.1.2. Properties of noble metal NPs

The previously described various methods of synthesis, allow to obtain NPs with different morphologies (shape, size, porosity etc.), often avoiding organic solvents. Due to the unique properties of these nanomaterials, there is no area where they would not be applicable. Recently, an increasing use of nanotechnology has been observed, not only in various industries, but also in medicine [46]–[48]. In this doctoral thesis the properties of NPs, which are important for medical application, especially in supporting of PIr, were examined and described.

The chemical composition of NPs is the basic property that determines their usefulness in medicine. High-Z metal NPs are desirable to enhance the irradiation effect of cancer cells with protons. More information on the role of the interaction of these NPs with protons can be found in paragraph 1.3. Other properties of NPs that are of extraordinary importance in medicine are:

- **Size of NPs** – the size of NPs influences *in vivo* processes, such as circulation half-lives, extravasation through leaky vasculature and macrophage uptake. As can be seen, (Figure 4) the, ultra-small NPs rapidly undergo renal clearance after intravenous administration. Larger NPs readily accumulate in the liver due to the presence of non-continuous endothelia with vascular fenestrations having 50-100 nm. Moreover, the larger particles easily accumulate in the lungs, which makes it possible to use these NPs for targeted treatment of e.g. lung cancer. The spleen filtration also takes into account the retention of large NPs, as the size of the interendothelial cell slits in the spleen is about 200-500 nm [49],
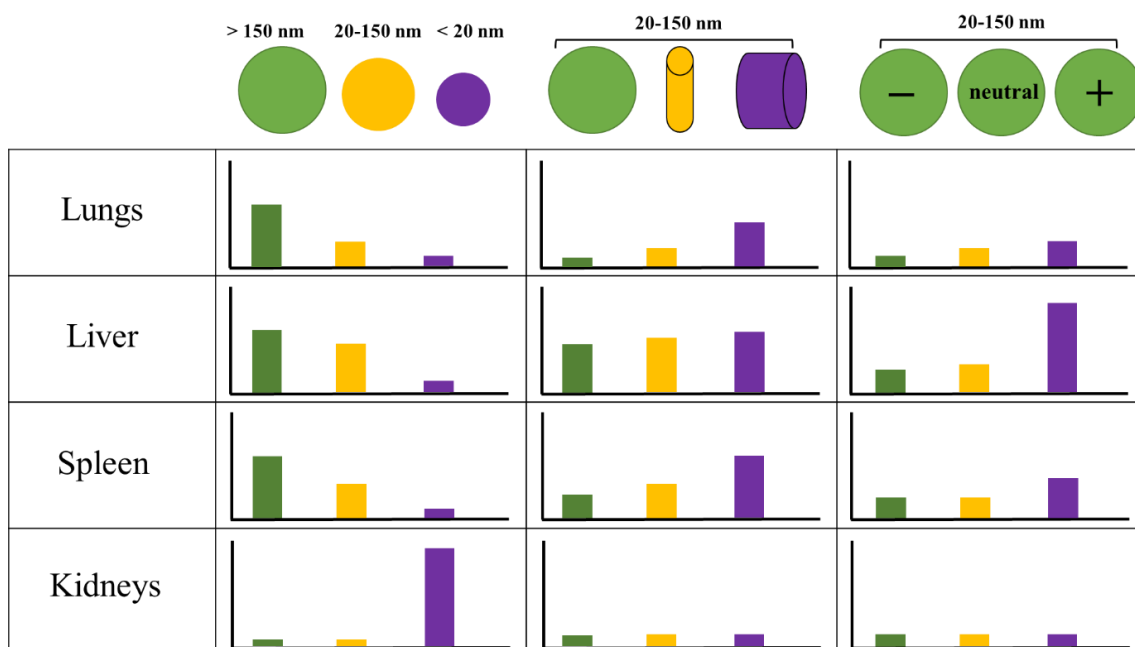
Figure 4. *Biodistribution of NPs in lungs, liver, spleen and kidneys depending on size, shape and surface charge. Modified from* [50].

- **Shape of NPs** – geometry of NPs drives initially their internalization into the cells. NPs with different shapes are characterized by unique flow characteristics, that can alter circulating lifetimes, interaction of NPs with cell membrane and macrophage uptake. As shown in Figure 4, discoidal NPs have the greatest biodistribution in the lungs, liver and spleen compared to spherical and rods-like NPs. It was also show that NPs characterized by high aspect ratios and minimal regions of curvatures are more likely to undergo phagocytosis and can accumulate more effectively, for example, within a tumor [51]. The shape of NPs significantly influences the future potential application of NPs to aid radiation-based anticancer therapies. Exemplary, it was shown that spherical Au NPs showed better radiosensitizing properties in supporting X-ray radiotherapy compared to gold nanospikes and gold nanorods [12],

- **Surface charge of NPs** – it was shown that NPs with negative charge allow for longer circulating half-lives. Moreover, the negatively charged NPs show reduced accumulation in the liver and spleen (Figure 4). In contrast, positively charged NPs tend to have higher uptake by most cells. Therefore, in order to more effectively deliver NPs to tumors in the body, these NPs should be designed in such a way, that after intravenous administration they would have a negative or neutral surface charge, however, based on an environment stimulus, they should change to positive charge after reaching the tumor localization [52],

- **Aggregation and stability** – the aggregation factor of NPs is also important in biomedical application of NPs. Stability of NPs means that they should not agglomerate, crystallize, change shape, size etc. [53], [54]. Although the produced NPs are originally ultra-small, over time they can form larger, colloidal aggregates that may no longer be suitable for medical applications. These small NPs have a higher free surface energy, which explains their susceptibility to form larger NPs clusters. The stability of NPs in solution depends, among others, on the pH of the solution and the concentration of the electrolyte in the solvent. Agglomeration can be prevented by adding to the NPs solution so-called protecting agents [55]. It has also been shown that the form of NPs (agglomerated or non-agglomerated) significantly affects the cellular uptake of these NPs. The most common way of internalizing dispersed NPs is caveole-mediated endocytosis, but for agglomerated NPs it is more likely that they enter the cell *via* micropinocytosis [56].

- **High surface to volume ratio** – this parameter has remarkable importance regarding the use of NPs as potential radiosensitizers. The smaller NPs are characterized by a greater surface to volume ratio. Increment in the surface area will allow a larger populations of these atoms to be located at the surface of NPs, rather than its interior [55]. Exemplary, for 30 nm NPs about 10 % of the atoms are on the surface, and for ultra-small 3 nm NPs – as much as 50 %. Thanks to the highly developed surface, these NPs will more effectively interact with X-rays or protons, giving a better therapeutic effect in such combined therapy. Besides, the large surface area to volume ratio can be functionalized with a higher amount of molecules (including drugs, targeting agents etc.) [57], [58],

- **Possibility of functionalization** – noble metal NPs can be easily modified covalently or non-covalently, which gives them new properties. Unmodified NPs are often characterized by increased toxicity (they are not biocompatible) and limited biodegradability. Functionalization of NPs can sometimes overcome these problems. The non-covalent strategy of NPs functionalization is based on a large number of weak interactions, such as ionic, van der Waals, hydrophobic or electrostatic interactions. Unfortunately, non-covalent modifications can be easily influenced by parameters such as pH and ionic strength. In turn, covalently modified NPs are more stable, but require more complicated preparation. Noble metals can be functionalized by using crosslinkers containing e.g. –SH or- NH_2 groups [59]. Especially, in the case of crosslinkers containing toxic sulfur, it is very important to thoroughly rinse the solution of functionalized NPs from the remains of unreacted crosslinkers. As the NPs can be functionalized, it is possible to attach some drugs (e.g. cytostatics) and compounds improving the specificity of these nanosystems towards e.g. cancer cells [59]–[61]. These modifications enable so-called active targeting, as the ligand-modified NPs have a particularly high affinity for specific overexpressed receptors on the cell surface. Exemplary, galactose-modified NPs specifically target liver cancer cells that have an excess of galactose-specific asialoglycoprotein receptors on their surface [62].

1.1.3. Interaction of NPs with living cells

Interactions between NPs and target cells play a key role in understanding the biomedical potential of NPs. The engineering of NPs has a remarkable impact on the behavior in NPs contact with cells, because cellular uptake of NPs is highly dependent on the physicochemical properties of our nanomaterials. In general, when NPs are in the vicinity of the outer cell membrane, they can interact with it and enter the cell or be adsorbed on the cell surface [63], [64]. NPs can get into the cell through two different mechanisms, namely active and passive transport (Figure 5).

Active transport of NPs is a type of cellular uptake, which requires energy is energy-dependent. There are three types of active transport of particles: (i) **Endocytosis** – in this type of transport, the cell membrane is deformed, and it wraps around the penetrating NPs. The cell ingests NPs mainly by phagocytosis and macropinocytosis (for engulfing NPs larger than 500 nm) or by clathrin-, caveolin-dependent or clathrin/caveolin-independent endocytosis (in the case of smaller NPs). **Phagocytosis** in the human body plays a role mainly in the innate immune response and occurs mainly in professional phagocytes, namely tissue macrophages, and blood monocytes, and neutrophils. Phagocytosis consists of several steps: linking the pattern recognition receptors with the appropriate ligand, formation of a vesicle (phagosome) with the participation of actin-binding proteins, kinases, phospholipase C and cholesterol. The phagosome is then fused with the lysosomes to form the phagolysosome. **Caveolin-mediated endocytosis** is related to the reorganization of the actin cytoskeleton and the action of dynamin. The interaction of the actin cytoskeleton and dynamin produces small vesicles (50-80 nm) that can fuse with early endosomes forming lysosomes or fuse to form caveosomes, which are then transported *via* microtubules to their destination.

Clathrin-mediated endocytosis is one of the most common pathways for NPs uptake, requiring specialized receptors on the surface of cell membrane. In the first step, the ligand binds to the appropriate receptor and forms a receptor-ligand complex. These complexes are concentrated in proper places on the cell membrane, where the protein-clathrin accumulates from the side of the cytoplasm. The membrane bulges and a vesicle covered with clathrins is formed. Then, endocytosis takes places inside the cell. The released vesicle becomes an endosome, which is transferred to the Golgi apparatus and to other cell organelles. In **clathrin/caveolin-independent endocytosis** the penetration of NPs into cells takes places in a dynamin-dependent (requires small guanosine triphosphate Ras homolog A) or dynamin-independent pathway. **Macropinocytosis** is a non-specific intracellular absorption pathway, in which the actin cytoskeleton is involved. In this process, substances, which are soluble in the extracellular fluid, most often in anionic or electrically neutral form, are incorporated into the cell. Transport vesicles – macropinosomes – have a diameter of 100 nm to 1 μm. Apart from actin, Rho GTP-ase, phosphatydyloinositol kinase, serine-threonine kinase and Rab proteins are involved in the formation of macropinosomes. When the macropinosome is formed, it is further transported by microtubules into to cell interior [65], [66].
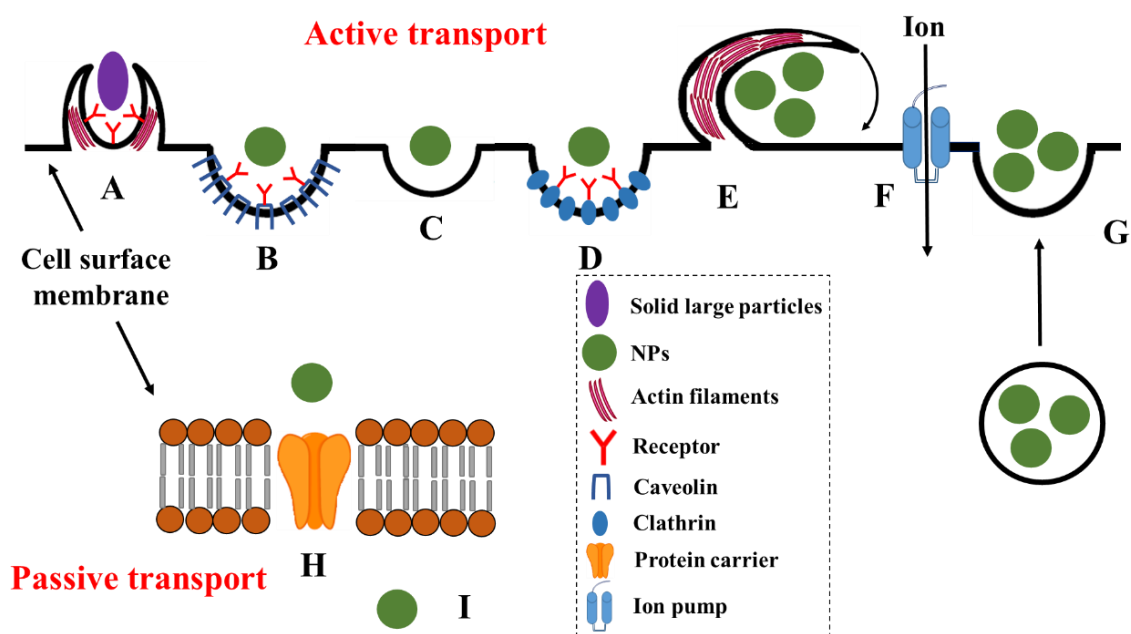
Figure 5. *Active and passive transport of NPs. A) phagocytosis, B) caveolin-mediated endocytosis, C) clathrin-caveolin-independent endocytosis, D) clathrin-mediated endocytosis, E) macro-pinocytosis, F) ion pumps, G) exocytosis, H) facilitated diffusion and I) simple diffusion. Modified from* [67].

(ii) **Exocytosis** is the inverse of endocytosis and involves the secretion of vesicles and their transport from membrane compartments, such as the endoplasmic reticulum and the Golgi apparatus. Then, the vesicle and its contents are directed outside the cell or to the lysosomes. Exocytosis is involved in the construction and distribution of cell membranes after cell division and in the sorting of proteins [67]. Finally, the last transport mechanism is (iii) **ion pumps**. Selective transport of ions such as calcium, sodium, potassium and hydrogen can be achieved by ion pumps. Adenosine triphosphate (ATP) or light is used by pumps to direct ions against their gradient. ATPases and ATP-binding cassette pumps bind to ATP and transfer the ions

across the membrane. The most popular ion pumps in the body are sodium-potassium (Na^+–K^+) and calcium pumps [67].

In turn, **passive transport** is another form of NPs cell penetration based on a concentration gradient, thus not requiring energy. Passive transport may occur as **simple diffusion** (NPs enter the cell by passing through the protein channel) or **facilitated diffusion**, when the protein carriers are used [67], [68]. Inside the cells, NPs are already in contact with the intracellular environment and can be degraded by enzymes, pH or by dissociation (for e.g. polymeric NPs) [69] or cause impairment of lysosomal function by alkalinizing their pH by for e.g. poorly-biodegradable Au NPs [70]. Some cells, especially cancer ones, show the ability to remove NPs or drugs e.g. due to the efflux pump's activity, which contributes to drug resistance in many cancers [71].

It is worth noting that the mechanism of cellular uptake depends not only on the morphology (shape or size) of NPs, but also on their surface charge, hydrophobicity, attached ligands, as well as the presence of so called protein corona on the surface of NPs (Figure 6) [72]–[74].
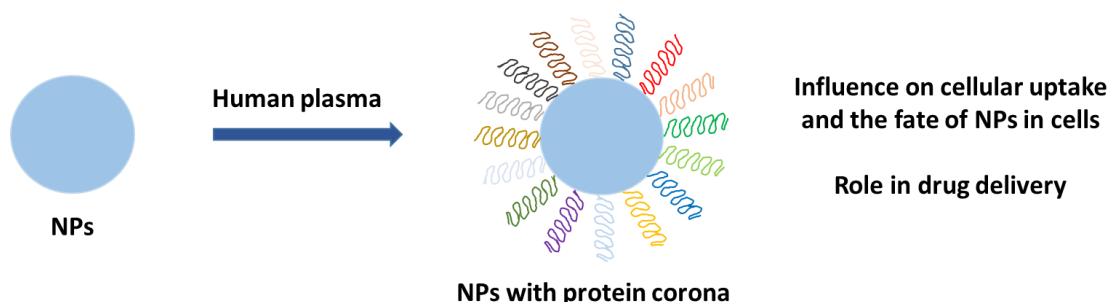
Figure 6. *General scheme of protein corona formation and its function.*

More recently, the relevance of the formation of protein corona on the surface of NPs has been noticed. It has been shown that nanocarriers are covered with proteins as a result of contact with body fluids. The type of proteins included in the protein corona determines the interaction with the cell membrane, and the mechanism of cell absorption. It has been shown that protein corona may consist of as many as 300 different proteins [55]. Moreover, it has already been proven that the formation of the protein corona affects hemolysis, thrombocytes, NPs uptake and the death of endothelial cells [55], [75], [76]. It is assumed that better understanding of the role of protein corona will allow more effective delivering of the therapeutic substances into the cells [77].

When assessing the interactions of cells with NPs *in vivo*, it should be kept in mind that before NPs reach the target cell, they often must overcome biological barriers (such as blood-brain barrier or blood-testis barrier). Moreover, the NPs should be constructed in a way to avoid opsonization, uptake by macrophages, early degradation and excretion from the body [78]–[80].

1.2. Cancer

1.2.1. Cancer development

Cancer is a disease, in which cells disrupt apoptotic mechanisms and start to divide abnormally in an uncontrolled manner, leading to a tumor formation. Developing tumor at the beginning is benign, the cells grow slowly and do not invade nearby tissues. Untreated, it turns to malignant tumor characterized by eight major hallmarks: (i) **Self-sufficiency in growth signals** – cancer cells multiply independently of external signals, so called growth factors. They independently produce autocrine signaling and are capable of destroying „off switches" that prevent these autocrine signals from overgrowing. Cancer cells deregulate controlled cell division because the proteins, which control the cell division, are altered [81]. (ii) **Insensitivity to anti-growth signals**, where cancer cells are capable of inactivating suppressor genes (e.g. Rb), which under normal conditions make it possible to inhibit the cell growth. Suppressor genes in normal cells receive information from the cells that it is ready to divide or inhibit the cell division in the case of DNA damage [81], [82]. (iii) **Tissue invasion & metastasis**, when cancer cells fill the space, they are in, they won't stop growing, but will continue the grow and divide, invading neighboring tissues. After that, they attack the surrounding blood vessels. Those cells that are not destroyed in the bloodstream will settle down in a new place and start dividing again, forming metastases [82]. (iv) **Limitless replicative potential** – normal cells have a certain number of divisions (called the Hayflick limit) and then die. In turn, cancer cells manipulate an enzyme (telomerase) to increase the length of the telomere, allowing them to divide indefinitely [83]. (v) **Sustained angiogenesis** occurs**,** when a tumor consists of both cancerous and normal cells. In order to survive, a growing cancerous tumor requires the formation of new blood vessels, which will provide the right amount of oxygen and nutrients. Cancer cells activate so-called „angiogenic switch", which causes that normal cells, within the tumor, produce new blood vessels [81]. (vi) **Evading apoptosis** – apoptosis, called cell suicide, is the programmed death of a cell, when it is severely damaged. Apoptosis is deregulated in cancer cells, thus changing the mechanisms that detect abnormalities in the cells. Consequently, neoplastic cells, even if they are severely damaged, do not follow the path of apoptosis [81]. (vii) **Reprogramming energy metabolism** occurs, when cancer cells are capable of metabolic reprogramming, as they require more energy due to their continual growth and proliferation. Cancer cells are characterized, among others, by increased glycolysis, induction of pentose phosphate pathway, as well as upregulation of lipid and amino acids metabolism [84]. (viii) **Evading immune response** – cancer cells are characterized by an escape from immune surveillance, leading to not recognizing them as non-normal cells. Under physiological conditions, the immune system, and more specifically T-lymphocytes, destroy the mutated cells. However, some cancer cells can inhibit the activity of T-lymphocytes by stimulating a certain group of protein, called immune response checkpoints [85].

Carcinogenesis is a multi-stage, complex process. Generally, it consists of three stages: initiation, promotion and progression. As a result of damaging a specific gene in the DNA of a normal cell, a single mutation occurs. This damage can be the result of many different factors, such as inherited gene mutations, external factors (physical or chemical) and viral infection [86]. If the damage is not repaired or the cell does not die as a result of apoptosis,

the process of neoplastic transformation is initiated (**initiation stage**). The second step is **promotion**, which is the accumulation of genetic and epigenetic changes that lead to the conversion of the mutant cell into a cancerous cell, i.e. cell undergoing uncontrolled division. This stage may last for several years and is reversible – it is possible to change this process by chemopreventive agents and affect growth rates [87]. The **progression** of cancer begins with mutations that promote cell proliferation and disrupt its apoptosis machinery. The process is applicable only for a solid tumor, such as carcinoma or sarcoma. For leukemia or lymphoma, the cells float freely, thus they are found not only in one location in the body. Then, the mutated cells divide rapidly divides, leading to **hyperplasia** – the cells have a normal appearance, but there are too many of them. The cells with altered morphology and additional mutations are generated (**dysplasia**). Dysplasia occurs as a result of additional genetic changes in hyperplastic cells. At this stage, cells do no longer appear normal. The next stage is a so called „**cancer *in situ***", when strongly altered cells stop to differentiate and loose contact with other cells. Such cells become more and more primitive in their abilities. For example, at this stage (i) the liver cells no longer secrete specific proteins. Importantly, the cells have not yet crossed the basal lamina and do not attack normal tissues. These tumors are completely surgically treatable, as all abnormal, altered cells are found in one location. The final stage is an **invasive carcinoma**, where cancer cells spread around, invading normal tissues and metastasize through the bloodstream and the lymphatic route [88], [89]. The depiction of the individual stages of cancer development and progression is shown in Figure 7.
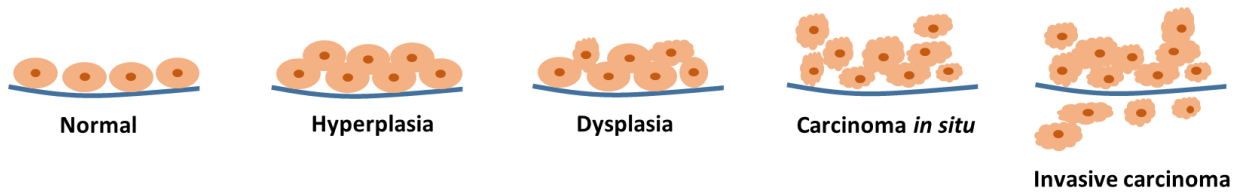
Figure 7. *Stages of cancer progression (description given in the text).*

There are mathematical models describing the tumor growth, but none of them fully illustrate the complexity of the tumorigenic process. To date, two models reflect the tumor growth in a most adequate way: the Gompertz model (equation 7) and logistic model (equation 8). Both are sigmoidal in shape, what qualitatively shows the tumors growth slowdown observed experimentally [90], [91]. V_0 is the volume at t = 0; a, A, b, B are the model parameters.

Gompertz model:

$$V(t) = V_o \exp\{A[1 - \exp(-at)]\} \tag{7}$$

Logistic model:

$$V(t) = \frac{V_o B}{V_o + (B - V_o)\exp(-bt)} \tag{8}$$

Although both models have many similarities and can be used to approximate tumor growth, it has been shown that tumor growth is better reflected by the logistic model. On the other hand, the Gompertz model is more often used to simulate the growth of e.g. bacteria [92].

1.2.2. Photo- and radiation-based anticancer therapies: light, X-rays, gamma-rays, neutrons, protons

Photo- and radiation-based anticancer therapies are commonly used as local methods of cancer treatment. Both can be used before surgical intervention to reduce the initial tumor size (e.g. in the case of colorectal cancer) and in postoperative adjuvant therapy, often in combination with chemotherapy and/or immunotherapy. These types of therapies can also be used in palliative treatment as monotherapy, effectively relieving the cancer-related pain [93], [94].

Anticancer phototherapies are medical treatments, where the tumor is irradiated with a light beam (Figure 8). Photo-based anticancer therapies include: (i) **Photothermal therapy** (PTT) where the photothermal agent is delivered to the area of the tumor and then, under the influence of light, it heats up destroying the surrounding cancer tissues. During PTT, lasers with a wavelength in the range of 650 nm to 980 nm (visible light and near infrared region – NIR) are directed at the tumors for a few minutes, usually no more than six, destroying them with localized heat. There is danger that the normal tissue surrounding the tumor may absorb the heat from the radiation and be damaged. (ii) **Photodynamic therapy** (PDT) is a method involving a series of photochemical reactions caused by light-activated photosensitizers, which are toxic for cancer cells. The photosensitizing agent is most often applied in the form of a gel or ointment. It usually takes 1-3 h to absorb it. After this time has elapsed, a beam of red light with a specific wavelength is directed to the selected location and exposure takes approximately from 5 to 15 minutes. PDT is very beneficial for its aesthetic effects – unlike traditional surgical methods, it leaves no marks or scars on the skin. It worth mentioning that PDT also has some limitations. The light beam used for medicinal purposes can penetrate only up to about 8 mm deep into the tissue. For this reason, PDT can only be used to treat superficial tumors. [95].
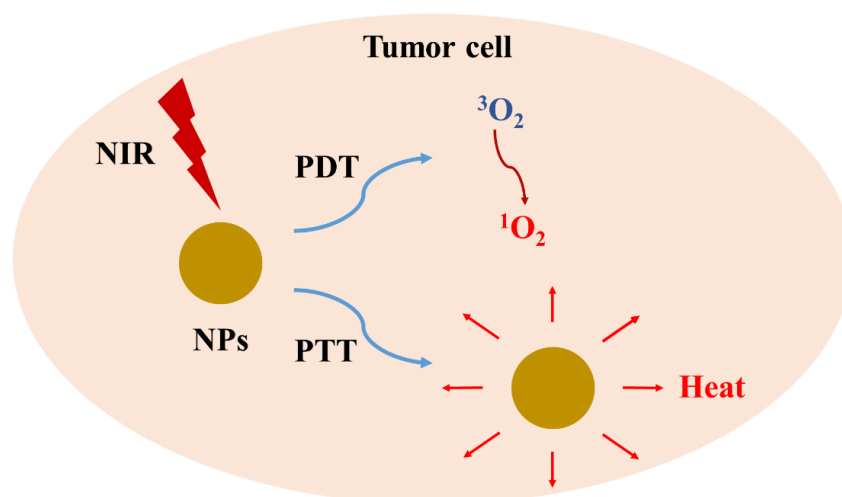
Figure 8. *General scheme of PDD and PDT. Modified from* [96].

For radiation-based anticancer therapies, generally, two main types of radiotherapy can be distinguished: (i) **Photon radiation therapy**, which includes X-ray and gamma radiation therapies and (ii) **particle radiation therapy**. The first ones are more often used in medicine compared to the particle radiation therapy, due to the lower cost of treatment. Photons are small

packets of high energy light and photon energy decreases, as it goes through the body. Therefore, in order to deliver the desired dose to the tumor, shallower places in the body (e.g. skin) will also be damaged, so there is a risk of secondary neoplasms, most often of skin origin [97], [98]. Moreover, photon radiotherapy can be divided into **teleradiotherapy** – radiation comes from a source outside the body and **brachytherapy**, where the radiation comes from implants placed inside the body. There is also an innovative method, called **stereotaxic radiotherapy**, which enables more precise irradiation of the tumor with a higher total dose of radiation [99],

In the **particle radiation therapy**, being a form of external beam radiotherapy – either energetic neutrons – **boron neutron capture therapy** (BNCT), or a proton beam – **proton therapy** (PT) are used. BNCT is based on the selective delivery of a stable boron nuclide to the tumor, followed by irradiation with low-energy neutron radiation. Neutrons collide with boron, causing a nuclear decay reaction, resulting in a highly concentrated dose of radiation. However, difficulties with neutron beam generation and its control are factors that make this particle therapy rarely used today [100], [101]. An alternative is PT, which uses high-energy protons to precisely destroy the tumor, and the details will be presented in the next paragraph.

1.3. Proton therapy

PT is a relatively new method of cancer treatment. The properties of protons make PT in many cases more effective than traditional photon radiotherapy (Figure 9).
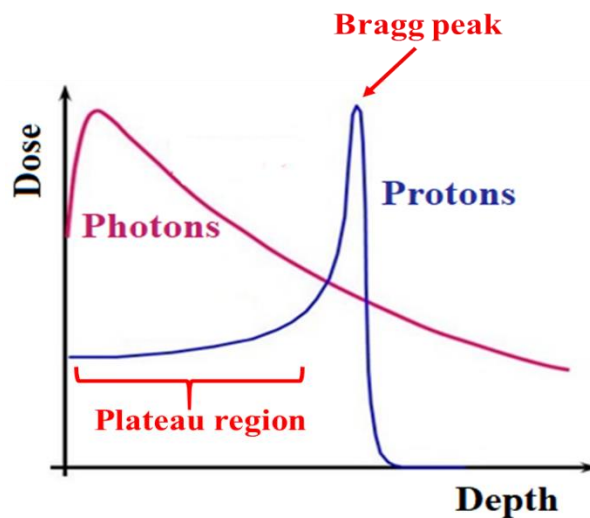
Figure 9. *The comparison of dose-depth profiles for photon and protons.*

As presented in Figure 9, in classical photon radiotherapy, the maximum radiation dose goes to the patient's skin and not to the tumor inside the body. On the other hand, for PT the maximum energy reaches a precisely defined depth, depending on the proton beam energy. This is the **Bragg peak**. It should be noted, that near the Bragg peak, the **linear energy transfer** (LET), being the amount of energy per unit length lost by protons traversing a material, changes very quickly. In the second area – **plateau region** – the LET changes very slowly and only a small percentage of the radiation dose is deposited in here [102]. To sum up, PT will be more

effective in the treatment of tumors deep inside the body, especially with locations, where surgical interventions could be associated with high risk of damaging sensitive organs in the body (e.g. brain). Protons show a biological effect similar to photons, as evidenced by the value of **relative biology effectiveness** (RBE) coefficient for protons = 1.1. The RBE is a parameter, which determines the effectiveness of the selected PIr in relation to X-rays. For particles with high ionizing capacity, as protons, this biological effect depends not only on the deposited radiation dose, but also on the kinetic energy and the degree of ionization [103].

Loses of kinetic energy of protons traversing the matter are described by **Bethe-Bloch formula** (equation 9).

$$-\frac{dE}{dX} = -4\pi N_A r_e^2 m_e c^2 z^2 \frac{Z}{A}\frac{1}{\beta^2}\left[\frac{1}{2}ln\frac{2m_e c^2\gamma^2\beta^2 T_{max}}{I^2} - \beta^2 - \frac{\delta(\beta\gamma)}{2}\right] \qquad (9)$$

where N_A – Avogadro's number; r_e – particle radius; m_e – particle mass; c – speed of light; z – particle charge; Z – atomic number; A – mass number; β – relative speed; δ – correction due to the polarization effect of the medium density; γ – relativistic velocity factor; T_{max} – maximum kinetic energy, which can be transferred to protons; I – average ionization energy.

From the Bethe-Bloch formula it follows, that the energy loss is proportional to the square of the particle charge z^2, the ratio of the number of protons to nucleons (Z/A) and inversely proportional to the square of the particle velocity $1/\beta^2$ [6]. It ought to be mentioned, that the Bethe-Bloch formula is not valid for small energies of particles. Protons on their way to the target material interact with a large number of electrons and lose some of their energy, until they stop in the final material. This energy transfer, results in atom ionization followed by breaking the chemical bonds. Protons interact with matter mainly through inelastic or elastic Coulomb scattering (with electrons or atom nucleus, respectively), with a cross-section depending on the kinetic energy and charge of the incident particle. The protons can also interact *via* non-elastic nuclear reaction, where the primary proton is removed and secondary particles (e.g. protons, electrons or gamma rays) are generated [6]. Theoretically, the proton Bremsstrahlung is also possible, although for the energy used in PT, this effect in less likely.

The radiation effect of the proton beam can be enhanced by metal NPs, called **radiosensitizers** (also known as radio-enhancers). The latter are compounds, which sensitize cancer cells to subsequent radiation-based anticancer therapy. It is extremely important that these radiosensitizers by themselves, added in a concentration required for PT, do not cause excessive cytotoxicity [104]. Radiosensitizers can be classified into three groups: small molecules (radiosensitizing chemotherapeutic agents, such as cisplatin and its derivatives), macromolecules (proteins and peptides) and NPs (high-Z metal NPs, including gold, platinum, silver and oxides: zinc, bismuth, hafnium or titanium) [105]–[111]. Originally, it was assumed, that NPs are effective radiosensitizers only for photon radiation, because their photoelectric interaction is strongly dependent on the atomic number. However, protons can also activate an avalanche of electron emission from NPs and surface plasmon excitation can produce numerous secondary electrons, making NPs effective radio-enhancers in PT [112].

PIr can have an indirect or direct effect on DNA molecules in the cells (Figure 10).
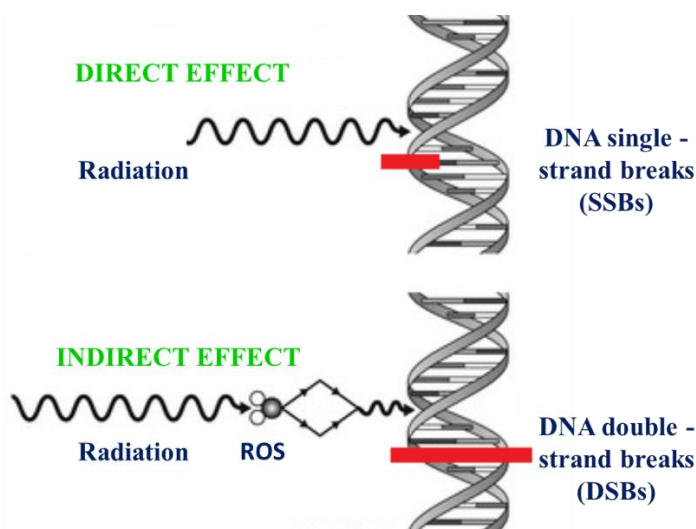
Figure 10. *Direct and indirect action of PIr. Modified from* [113].

About 80 % of radiation damage is thought to be caused by the **indirect effect**, which occurs, when protons interact with water, causing its radiolysis. This leads to the formation of reactive oxygen species (ROS), which in turn contribute to double-strand breaks (DSBs) of the DNA strand and cell apoptosis. Much less often, radiation **interacts directly** with atoms or molecules of the cell (DNA, proteins, and less often with lipids). There is no intermediate stage here, i.e. interaction with water molecules, but single-strand breaks (SSBs) of the DNA usually are in the radiation pathway [114]. Therefore, if nanoradiosensitizers are delivered inside the cell, ROS will be created as a results of the interaction of protons with NPs, leading also to cell death [115]. Thus, NPs-assisted PT would allow to reduce the total radiation dose and decrease the side effects of such therapy. The above-described way of NPs sensitizing cells is known as the **biological-chemical mechanism**.

There are also a pure, **biological mechanisms** involved in the sensitization of cells. Noble metal NPs can inhibit the cell cycle in the G2/M phase (cell division), in which cells show the highest radiosensitivity, consequently DSBs by NPs occurs and DNA repair mechanisms are inhibited [116]. The intensification of the bystander effect may also be a biological mechanism of radiosensitization. This effect has been observed in photon radiotherapy, but is possible in PT as well. The bystander effect occurs, when irradiated cells send a signal to neighboring, originally undamaged cells, resulting in cells damage [117].

In turn, the **physical mechanism** of cell radiosensitization by NPs is based on the increased production of secondary electrons due to the interaction of NPs with protons [118]. High-Z NPs can also induce the so-called Coulomb nanoradiator (CNR) effect. This effect produces burst emissions of fluorescent X-rays and low-energy electrons via Auger cascades, ultimately contributing to water radiolysis and ROS generation [119]. The final radiosensitizing effect will of course also be dependent on synthesis method and the NPs size. Indeed, smaller NPs, having a higher surface to volume ratio, will more effectively generate ROS and secondary electrons during interaction with the proton beam. Also NPs charge and – presumably – porosity will impact on the radiosensitizing effect, as more porous NPs

with a highly developed surface will interact more effectively with protons [5], [120]. A representation of the individual mechanisms of radiosensitization is shown in Figure 11.
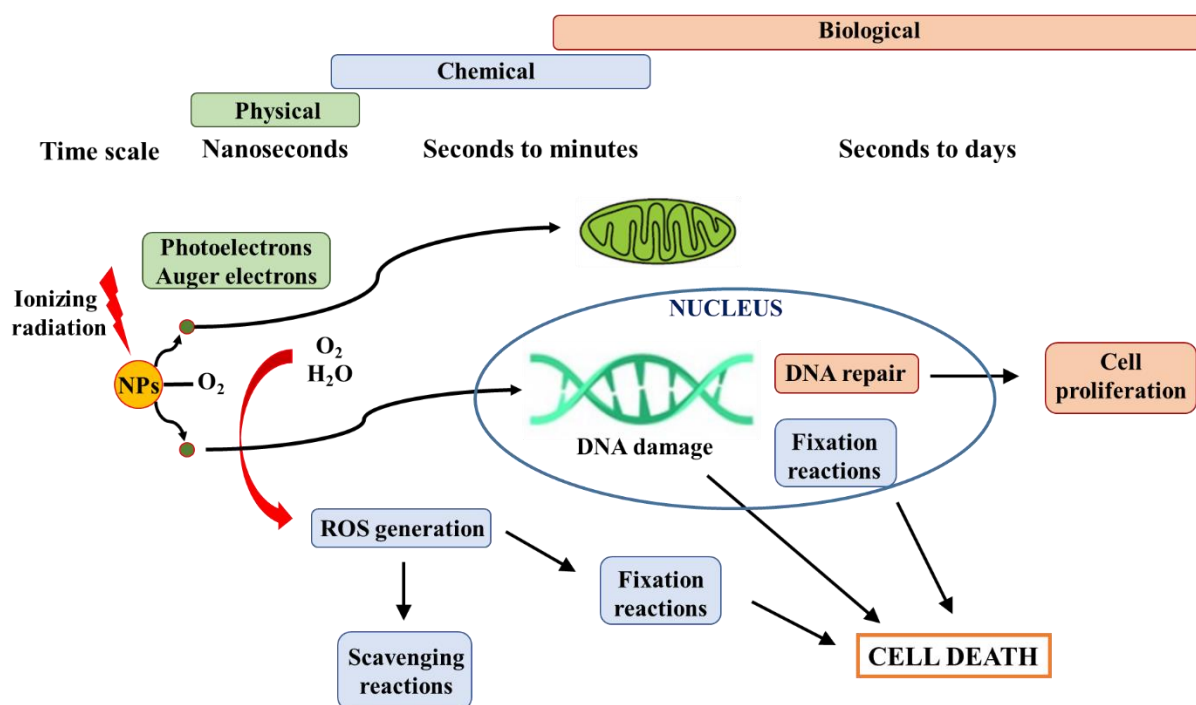
Figure 11. *NPs involved in the physical, chemical and biological mechanism of radiosensitization. Modified from [121].*

Currently, the AGuIX NPs is the most advanced theranostic nanosystem for radiosensitization in clinical trials (phase II). AGuIX are gadolinium-based NPs being studied both as contrast agents in MRI and as radiosensitizers for the treatment of metastatic tumors in the brain [122]. Moreover, a satisfactory effect of AGuIX nanosystem in MRI-guided radiosensitization in hepatocellular carcinoma has been reported [123].

1.4. Aims and hypotheses of the study

One of the most promising metals that may have potential application in supporting PT is gold. However, literature indicate that it is possible to replace Au NPs with other, cheaper nanomaterials such as Pt NPs or – especially – Pd NPs.

The aim of this dissertation was to design and synthesize NPs, which added in a non-toxic concentration to colon cancer cells culture, would enhance cell death after PIr in comparison with proton irradiated cells without NPs.

Therefore, the **specific goals** of the study were the following:

1) Synthesis, in a reproducible way, of monometallic and multicomponent NPs based on gold (≈ 16 nm), palladium and platinum (≈ 2-3 nm) using non-cytotoxic reagents,

2) Assessing the physicochemical properties (morphology, nanostructure, chemical composition, optical properties, zeta potential, concentration, interaction with high-energy protons) of the developed NPs,

3) Determining the non-toxic concentration of the NPs for cells,

4) Selecting, from the synthesized NPs differing by chemical composition, size and porosity, these NPs, which cause the most pronounced cytotoxic effect on cancer cells after PIr,

5) Evaluating, if the radiosensitizing effect is influenced by the biological-chemical mechanism or rather by the physical mechanism.

The following **research hypotheses** were formulated:

- NPs-PIr (defined as irradiation with 225 MeV proton beam with a total dose of 15 Gy of cell lines cultured with the synthesized NPs. After irradiation the cells were cultured for another 18 h and subsequently all tests were performed) gives a higher cancer cell death than PIr without the use of NPs,

- NPs-PIr is selective for cancer cells, being generally non-harmful to normal cells,

- NPs with a smaller size and bigger porosity show better radiosensitizing properties,

- The radiosensitizing effect is mainly due to the biological and chemical mechanism of radiosensitization, rather than to the physical aspects of the interactions of protons with NPs,

- The dynamics of NPs penetration into the cells differs depending on the selected cell line.

Chapter 2: Materials and methods

2.1. Reagents

Gold, platinum and palladium precursors (chloroauric acid trihydrate $HAuCl_4 \cdot 3H_2O$, chloroplatinic acid hexahydrate $H_2PtCl_6 \cdot 6H_2O$ and palladium (II) chloride $PdCl_2$, respectively), reducing agent and stabilizers (sodium borohydride, trisodium citrate, ascorbic acid, gallic acid, cetyltrimethylammonium bromide (CTAB) and ethylene glycol) were purchased from Sigma Aldrich (Burlington, MA, USA). SW480 and SW620 cell lines were obtained due to the courtesy of Professor Caroline Dive from Paterson Institute for Cancer Research, University of Manchester. HCT116 and CCD 841 CoN (CRL-1790) cell lines were purchased from the American Type Culture Collection (ATCC, Manassas, VA, USA). Gibco McCoy's 5A medium was obtained from Thermofisher (Waltham, MA, USA). Dulbecco's modified eagle medium (DMEM) and eagle's minimum essential medium (EMEM) were purchased from Corning® (Corning, NY, USA). Polymerase chain reaction-enzyme linked immunosorbent assay (PCR-ELISA) kit was obtained from Roche (Basel, Switzerland). 3-(4,5-dimethylthiazol-2-yl)-5-(3-carboxymethoxyphenyl)-2-(4-sulfophenyl)-2H-tetrazolium (MTS) test kit (Cell Titer96® Aqueous One Solution Cell Proliferation Assay) was purchased from Promega (Madison, WI, USA). Annexin-V apoptosis detection kit was obtained from BD Bioscience (San Jose, CA, USA).

2.2. Synthesis of NPs

2.2.1. Synthesis of monometallic Au, Pt and Pd NPs

a) Synthesis of Au NPs

Spherical Au NPs were synthesized by the Turkevich method, in which the precursor is reduced to metallic NPs under appropriate conditions (Figure 12) [124]. This method is one of the most popular and reliable methods of obtaining Au NPs with trisodium citrate, acts as a stabilizing compound for Au NPs, preventing their agglomeration. As a result, the synthesized NPs are stabilized with negatively charged citrate and its oxidation products [125]. By changing the molar ratio of gold precursor (chloroauric acid) to sodium citrate, it is possible to control the growth of the resulting gold nanospheres [126].

To produce Au NPs, 100 ml of 0.001 M aqueous $HAuCl_4$ solution was placed in a flask and then heated to the boiling point. Next, 15 ml of 1 % trisodium citrate was poured into the mixture and the reaction was continued for 15 minutes, observing the change of the solution to dark red. The obtained NPs were purified by centrifugation three times in fresh distilled water (20 000 x g, 20 minutes).
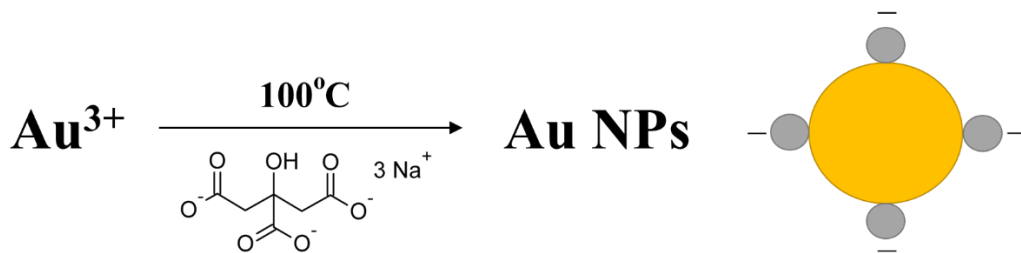
Figure 12. *Diagram showing the synthesis process of monometallic NPs on the example of Au NPs.*

b) Synthesis of ultra-small Pt NPs

The obtaining of ultra-small NPs requires the use of strong reducing agents (such as sodium borohydride) and/or organic solvents. In order to prepare ultra-small Pt NPs, the modified polyol method previously reported by Drzymała et al. [45] was used. In this method, ethylene glycol was used, which acted as both a stabilizer and a reducing agent. At temperatures above 100°C, the reaction proceeds relatively quickly, but the stability of the obtained Pt NPs depends on the pH, at which the reaction is carried out. An acidic reaction condition favors the formation or larger platinum-based agglomerates. Increasing the pH of the reaction mixture allows to obtain ultra-small, stable and non-agglomerated Pt NPs [127]. The Pt NPs were synthesized as follows: 0.048 g $H_2PtCl_6 \cdot 6H_2O$ was dissolved in a flask containing 40 ml of ethylene glycol. Then, 0.5 M solution of ethylene glycol in NaOH was poured into the reaction mixture until the pH $\approx$ 12. The solution was heated to 160°C on a magnetic stirrer, turning into a dark brown color. The reaction was continued for 3 h. The NPs were purified by repeated centrifugation (24 000 g, 30 minutes) in acetone, ethanol and copious amount of distilled water (24 000 x g, 30 minutes).

c) Synthesis of ultra-small Pd NPs

In comparison with Pt NPs, the ultra-small Pd NPs were prepared in water solution, using sodium borohydride as strong reducing agent. However, sodium borohydride has no stabilizing properties, so it was necessary to use an additional reagent. CTAB was selected, which efficiently stabilized NPs and ensures obtaining monodisperse, positively charged NPs. CTAB, being a quaternary ammonium surfactant, plays a role not only as a stabilizer of NPs, but also as a structure-directing agent. Unfortunately, its drawback is relatively high cytotoxicity [128].

For the synthesis of Pd NPs chloropalladium acid (H_2PdCl_4) was used, which was obtained by treating $PdCl_2$ with an equivalent of hydrochloric acid. The Pd NP synthesis was performed by mixing aqueous solution of chloropalladium acid (0.5 ml, 0.01 M) and CTAB (10 ml, 0.05 M). The reaction mixture was heated to 30°C on a magnetic stirrer, and then 1 ml of 0.5 M ice-cold sodium borohydride was added. The solution turned light brown immediately and foamed temporarily. The reaction was complete after 20 minutes and then the obtained NPs were purified by centrifugation three times in distilled water (16 000 x g, 15 minutes).

2.2.2. Synthesis of bi- and trimetallic AuPt, AuPd and AuPdPt NPs

Bimetallic AuPd CSs and AuPd NRs were synthesized by selective reduction of palladium precursors on pre-synthesized Au seeds using ascorbic acid. The choice of ascorbic acid as a reducing agent and stabilizer at the same time, is excellent from the point of view of biomedical application, because ascorbic acid is characterized by high biocompatibility [129]. A general scheme of the proposed reaction is given below (Figure 13).
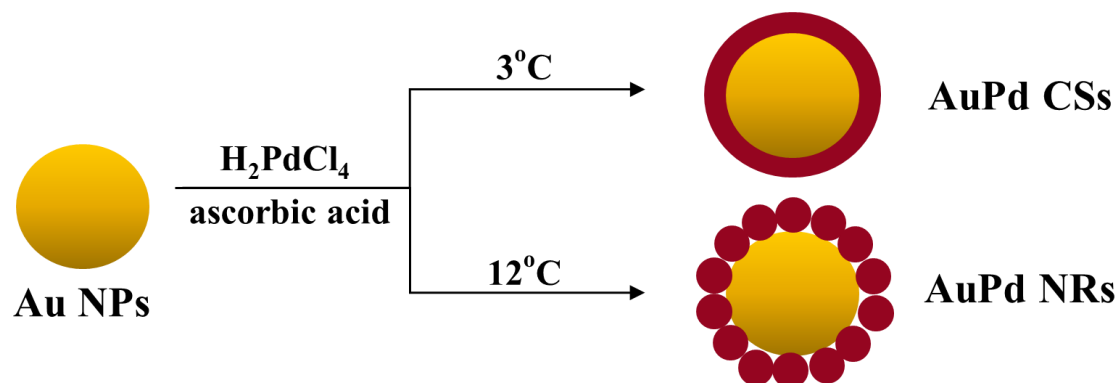
Figure 13. *Comparison of AuPd CSs and AuPd NRs synthesis process.*

In the synthesis process, both reactions differ only in temperature – all other parameters are the same. The slow, dropwise addition of ascorbic acid is essential for the proper formation of the palladium layer on the gold surface, otherwise palladium agglomerates.

a) Synthesis of bimetallic AuPd core-shell NPs (AuPd CSs)

The preparation of AuPd CSs was performed based on publication [130] with small modifications. 0.1 ml of 0.1 M aqueous solution of H_2PdCl_4 and 5 ml of pre-synthesized Au NPs were placed into an ice bath ($\approx 3°C$) on a magnetic stirrer. Then, 6 ml of 0.1 M ascorbic acid aqueous solution was slowly added dropwise during 1 h (0.1 ml per minute). A change of the solution color from pink to pale brown was noticed already after the addition of a few drops of ascorbic acid. The reaction was continued for another 30 minutes. The obtained NPs were purified by centrifugation three times in fresh water (20 000 x g, 20 minutes)

b) Synthesis of bimetallic nanoraspberry-like AuPd NPs (AuPd NRs)

The reaction and purification were carried out analogously as described above, however in this case, the synthesis was performed in a cold bath ($\approx 12°C$).

c) Synthesis of bimetallic platinum-decorated gold nanoparticles (AuPt NPs)

Bimetallic AuPt NPs were obtained using a cheap, eco-friendly, green reagent, which is gallic acid [131]–[133]. Gallic acid, due to its chemical structure, is a universal reducing agent, being a stabilizer at the same time. This reducing agent in its chemical structure has an aromatic ring containing carboxyl and hydroxyl groups, which form chelating rings with metal ions (e.g. derived from noble metal precursors). Gallic acid is oxidized to benzoquinones by exposure to electrophilic ions or air. Moreover, gallic acid can be successfully applied in medicine, because it exhibits strong anticancer properties, causing

simultaneously only little damage to normal cells [134]. The simplified scheme of the reaction taking place during the synthesis of AuPt NPs is depicted in Figure 14.

$$[AuCl_4]^- + 3e^- \longrightarrow Au + 4Cl^- \quad + 1.10 \text{ eV}$$

$$[PtCl_6]^{2-} + 2e^- \longrightarrow [PtCl_4]^{2-} + 2Cl^- \quad + 0.68 \text{ eV}$$
$$[PtCl_4]^{2-} + 2e^- \longrightarrow Pt + 4Cl^- \quad + 0.76 \text{ eV}$$
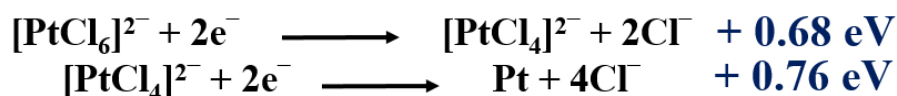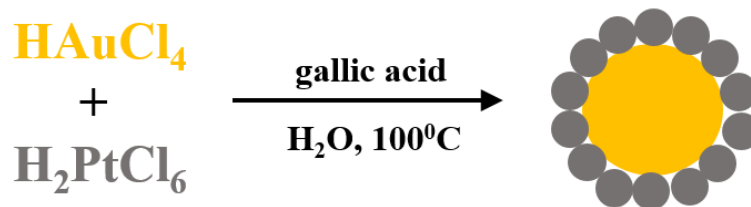
Figure 14. *Synthesis mechanism of AuPt NPs using gallic acid.*

The above reaction is based on the difference in the standard electrochemical potentials of platinum and gold. This difference is the driving force of the chemical reaction, ensuring that it occurs quickly. As shown in Figure 14, the reduction of the gold precursor to zero-valent gold takes place in one step. In turn, chloroplatinic acid is initially reduced to two-valent platinum, and in the next stage to metallic, zero-valent platinum. Due to significant differences in electrochemical potentials, gold is reduced first, creating the core of the NPs. Next, chloroplatinic acid is reduced to Pt NPs, which surround the pre-synthesized gold. Interestingly, by changing the molar ratio of the platinum and gold precursors, fascinating structures can be obtained, e.g. gold-platinum nanocauliflowers with a highly developed surface giving application potential in radiation-based anticancer therapies [43].

For the synthesis of AuPt NPs using gallic acid [44], 0.25 ml of 0.01 M aqueous solutions of $HAuCl_4$ and H_2PtCl_4, as well as 17.5 ml of distilled water were mixed in a round-bottom flask. The reaction mixture was heated until boiling on a magnetic stirrer and then 2 ml of 0.005 M freshly prepared gallic acid aqueous solution was poured into the boiling mixture. The reaction was carried out for 1 h, with a slow color change from colorless to gray-brown. The NPs were purified by centrifugation in fresh water three times (13 000 x g, 20 minutes).

d) Synthesis of ternary AuPdPt NPs

The synthesis of ternary AuPdPt NPs was carried out also using gallic acid as reducing agent and stabilizer. The scheme of the reaction for obtaining AuPdPt NPs with a double PdPt shell is shown in Figure 15.

$$[AuCl_4]^- + 3e^- \longrightarrow Au + 4Cl^- \quad + 1.10 \text{ eV}$$
$$[PdCl_4]^- + 2e^- \longrightarrow Pd + 4Cl^- \quad + 0.60 \text{ eV}$$
$$[PtCl_6]^{2-} + 2e^- \longrightarrow [PtCl_4]^{2-} + 2Cl \quad + 0.68 \text{ eV}$$
$$[PtCl_4]^{2-} + 2e^- \longrightarrow Pt + 4Cl^- \quad + 0.76 \text{ eV}$$
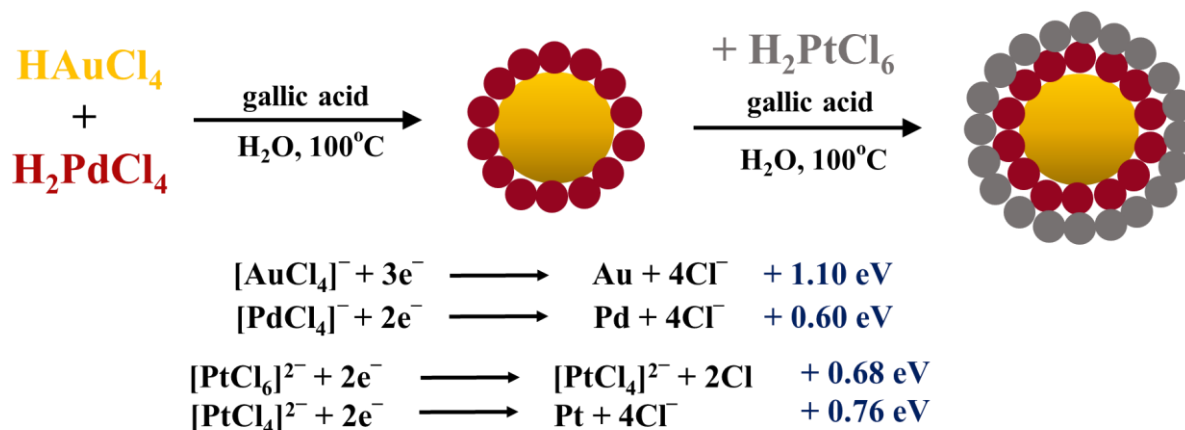
Figure 15. *Preparation of ternary AuPdPt NPs.*

In order to prepare a structure with a double shell composed of two separated metals, it is necessary to simultaneously reduce the gold and palladium precursors in one step. The electrochemical potentials of the three metals are different, so first gold will be reduced by gallic acid followed by palladium, which will form a shell on gold. When a change in the reaction mixture solution is observed, i.e. the formation of AuPd NPs has occurred, the platinum precursor can be added, which will quickly reduce to form the outermost layer. The procedure is as follows: 17.5 ml of distilled water and 0.166 ml of aqueous solutions of $HAuCl_4$ and H_2PdCl_4 were mixed in a round-bottom flask and then heated to the boiling point. A fresh portion of the aqueous gallic acid solution (2 ml, 0.005 M) was added and the reaction was continued for 30 minutes, observing the color of the solution turning light brown. Then 0.166 ml of an aqueous solution of H_2PtCl_4 was added, and the reaction was carried out for another hour. Finally, the NPs solution turned gray-brown. The obtained NPs were purified by centrifugation in fresh water three times (13 000 x g, 20 minutes).

The concentration of all NPs types was estimated by heating a known volume of the purified NPs solution to dryness in a laboratory muffle furnace. The dry NPs were weighted and thus it was possible to calculate their mass in the starting solution. The concentrations (μg/ml) determined in this way were similar to those calculated based of the equations of individual NPs synthesis reactions.

2.3. Techniques used for characterization of NPs

2.3.1. Transmission electron microscopy (TEM)

Transmission electron microscopy is a useful tool for characterizing the morphology, chemical composition and structure of nanostructured materials. This microscope uses an electron beam to image nanomaterials. Electrons have a significantly shorter wavelength than visible light, which allows to increase the resolution of the electron microscope compared to an optical microscope. In TEM, the image is formed by electrons passing through the sample. The electron source can be tungsten, lanthanum hexaboride or a field emission gun (FEG) referred to as the cathode [135]. The electrons generated by the cathode, are accelerated due to the attraction of the anode. Vacuum in the microscope is necessary in order not to interfere with the electron beam being characterized by wave-particle duality. This wavelength depends

on the potential difference between the cathode and the anode (known as the accelerating voltage) and can be described by the Broglie's equation:

$$\lambda = \frac{h}{mv} \tag{10}$$

where h – Planck's constant; m – electron mass; v – electron velocity.

Considering the dependence of momentum on the accelerating voltage, the above formula takes the following form:

$$\lambda = \frac{h}{(2meV)^{1/2}} \tag{11}$$

At high electron voltages, the electron speed increases almost to the speed of light and then equation 11 should be modified to take into account the relativistic effect:

$$\lambda = \frac{h}{\left(2m_eVe\left(1+\frac{eV}{2m_ec^2}\right)\right)^{1/2}} \tag{12}$$

where V – accelerating voltage, m_e – electron rest mass, e – electrons charge.

Accordingly, the greater the accelerating voltage, the larger the resolution of this microscope [136]. The electron beam emitted by the cathode is focused by the condenser aperture, and then part of the electrons passes through the imaged sample. The electrons re then focused by the objective, intermediate and projector lenses and finally inside on a fluorescent screen, where the image is visualized. The image is recorded either by a camera filming the screen or by a camera located under the screen. A general scheme of TEM is presented in Figure 16.

As a result of the interaction of the primary electron beam with the sample, various types of electrons (secondary electrons, back-scattered electrons, (in)elastically scattered electrons, Auger electrons), as well as visible light or characteristic X-rays are emitted. These individual signals are generated from different depths and volumes of the sample and each of these can be used for structural or chemical composition analysis as well as image formation.

Electron microscopy can be operated in transmission and scanning mode (STEM). When operating in this mode, thicker specimens than in the TEM can be observed and the electron beam, scanning the sample is focused to small spot (0.2 – 10 nm). The bright field image is obtained using a detector collecting the transmitted and the low-angle scattered electrons. In turn, imaging in the dark field is based on non-coherent scattering. For this purpose, the high-angle annular dark field (HAADF) detector is used to collect the electrons diffracted at high angles. The intensity (contrast) of these images is proportional to the square of the atomic number Z^2, which allows to distinguish groups of atoms derived from different chemical elements [136]. Another TEM operating mode is selected area electron diffraction (SAED), which is described in more detail in paragraph 2.3.3. The chemical analysis of the samples was performed by energy-dispersive X-ray spectroscopy (EDS) detector.
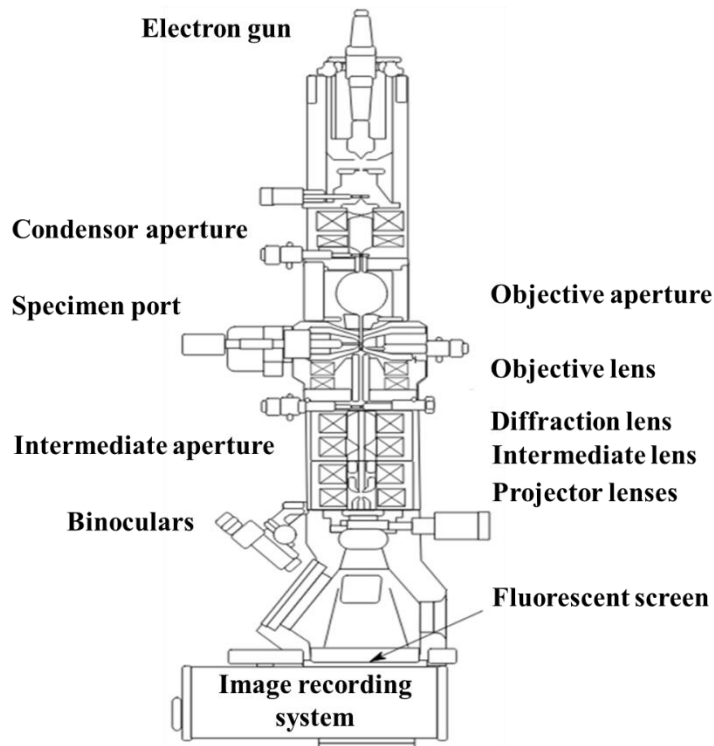
Figure 16. *Schematic diagram of a transmission electron microscope. Modified from* [137].

2.3.2. Energy-dispersive X-ray spectroscopy (EDS)

The EDS is a detector, which allows to analyze the chemical composition of a sample either in the TEM or in the STEM mode. In the TEM mode global information from the entire sample illuminated by the electron beam is acquired, while in the SEM mode, as the sample is illuminated with a focused beam, local information from a point area of the sample is obtained. Thus, it is possible to acquire elemental distribution maps, showing graphically the location of the respective elements in the sample. The physical basics of EDS are depicted in Figure 17.
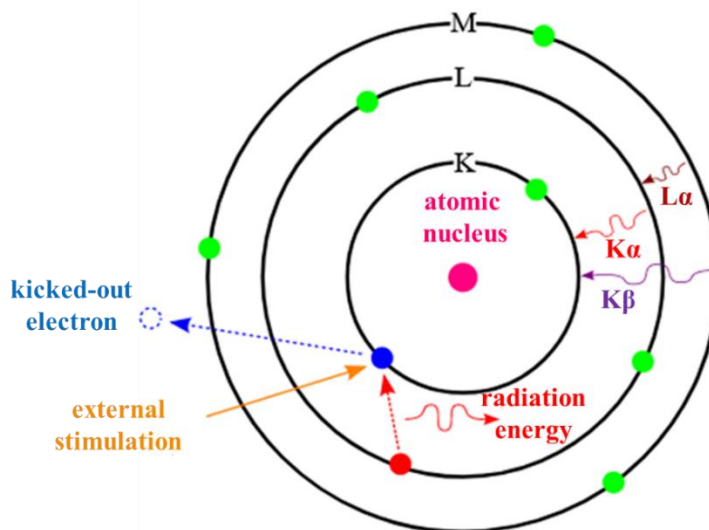
Figure 17. *Basics of EDS method* [138].

The characteristic X-ray radiation, collected by the EDS detector, is produced by the interaction of high-energy electrons with the sample. The beam excites ground-state atoms, knocking electrons out of the inner electron shell. The „hole" after the knocked out electron is occupied by an electron from the outer, higher energetic shell and the difference in electron energy between the energy levels is emitted as a characteristic X-ray, specific for each chemical elements, according to the Moseley's law [139].

$$v = \frac{3R_e}{4}(Z-1)^2 \qquad (13)$$

where v – frequency of the observed X-ray emission line; R_e – Rydberg constant; Z – atomic number.

2.3.3. Selected area electron diffraction (SAED)

SAED is a technique for determining, from a very small area, the crystallinity of the analyzed sample. The wavelength of high-energy electrons is significantly shorter compared to the spacing between the atoms of the sample. Thus, part of the electrons passing through the sample are scattered to particular angles, which are characteristic for the crystal structure of the sample. The remaining electron fraction passes through the specimen without deflection. The number of deflected electron beams varies with number of network planes with different hkl indices (so-called Miller indices) [140]. As a result, a diffraction patterns in the form of spots arranged at a distance proportional to λ/d for a single crystalline sample and in form of concentric rings with radius R (distance between the diffracted and transmitted beams in the diffraction pattern) for polycrystalline samples is generated (Figure 18). For amorphous samples, the diffraction pattern is composed of a blurred ring [136].
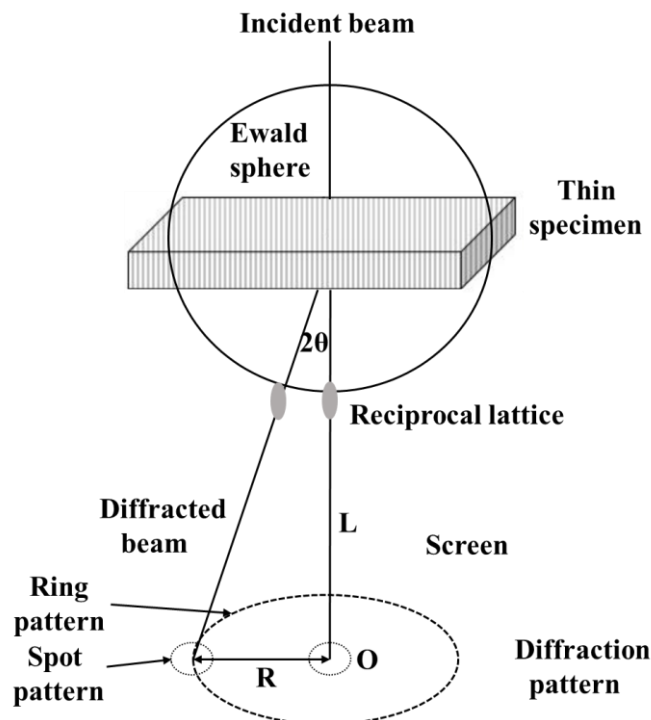
Figure 18. *The formation of a SAED patterns. Modified from* [140].

The electron diffraction can be described by the Bragg's law:

$$2dsin\theta = n\lambda \tag{14}$$

Based on Figure 18, it can be concluded that:

$$tg2\theta = \frac{R}{L} \tag{15}$$

where d – interplanar spacing; θ – the angle between incident and diffracted beams; λ – electron wavelength; n – the integer number of diffraction order; L – camera length; R – interplanar spacing.

Moreover, assuming very small diffraction angles and n = 1, the Bragg's law can be written as:

$$\lambda L = Rd \tag{16}$$

Knowing the above dependence, it is possible to easily calculate the interplanar spacing and therefore – identify the sample. The crystal structures of NPs were identified based on the ICDD (International Centre for Diffraction Data) database. The SAED diffraction patterns of Au NPs were indexed using the ICCD card nr 00-004-0784; of Pt NPs – the ICCD card nr 01-087-0646, of Pd NPs – the ICCD card nr 00-005-0681.

For our TEM observations (HAADF STEM, SAED and EDS), solutions of NPs purified and sonicated for 20 minutes were dropped on a Cu carbon film coated TEM grid (300 mesh). Then, the grid was rinsed with fresh ethanol and dried at room temperature. Before placing the samples in the TEM, they were cleaned in a plasma cleaner for 3 seconds. The morphology of the synthesized NPs was imaged by STEM using a HAADF detector operating in conventional and high-resolution (HRSTEM) modes. SAED patterns were taken in the TEM mode to assess the local crystallinity of the NPs. EDS was used to identify the local chemical composition of bi- (AuPd CSs, AuPd NRs and AuPt NPs) and trimetallic NPs (AuPdPt NPs). The STEM images processing was conducted by FEI TEM Imaging & Analysis Software. Bruker Esprit Software was used to analyze EDS data. By the Gatan Digital Micrograph software, the NPs size distribution and SAED patterns were analyzed. The size of the spherical NPs was evaluated by measuring the diameter of approximately 200 NPs. When the NPs were non-perfectly spherical in shape, their size was determined as the largest diameter of these NPs. For multicomponent NPs, the diameters of the outer shell were evaluated. The NPs size distribution was determined based on the images taken from different areas of the TEM grids.

The TEM measurements were performed on two microscopes:

- Aberration-corrected (Cs-corrected) FEI Titan electron microscope (Hillsboro, OR, USA) operating at 300 kV equipped with a FEG cathode located at the Faculty of Mechanical Engineering of the Silesian University of Technology. Overview STEM and HRSTEM images, as well as SAED patterns were acquired using this microscope.

- FEI Talos TEM (Waltham, MA, USA) operating at 200 kV equipped with a FEG cathode and four in-column EDS detectors (Super EDS system) located

at the University of Warsaw Biological and Chemical Research Centre. EDS mappings were performed using this microscope.

2.3.4. X-ray diffraction (XRD)

X-ray diffraction (XRD) was used to determine the global crystal nanostructure of the obtained NPs. Using this non-destructive method, it is also possible assessing the size of the nanocrystallites. For multicomponent NPs, it is possible to show that these NPs have a core shell structure. Figure 19 below shows the physical basics of the XRD method.
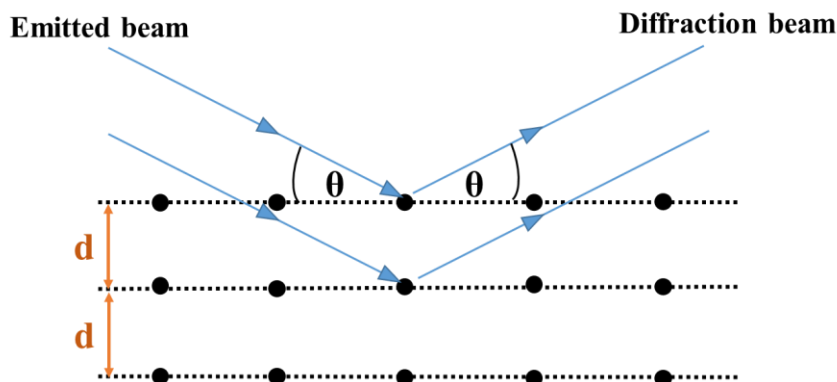
Figure 19. *Principle of the X-ray diffraction. Modified from* [141].

X-ray diffraction will only occur if Bragg's law (equation 14) is fulfilled. The fixed wavelength X-ray beam emitted from the source incides on the surface of the crystal at a fixed angle, and the generated diffracted X-ray beam is reflected under the same angle. To obtain an intense signal, the wavelengths of the scattered X-ray must interfere constructively, thus the differences in the optical path must be equal to integer multiples of the wavelength. These intense diffracted X-rays form the characteristic pattern, which is used to determine the crystal structure of the sample [142].

Powder XRD measurements of the NPs were carried out using a D8 Advance 800234 X-Ray (9829) Bruker (Billerica, MA, USA) at 40 kV and 40 mA located at the Binghamton University, Department of Chemistry. This instrument uses an X-ray tube producing Kα radiation at a wavelength of 1.5406 Å. Monochromatic X-rays are produced by the use of a Gobel mirror optics. The samples were tested at room temperature, in the range of 2θ from 30° to 80°. The size of NPs was calculated using the Scherrer equation:

$$D = \frac{0.94\lambda}{\beta cos\theta} \qquad (17)$$

where 0.94 – constant for spherical NPs in the cubic structure; λ – the wavelength used for XRD, which was 0.15406 nm; β – the full-width at half-maximum of the most intense peak; θ – angle of beam deflection. B and θ must be converted to radians before using them in the equation above. All reference crystallographic data were taken from ICDD database: 00-004-0784 (Au), 00-004-0802 (Pt) and 00-005-0681 (Pd).

2.3.5.   UV-Vis spectroscopy

UV-Vis (ultraviolet-visible) spectroscopy is a type of absorption spectroscopy using radiation in the range of ultraviolet and visible light. The absorbance of the energy in the UV-Vis range by the sample, may results in an electron transition from the ground state to a higher energy level. The absorbance can be determined from the Lambert-Beer law:

$$A = kcl \qquad (18)$$

where A – absorbance; k – molar absorption coefficient; c – molar concentration n; l – optical path length. The UV-Vis measurements of NPs were performed using a UV-2600 instrument from Shimadzu (Kyoto, Japan). For this purpose, 1 mL of each sample was measured with spectral resolution 1 nm and wavelength range between 200 nm and 900 nm.

2.3.6.   Zeta potential measurement

Zeta potential, or electrokinetic potential, is defined as the distribution of ions in the electrical double layer surrounding charged NPs, suspended in a solution (Figure 20). Schematically, the presence of a negative charge on the surface of a NPs, affects the distribution of ions in the adjacent region. Therefore, an increased concentration of ions with the opposite (positive) sign is observed, which are strongly associated with the surface of the NPs (so-called Stern layer). The latter layer, together with the outermost NPs-liquid interface layer, create an electric double layer. Thus, the potential formed at the slipping plane, separating the stable ion layer of ions from the ,,fuzzy layer", is the zeta potential [143].
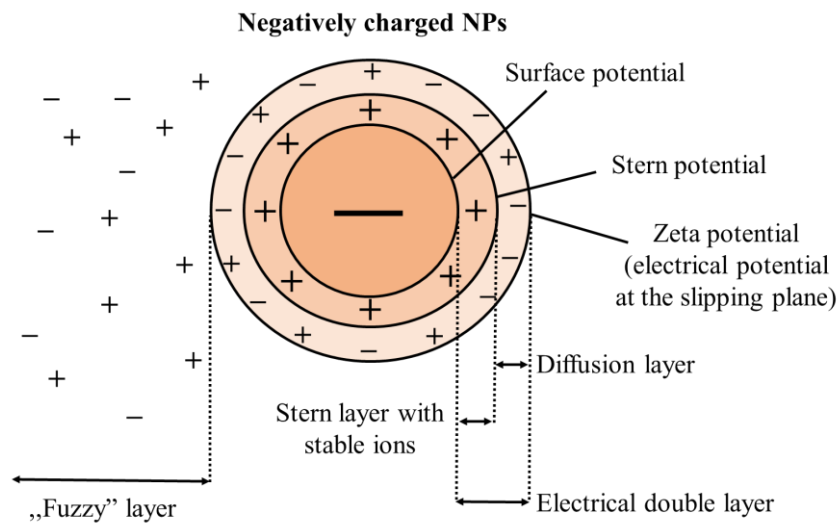
Figure 20. *Schematic representation of zeta potential. Modified from* [144].

The zeta potential is indirectly determined by measuring the electrophoretic mobility under an applied electrical field according to Henry's equation:

$$\frac{U}{E} = \frac{2\varepsilon\varsigma(K\alpha)}{3\eta} \qquad (19)$$

where U/E – electrophoretic mobility; ς – zeta potential; ε – dielectric constant; η – viscosity; F(Kα) – Henry's function varying between 1 and 1.5 [145].

To determine the zeta potential of the obtained NPs, each sample was placed in a viewing chamber and then the electric field was activated. The NPs in solution move towards the electrode of the opposite sign at a velocity proportional to their zeta potential. The zeta potential values of the synthesized NPs suspended in water (pH ≈ 7) were determined at room temperature by the microelectrophoretic method using Zetasizer Nano Series from Malvern Instruments (Worcestershire, UK) located at the Institute of Nuclear Physics Polish Academy of Sciences. The Smoluchowski model was used in zeta potential measurements.

2.3.7. Nanoparticle tracking analysis (NTA)

The nanoparticle tracking analysis (NTA) is a method, which allows fast visualization, size determination, polydispersity assessment and counting of NPs (NPs per ml) suspended in a solution. The NanoSight series analyzers (Figure 21) using the NTA technique do not require prior calibration.
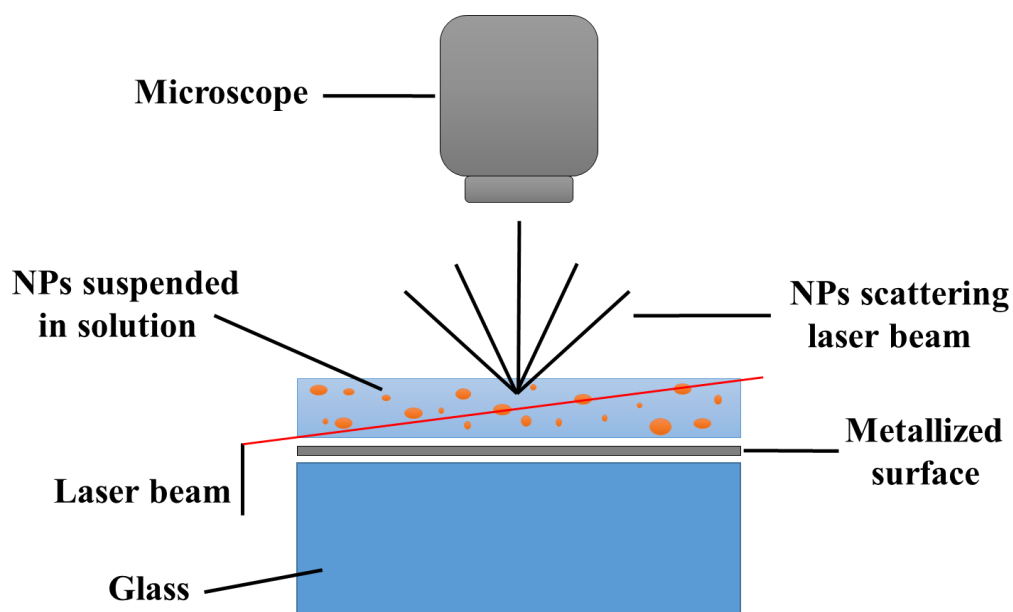
Figure 21. *NanoSight instrument configuration. Modified from* [146].

A sample of NPs is inserted into a measuring chamber containing a metallized element illuminated by a laser beam (480 nm). The laser beam illuminates the NPs flowing through the measuring chamber forced by a pump. The NPs being in Brownian motion scatter the illuminating laser beam. The velocity of the NPs depends on their size – smaller NPs move faster. The software records three one-minute movies of flowing NPs, on the basis of which the tracking and analysis of NPs is then carried out. The Brownian motion of each NPs is tracked, and then the diffusion coefficient (as a mean square of the NPs shift in the two planes x and y) is calculated (equation 20):

$$D_t = \frac{\overline{(x,y)}^2}{4} \qquad (20)$$

The NPs diameter, corresponding to the hydrodynamic diameter, can be determined from the Stokes-Einstein equation:

$$D_t = \frac{K_B T}{3\pi\eta d_h} \qquad (21)$$

where, D_t – diffusion coefficient; K_B – Boltzmann constant; T – thermodynamic temperature; η – viscosity; d_h – particle diameter [147].

The NTA was performed using NanoSight LM10-HS488FT14 Nanoparticle Characterization System from Malvern Instruments (Worcestershire, UK). 1 µl of NPs solution was diluted 1000x to a total volume of 1 ml in distilled water and then 600-700 µl of the sample was loaded into the measuring chamber using an insulin-type syringe. This syringe was then mounted onto the pump and the sample was flowed at a constant flow rate of 80 units. Next, three one-minute videos were recorded, and samples were analyzed using NanoSight NTA 3.0 analytical software (Malvern Instruments). The measurements were performed only for monometallic Au NPs and multicomponent NPs, as the microscope's resolution is 10 nm.

2.3.8. Charged-particle activation analysis (ChPAA)

Activation analysis is an analytical method for evaluation of trace elements concentration in the bulk of the sample. This method is based on the nuclear reaction induced in the sample by irradiating with e.g. photons, neutron or protons, leading to radionuclides specific for any given element. A simplified diagram of the charged-particle activation analysis (ChPAA) is shown in Figure 22.
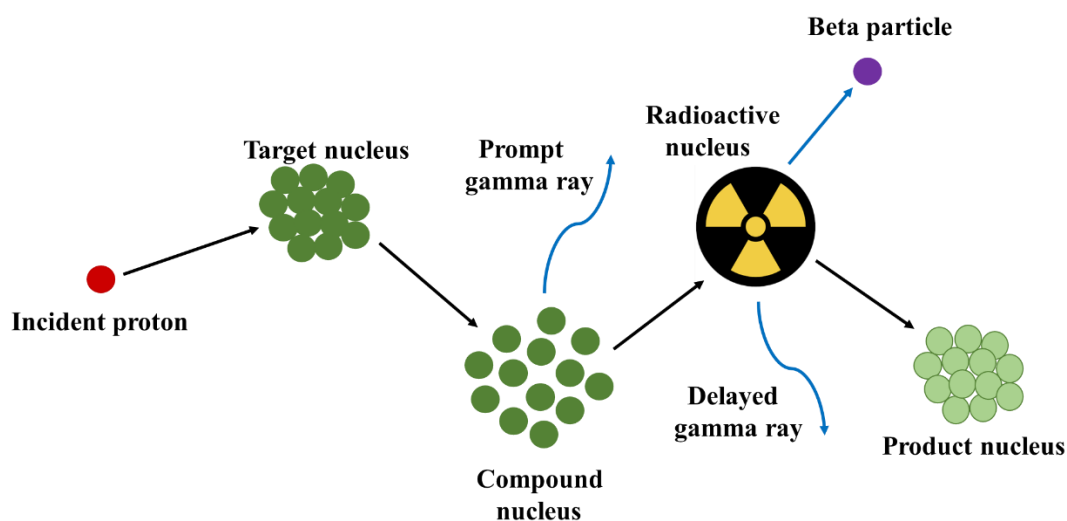
Figure 22. *Diagram illustrating the charged-particle activation analysis. Modified from* [148].

ChPAA uses a variety of nuclear reactions, simple ones as well as complex ones. The number of radioactive nuclides created per time unit in a nuclear reaction can be calculated using the following equation:

$$R = \int_{Emax}^{Emin} N_o \sigma(E) \Phi(E) dE \qquad (22)$$

where, N_o – number of target atoms of the nuclide taking part in the nuclear reaction; σ – differential cross-section; $\Phi \in dE$ – flux of NPs with kinetic energy between E and E+deE impinging on the sample.

By irradiating the sample nuclei, the reaction product may emit prompt gamma rays or additional particles. Protons can interact with nucleons, groups of nucleons or they can be absorbers and form so-called compound nuclei. If a radioactive nucleus is created, additional decay particles (e.g. beta particles) or decay gamma rays are emitted until a stable product nucleus is formed. Higher energy protons can induce various (p,a), (p,d) or (p,2n) nuclear reactions. Then they can deliver higher energies in the target nucleus, leading to greater heterogeneity of pathways for the de-excitation of activated nuclei [148].

First, the NPs solutions were irradiated with high-energy protons (15 Gy, 225 MeV) in 24-well plates. The ChPAA analysis was carried out using an ultra-low level gamma spectrometric system (Canberra, Atlanta, GA, USA) with a high purity germanium (HPGe) BE5030 detector equipped with passive (made from 1.5 cm of electrolytical copper, 5 cm of low background lead, 0.2 cm of cadmium, 10 cm of standard lead and 8-12 cm paraffin) and an active shield (five large plastic scintillation detectors sensitive to cosmic muons) with an aluminum free cryostat. The irradiated solutions were transferred to 15 ml Falcon tubes and placed into the spectrometer. Gamma rays emitted from the irradiated NPs solution were absorbed in the HPGe detector, generating electrical pulses, the amplitude of which is proportional to the energy deposited in the detector. Data acquisition was carried out using a digital analyzer CAEN DT5725 with CoMPASS Software.

2.4. Irradiation of colon cancer cells with proton beam

2.4.1. Cell culture

The effectiveness of the NPs-PIr was evaluated *in vitro* using the established cancer cell lines. Three colon cancer cell lines (SW480, SW620 and HCT116) were used in the study. The tested cell lines have a different level of malignancy/metastatic potential. The SW480 and SW620 isogenic cell lines were derived from the same patient – SW480 was obtained from the primary tumor (low metastatic ability), while SW620 – from a metastatic lesion to lymph node (high metastatic ability). HCT116 cell line is derived from the primary tumor, but is characterized by fast growth and high aggressiveness [149]. From the therapeutic point of view, it is important to assess, whether anticancer therapy damage normal cells, therefore a normal colon epithelium cell line CCD 841 CoN (CRL-1790, ATCC), was selected and used as a control.

SW480 and SW620 cells were cultured in DMEM with high glucose concentration. HCT116 cells were cultured in McCoy's 5A medium. The CRL-1790 cells were cultured in EMEM. All media were supplemented with 10 % fetal bovine serum and ciprofloxacin (10 µg/pl). The cells were cultured by bi-weekly passages in a 37°C humidified atmosphere

with 5 % CO_2 and regularly tested for *Mycoplasma* sp. contamination by the PCR-ELISA kit, according to the manufacturers' instruction.
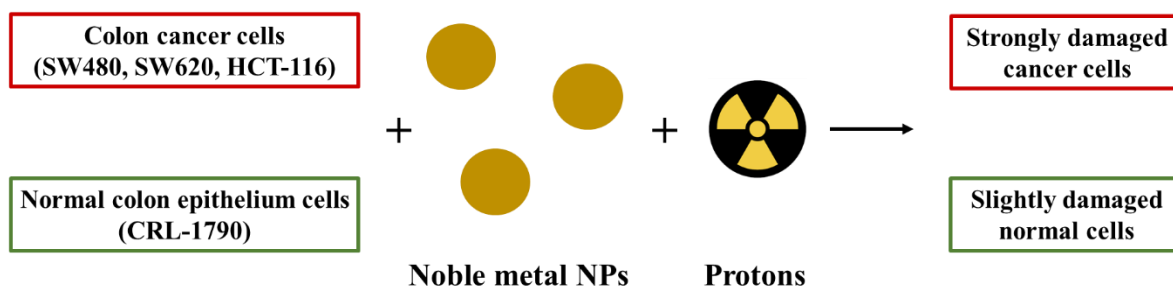
Figure 23. *General idea of the performed in vitro biological studies.*

The concept of biological research was as schematically shown in Figure 23. The cell lines were cultured with metallic NPs and subjected to PIr, but importantly the concentration of NPs and the radiation dose were selected in such a way, not to decrease the cell viability. Only the combined effect of NPs and PIr is expected. The justification for this type of complex therapy was elimination of cancer cells, while saving normal colon epithelium cells.

2.4.2. Proton beam irradiation protocol

Proton beam irradiation was performed in the Cycloctron Centre Bronowice, Institute of Nuclear Physics Polish Academy of Sciences. Prior to NPs-PIr, the non-toxic dose was determined using X-ray radiation. The PT system installed in the Centre consists of the IBA Proteus C-235 isochronous cyclotron (Ion Beam Applications, Louvain-la-Neuve, Belgium) with a compact conventional magnet and two gantries equipped with scanning nozzle. This cyclotron accelerates protons to the energy range from 70 MeV to 230 MeV using a classically generated magnetic field. Protons having 230 MeV are able to reach a depth of 30 cm in the human body, which allows to irradiate a tumor in any location. The pencil beam scanning (PBS) techniques, where a narrow proton beam is deflected in two perpendicular directions delivering the dose point by point to the whole target volume, was used for our research [150]. PIr was proceeded by dosimetry measurements performed with Markus type ionization chamber calibrated in terms of dose absorbed by water. PIr were carried out at room temperature using monoenergetic field with an energy 225 MeV and a field size of 20 cm x 20 cm. The cells were irradiated at 1.1 cm water equivalent depth, which consists of a 1 cm RW3 phantom plate with dose of 15 Gy. The gantry was set at 180 degrees, which means that the proton beam was coming from the bottom to the top. The depth-dose distribution of the 225 MeV proton beam, as well as the scheme of irradiation setup are shown in Figure 24.
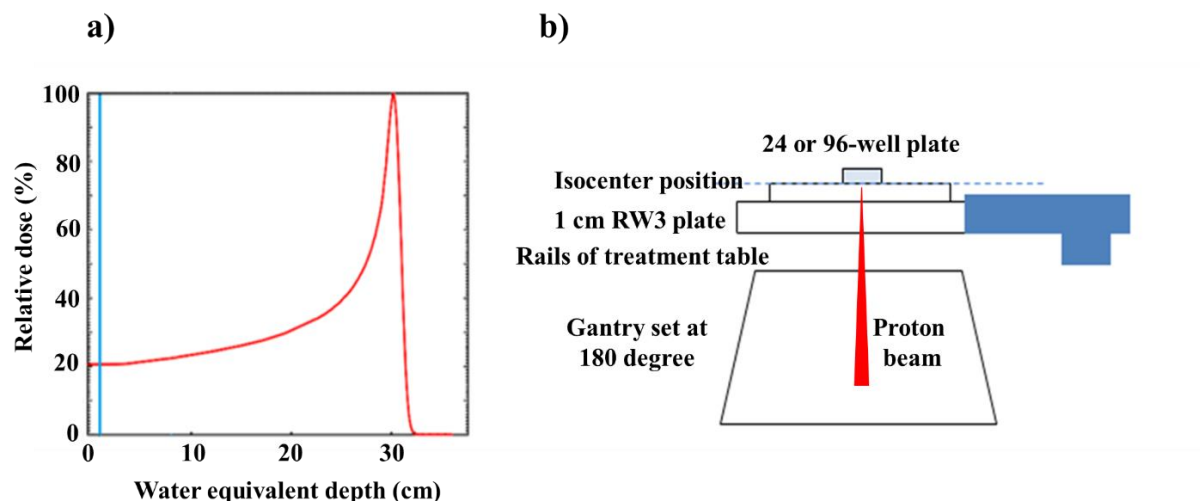
Figure 24. *a) Dose-depth plot for the applied PIr. The blue line represents the area that we use to irradiate the cells/NPs. b) A simplified scheme of the stand for irradiation with protons.*

2.4.3. MTS test

The colorimetric MTS test is commonly used in biological studies for assessment of cell viability. Its principle is based on the metabolic activity of viable cells, and more precisely – on the activity of the enzyme, mitochondrial dehydrogenase, converting a soluble substrate to formazan (Figure 25).
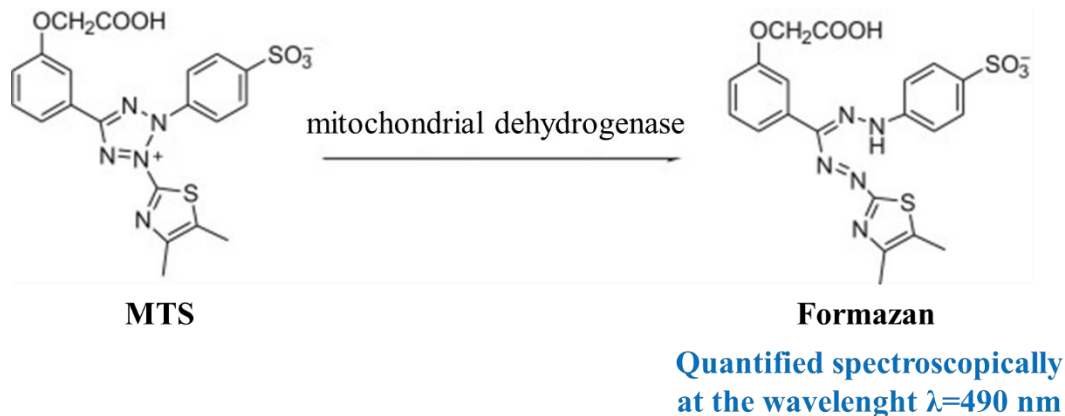
Figure 25. *The scheme of MTS-based cell viability assay.*

Formazan production can be quantified by UV-Vis spectroscopy at the wavelength of 490 nm and its amount is directly proportional to the number of viable cells. Cell viability (V) can be calculated by measuring the ratio of the absorbance of treated cells (ABS_x) to the absorbance of the control, untreated cells (ABS_C):

$$V = \frac{ABS_X}{ABS_C} \cdot 100\% \tag{23}$$

To evaluate the cytotoxicity of NPs, the cells were cultured in flat-bottom 96-well plates at a density of 1 x 10^4 per well. After 48 h of culture, 20 µl of NPs were added to 100 µl medium with cells. The final concentration of NPs in the medium ranged from 5 to 150 µg/ml. Then, after incubation period of 18 h, 20 µl of MTS dye solution was added per well. The absorbance was measured every half hour until its value stabilized (but not longer than 4 h). The quantity of formazan product was detected by absorbance measurements with a 96-well plate reader (Spark® Tecan, Mannedorf, Switzerland). Each sample was measured three times. Based on the MTS results, the maximum non-toxic concentration of individual NPs for each cell line was determined. **The non-toxic concentration was defined as the maximum concentration, which does not cause a significant decrease in cell viability not higher than 15 %**. Analogous experiments were also performed for 3 and 24 h incubation of cells with NPs. Moreover, the MTS assay was used to evaluate cell viability after the NPs-PIr. The general idea of this *in vitro* approach is presented below (Figure 26).
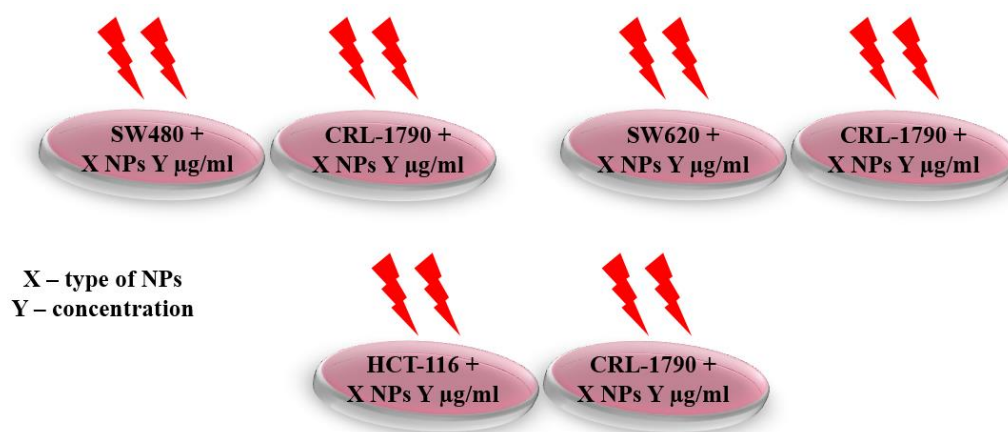
Figure 26. *The idea NPs-PIr.*

For NPs-PIr, cells were cultured with the determined non-toxic concentration of NPs. In turn, the normal CRL-1790 cell line (control) was treated with several NPs concentrations corresponding to individual non-toxic concentrations for the three cancer lines allowing a reliable comparison of the effect of PIr on normal and colon cancer cells.

The MTS results are shown as the means $\pm$ SEM (standard error of the mean). The data were analyzed by one-way analysis of variance (ANOVA) followed by *post hoc* Tukey test. Statistical significance was assumed when p-value < 0.05. The data were presented graphically using GraphPad Prism 8 Software.

2.4.4. Annexin-V binding and flow cytometry analysis

Flow cytometry is a powerful, analytical technique popular in biology and medicine, which enables rapid measurement of cell morphology (relative size and granularity) and fluorescence signals emitted by cells illuminated with the laser beam. The most popular application of this method includes immunophenotyping, cell cycle analysis, testing of cell apoptosis or monitoring of the cellular functions [151]–[154]. A simplified diagram of the flow cytometer is shown in the Figure 27.
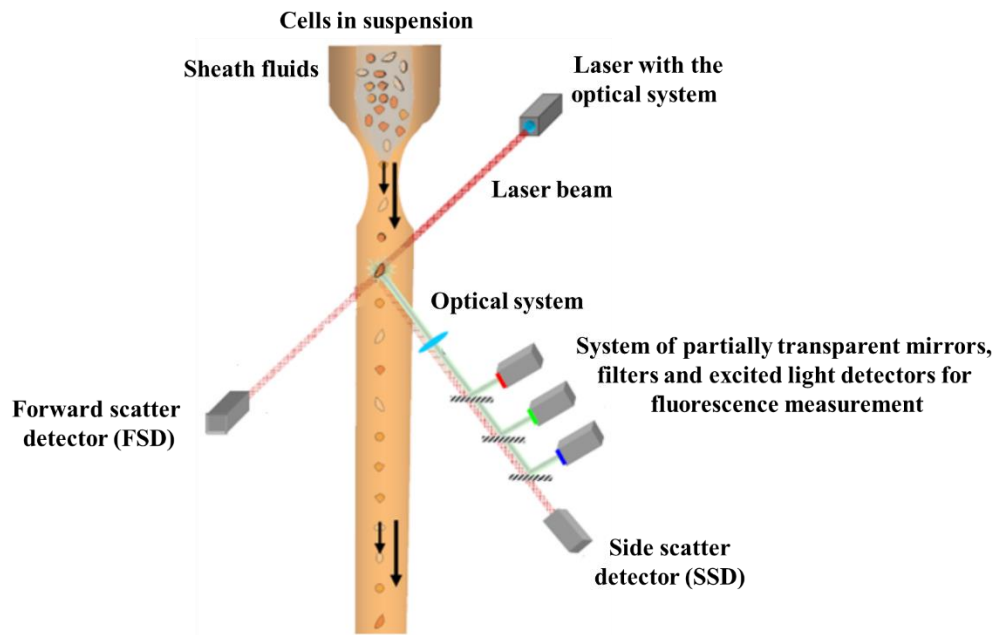
Figure 27. *Diagram of the flow cytometry. Modified from* [155].

In flow cytometry analysis, a cell suspension containing fluorescently labeled cells is injected into the cuvette, where the sample is focused by the Bernoulli effect, making the cells aligned in a single file in front of the laser. Then, the flowing cells are hitting the laser beam and the signals from the scattered light (corresponding to cell morphology) and fluorescence emitted by the cells (corresponding to cell phenotype and/or functions) are collected by dedicated detectors: forward scatter (FSD) and side scatter (SSD) detector, respectively.
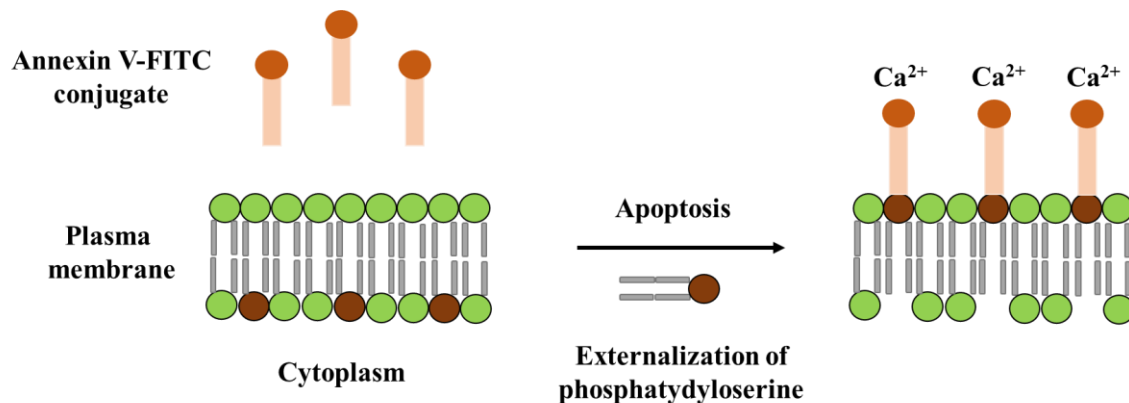
Figure 28. *Schematic representation of the Annexin-V assay.*

In the case of analysis of apoptotic cells by Annexin-V binding assay, the changes in the cell membrane organization are detected (Figure 28). The cell membrane of viable cells is characterized by asymmetry of the lipid bilayers and the presence of phospholipids i.e. phosphatidylserine (PS) on its inner part. When cells become apoptotic, the PS is externalized (early apoptosis marker) and a PS-specific protein – Annexin-V can be used to bind PS located in the outer part of the cell membrane. Annexin-V is conjugated

to the fluorescent dye, e.g. fluorescein isothiocyanate (FITC), allowing detection of the labelled cells in a flow cytometer.

To detect apoptotic cells after the treatment with NPs, the Annexin-V apoptosis detection kit was used. Cells were placed in a 24-well plate at the density of 1 x 10^6 per well/1 ml of appropriate medium. After 48 h of incubation, the non-toxic NPs concentration were added to the cells, which were subsequently irradiated with protons. After additional 18 h of incubation, the medium from each well was transferred in a pre-labeled separate centrifuge tube. Adherent cells from the same well were trypsinized (0.25 % trypsin solution in sterile PBS) and transferred to the same centrifuge tube containing NPs and non-adherent cells. All samples were centrifuged (1 200 x g, 10 minutes), and the supernatant were discarded. Pelleted cells were re-suspended in a solution containing FITC-conjugated Annexin-V and incubated for 10 minutes in the dark prior to analyzing by flow cytometry. Data from at least 10,000 cells were acquired. The results were analyzed using a FACS Diva v.8.1. and FlowJo v.10. software. All analyses were performed on a FACS Calibur flow cytometer (BD Biosciences, Immunocytometry Systems, San Jose, CA, USA) equipped with two lasers (488 nm and 635 nm) located at the Department of Clinical Immunology, Jagiellonian University Medical College.

2.5.   3D holotomographic microscopy of living cells

Holotomographic microscopy combines two techniques, holography and tomography. Nanolive 3D tool, is a microscope that enables the observation of changes in light propagation in biological materials (cells, blood, bacteria, etc.) allowing to obtain a three-dimensional matrix of the refractive index (RI) distribution. The holography allows to measure the optical phase delay of light that passes through a sample of a given thickness and distribution of RI values. In turn, tomography allows to reconstruct the 3D distribution of RI values and gives chemical and structural information about the sample. Using the holotomographic microscopy, the internal, three-dimensional structure of biological materials can be observed in nanometric resolution: below 200 nm in X-Y and 400 nm in Z axis [156]. Compared to other microscopic methods, the sample preparation for analysis in Nanolive does not require labeling or modifying the studied sample and low-energy light passes through the sample with minimal perturbation [157]. The device has also a built-in mini-incubator, providing optimal conditions for cells, so that the measurements of living cells can be carried out up to several days. Thus, holotomographic microscopy can be used to assess changes in the morphology of cells treated, for example, with NPs, to determine the charge-dependent dynamics of NPs penetration into cells, as well as to determine the location of their accumulation in or on the cells, and many others.

A scheme of the holotomographic microscope operation with an exemplary photo of a 3D Cell Explorer (Nanolive) is shown in Figure 29.
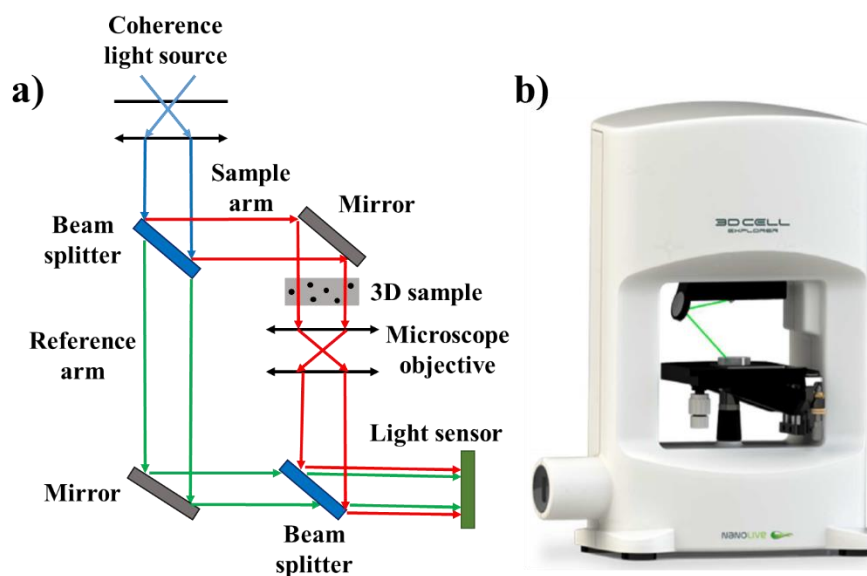
Figure 29. a) *Schematic principle of holotomographic microscope. b) An example of a holotomographic microscope Nanolive 3D Cell Explorer. Modified from* [158].

The measurements were performed using the holotomographic 3D Cell Explorer-Fluo (Nanolive, Tolochenaz, Switzerland) microscope equipped with a x 60 magnification objective, $\lambda = 520$ nm, sample exposure 0.2 mW/mm^2 and field depth of 30 µm, located at the Institute of Nuclear Physics Polish Academy of Sciences used for the generation of RI-based 3D holotomographic images. During the analysis, the sample, positioned above a high-numerical-aperture air objective, is irradiated with low-power green lasers an angle of approximately 45º. Then, the illumination arm rotates 360º around the sample. It is worth emphasizing that the microscope construction minimizes the phototoxic effect of this laser on living cells or other biological materials. A series of holograms is recorded by combining the beam that has passed through the specimen with the reference beam. The obtained holographic images are processed to obtain 3D rendered holotomograms using STEVE® Software.

In the present study, only the interaction between Pd NPs and cells from the four investigated cell lines was investigated. Previously, the non-toxic NPs concentrations were established and used in these experiments (see paragraph 2.4.3.). The cells were placed in a 96-well plate (special for fluorescence imaging, with glass coverslip bottom, minimal background noise and crosstalk between wells) and transferred into the mini-incubator coupled to the Nanolive device. Then the NPs were added to the cell cultures. The cells were holotomographically imaged after 1, 6 and 18 h. The 3D holotomographic and z-axis images were reconstructed based on the RI value using the STEVE® software, allowing to observe NPs accumulation regions in the cells.

Chapter 3: Results

3.1. Evaluation of morphology, structure and other properties of NPs

3.1.1. Monometallic Au, Pt and Pd NPs

a) Au NPs

STEM microscopic analysis, presented in Figure 30a, confirmed that not agglomerated, nearly spherical Au NPs are obtained. The NPs are crystalline with lattice fringes visible in the HRSTEM image (Figure 30b). The NPs are not perfect crystals, in all of them defects, such as stacking faults or twinning, are visible. The size distribution of the Au NPs was small around 16 nm (Figure 30c).
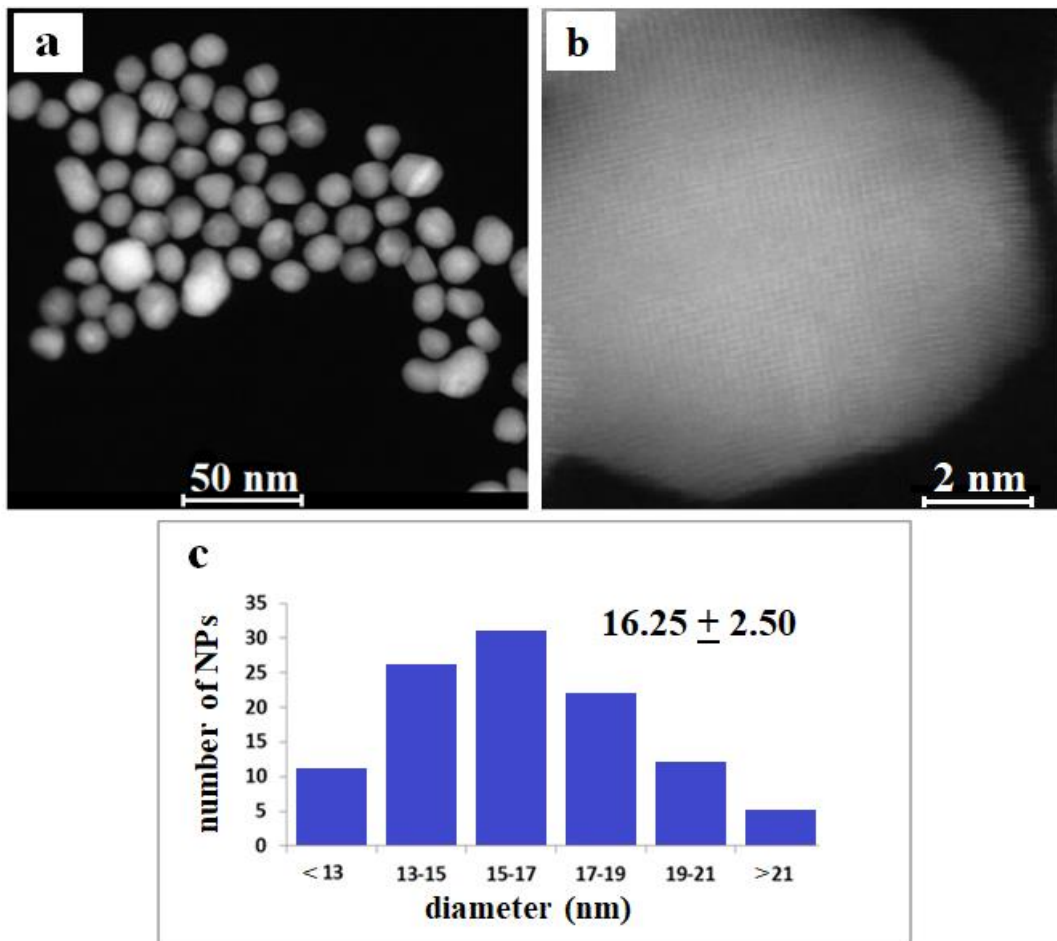
Figure 30. *a) HAADF STEM overview image. b) HRSTEM image. c) size distribution of Au NPs.*

The Au NPs structure is locally assessed by SAED (Figure 31a). The SAED patterns confirmed, similarly to HRSTEM images, that Au NPs have a crystalline structure. The spots in the diffraction pattern originate from the larger Au NPs. The rings of SAED can be attributed to the (111), (200), (311) and (222) lattice planes of face-centered cubic Au NPs.
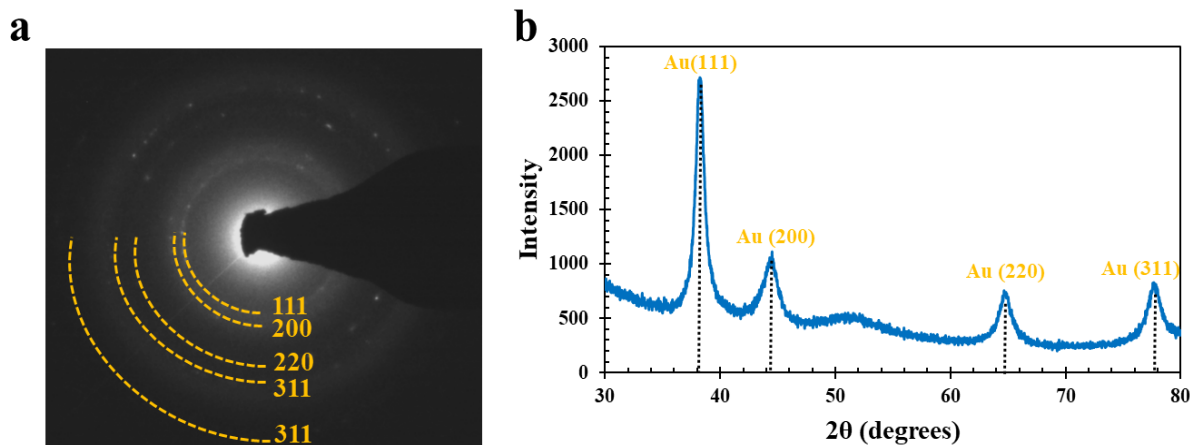
Figure 31. *a) SAED patterns of the Au NPs indexed with lattice parameters of gold. b) XRD diffractogram of Au NPs.*

Additionally, the global microstructure of Au NPs was assessed by powder XRD. Four diffraction peaks can be observed in the XRD pattern (Figure 31b). These reflections were present at 38.24°, 44.51°, 67.42° and 77.79° corresponding to (111), (200), (220) and (311) lattice planes. The peaks are also in good agreement with the standard values (ICDD, 00-004-0784), indicating that Au NPs have a fcc structure. The intensities of the peaks were compared to the intensity of the (111) plane. The (200)/(111) ratio was calculated to be 0.41, the (220)/(111) ratio was calculated to be 0.27 and the (311)/(111) ratio was calculated to be 0.30. All of these values are lower than the standard values of 0.53, 0.33 and 0.37, respectively (ICDD, 00-004-0784). This shows that the Au NPs are dominated by the (111) plane. Au NPs were calculated to have an average size of 10 nm. This value is close to what is observed in the TEM images.
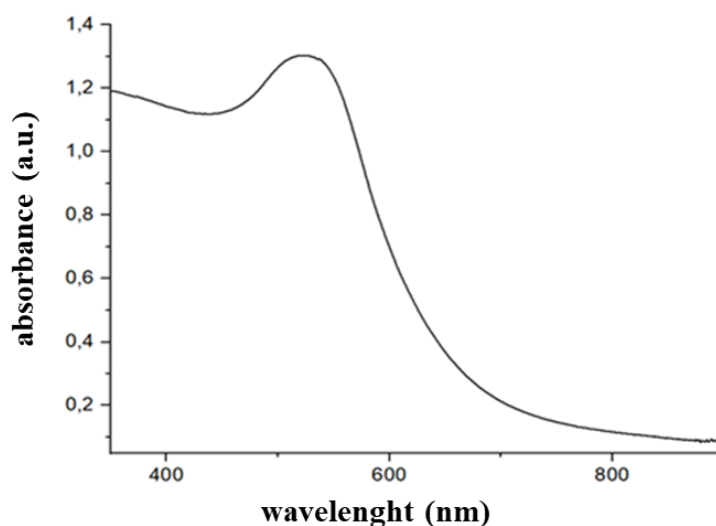
Figure 32. *UV-Vis spectrum of Au NPs.*

The optical properties of Au NPs were determined by UV-Vis spectroscopy. In the UV-Vis spectrum (Figure 32) a peak at 525 nm is visible. This peak is characteristic for spherical Au NPs. It is worth noting that the position of this maximum absorbance depends on the Au NPs shape [159], [160].

The zeta potential value of Au NPs was estimated to be – 17.40 mV. The diameter of NPs determined by the NTA method (Figure 33) is about 228 nm, which definitely differs from the diameter determined by TEM and XRD.

Results

Stats: Mean +/- Standard Error

Mean:	228.5 +/- 4.8 nm
Mode:	271.2 +/- 75.1 nm
SD:	107.7 +/- 1.2 nm
D10:	105.2 +/- 6.0 nm
D50:	198.5 +/- 4.0 nm
D90:	376.0 +/- 10.1 nm
Concentration:	5.44e+008 +/- 1.94e+007 particles/ml
	27.6 +/- 1.0 particles/frame
	33.4 +/- 0.9 centres/frame
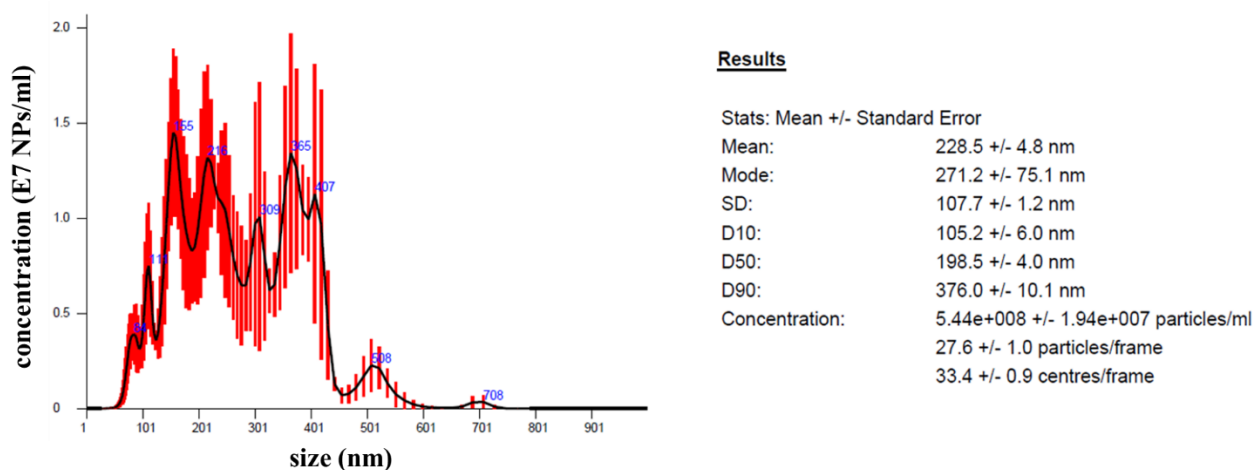
Figure 33. *NTA results for Au NPs.*

b) Ultra-small Pt NPs

STEM images (Figure 34a) revealed that ultra-small, monodisperse Pt NPs having the diameter of approximately 2 nm are obtained (Figure 34c). In the HRSTEM image (Figure 34b) the atomic lattice in the NPs is visible, proves their crystalline structure. Each NPs is a perfect single crystal – no defects inside the NPs are visible. Moreover, although the NPs seem to be slightly agglomerated, they form a monolayer on the carbon support of the TEM grid.
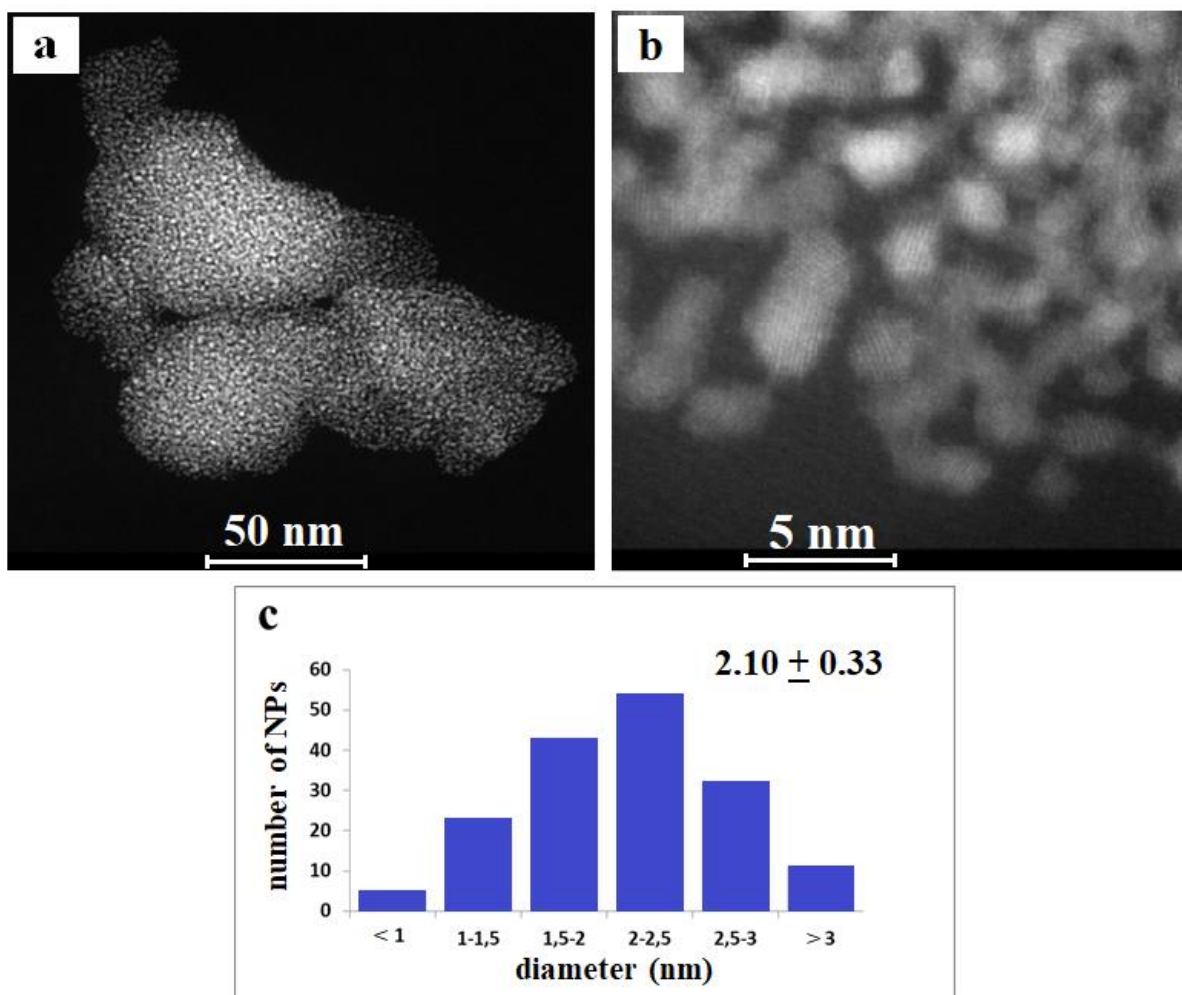
Figure 34. *a) HAADF STEM overview image. b) HRSTEM image. c) size distribution of ultra-small Pt NPs.*

The SAED diffraction rings (Figure 35a) were indexed with the (111), (200) and (220) planes of fcc platinum. These results are in agreement with XRD patterns shown in Figure 35b. Three different peaks were observed at 39.96°, 46.40° and 67.78° corresponding to the (111), (200) and (220) lattice planes, respectively. This shows that Pt NPs are crystalized in a fcc structure. The peaks are in good agreement with the standard values (ICDD, 00-004-0802). The (200)/(111) ratio was calculated to be 0.44 and the (220)/(111) ratio was calculated to be 0.25. Both of these values are lower than the standard values of 0.53 and 0.32, respectively. This means that these NPs are mainly oriented in the (111) plane. The size of the Pt NPs is calculated to be 9.3 nm, which in not in agreement with the TEM characterization showing an average size of 2 nm. However, this discrepancy may be due to the fact that, these small NPs form larger clusters, as seen in Figure 34a, which may falsify the XRD results. In addition, multiple sample centrifugation was required to prepare the samples for the powder XRD, which could result in stabilizer removal and NPs agglomeration.
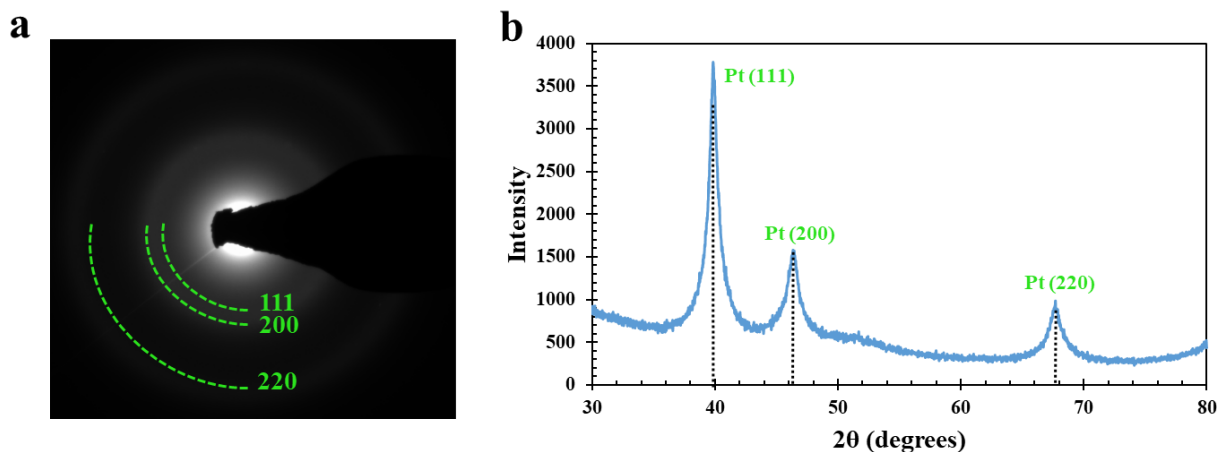
Figure 35. *a) SAED patterns of the Pt NPs indexed with lattice parameters of platinum. b) XRD diffractogram of Pt NPs.*

The UV-Vis spectrum (Figure 36) does not show any maximum in the tested range, which is consistent with the literature [161].
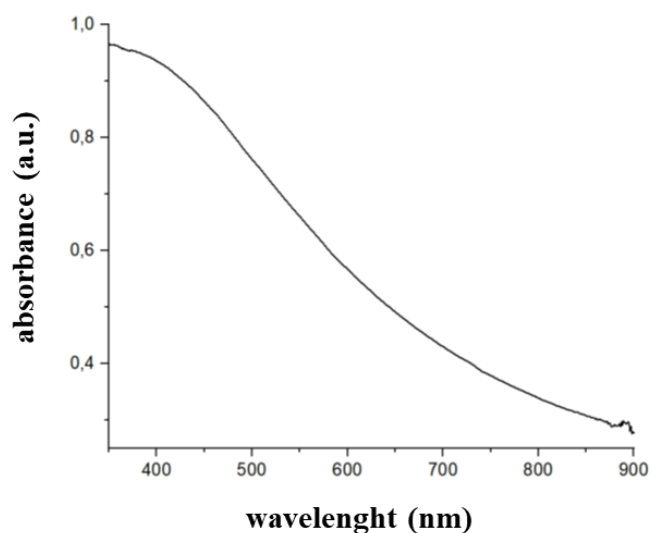
Figure 36. *UV-Vis spectrum of Pt NPs.*

The value of the zeta potential of ultra-small Pt NPs is approximately – 11.28 mV.

c) Ultra-small Pd NPs

The STEM image in Figure 37a and b, shows small, ≈ 2 nm, monodisperse and non-agglomerated spherical Pd NPs. HRSTEM images confirm the crystalline structure of these NPs, as lattice fringes are visible in the individual NPs. SAED patterns from the Pd NPs (Figure 38a) showed that the ultra-small Pd NPs have a crystalline structure. The rings are rather blurred, which indicates a very small NPs size. As the NPs have a very uniform size, no bigger NPs are present, no spots are visible in the SAED pattern. The global crystalline structure of the fabricated Pd NPs was also confirmed by XRD studies (Figure 38b). The observed XRD peaks at 40.02°, 46.62° and 68.32°, match perfectly the standard Bragg reflections (111), (200)

and (220) (ICDD, 00-005-0681). This also demonstrates that palladium has a fcc structure. The calculated intensities ratios are 0.58 and 0.37 for (200)/(111) and (220)/(111) ratios, respectively. These values are higher than the standard values of 0.42 and 0.26 indicating that the NPs has more (200) and (220) planes compared to standard (ICDD, 00-005-0681). These calculated NPs size is in around 12.8 nm. This is much higher than the TEM characterization showing an average size of approximately 2 nm. These discrepancies can be explained in the same way as for ultra-small Pt NPs.
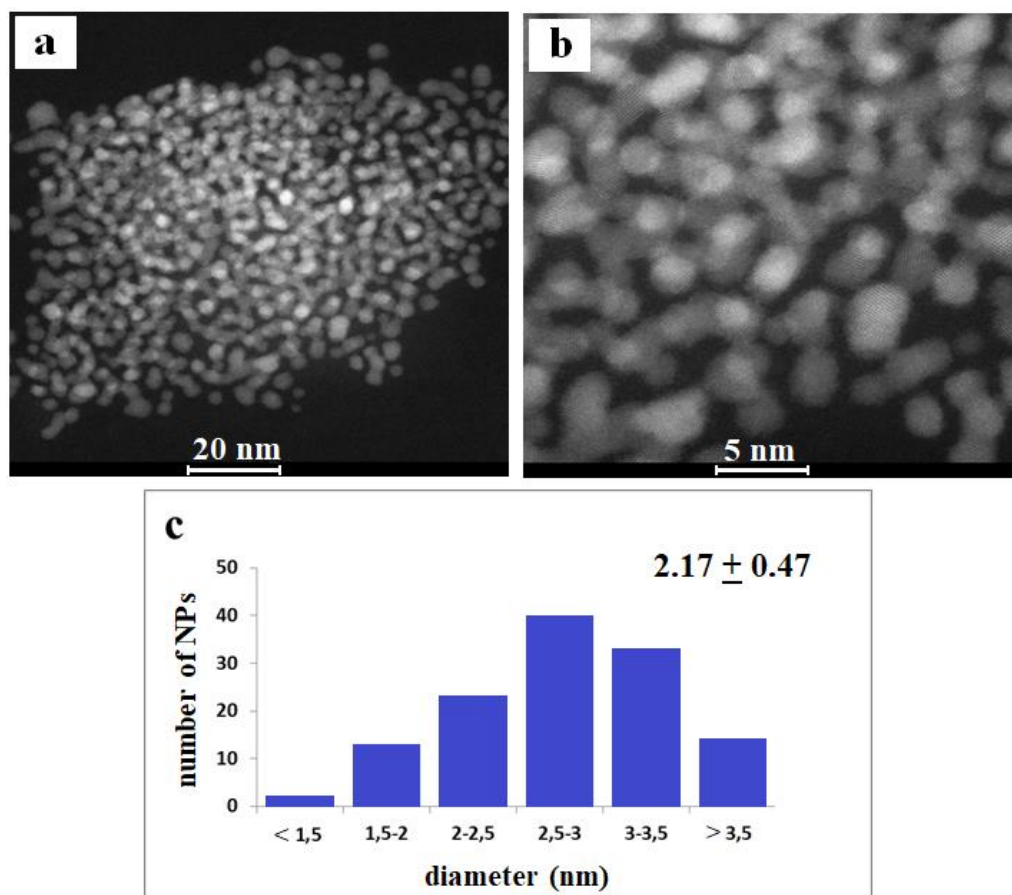
Figure 37. *a) HAADF STEM overview image. b) HRSTEM image. c) size distribution of ultra-small Pd NPs.*
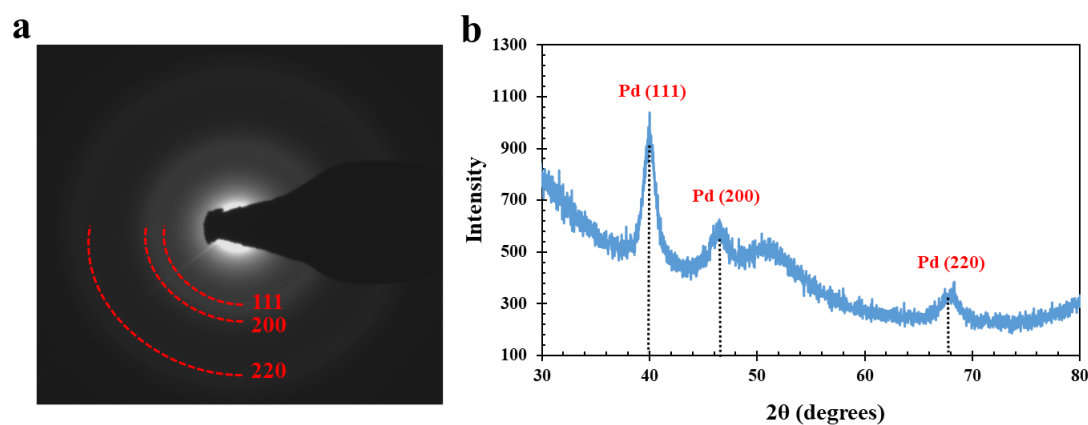
Figure 38. a) *SAED patterns of the Pd NPs indexed with lattice parameters of palladium. b) XRD diffractogram of Pd NPs.*

In the UV-Vis spectrum (Figure 39) of Pd NPs no maximum was noticed. This is consistent with the literature [162].
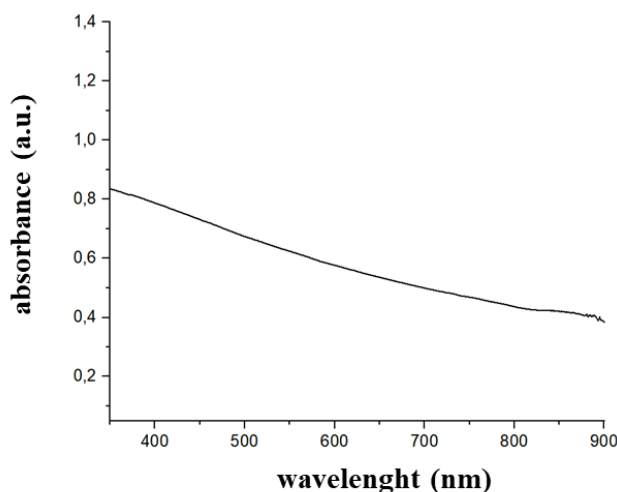
Figure 39. *UV-Vis spectrum of Pd NPs.*

The zeta potential value of ultra-small Pd NPs was estimated at + 12.49 mV.

3.1.2. Bimetallic NPs: decorating Au NPs with smaller Pt or Pd NPs

3.1.2.1. Comparison of AuPd core-shell and porous AuPd nanoraspberry-like NPs

The HAADF STEM of the AuPd CSs is shown in Figure 40a1. The gold core is clearly distinguishable, as it has a strong contrast due to its higher Z number (Z_{Au} = 79) compared to Pd (Z_{Pd} = 46). The spherical Au cores have a diameter of $\approx$ 16 nm and are surrounded by a continuous, thin $\approx$ 2 nm shell of palladium. The size distribution of the AuPd CSs is relatively narrow varying between 17 and 23 nm (Figure 40a2).
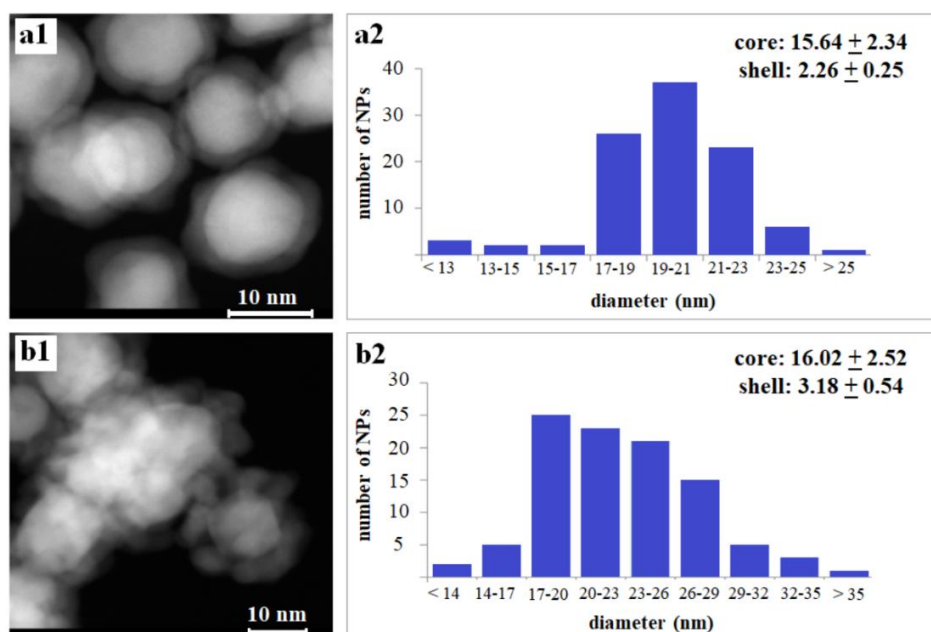
Figure 40. *HAADF STEM images of a1) AuPd CSs and b1) AuPd NRs) with the corresponding size distributions (a2, b2).*

The AuPd NRs (Figure 40b1-b2) have similar in sizes and shapes, with the difference that the palladium shell is porous. Small, 2 nm palladium spheres decorated the gold surface forming structures similar to raspberries. The distribution of Au and Pd in the respective types of NPs is shown on the EDS maps shown in Figure 41a1-a4 – for AuPd CSs and Figure 41b1-b4 – for AuPd NRs.
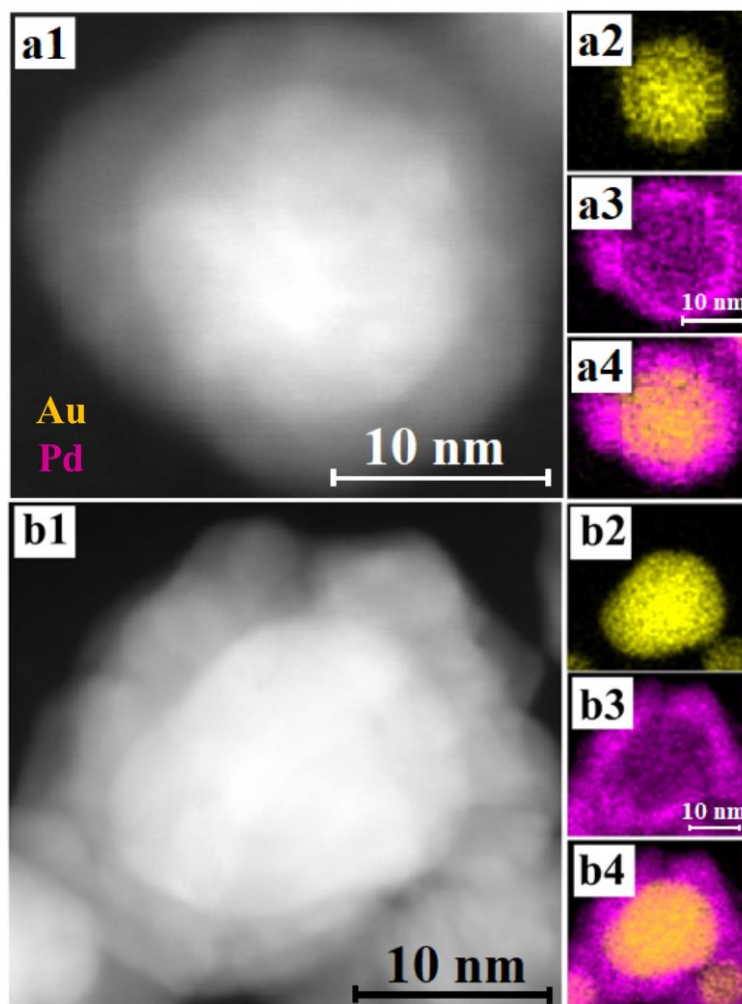
Figure 41. *STEM images of a1) AuPd CSs and b1) AuPd NRs with the corresponding individual EDS distribution maps of: a2, b2) gold, a3, b3) palladium and a4, b4) superposed gold and palladium in AuPd NPs.*

The above EDS maps for both types of AuPd NPs clearly indicate that gold is located only in the core and palladium forms the shells – continuous and smooth for AuPd CSs and uneven, porous for AuPd NRs.

Figure 42 presents the SAED and XRD patterns for the AuPd CSs (Figure 42a1 and a2) and AuPd NRs (Figure 42b1 and b2). For both structures, SAED patterns confirm a crystalline, fcc structure of the NPs, as the diffraction pattern consists of double rings. The latter ones originate from the superposition of the diffraction from the gold core, as well as from the palladium shell. The spots in the diffraction rings are formed due to the larger size of some individual NPs.
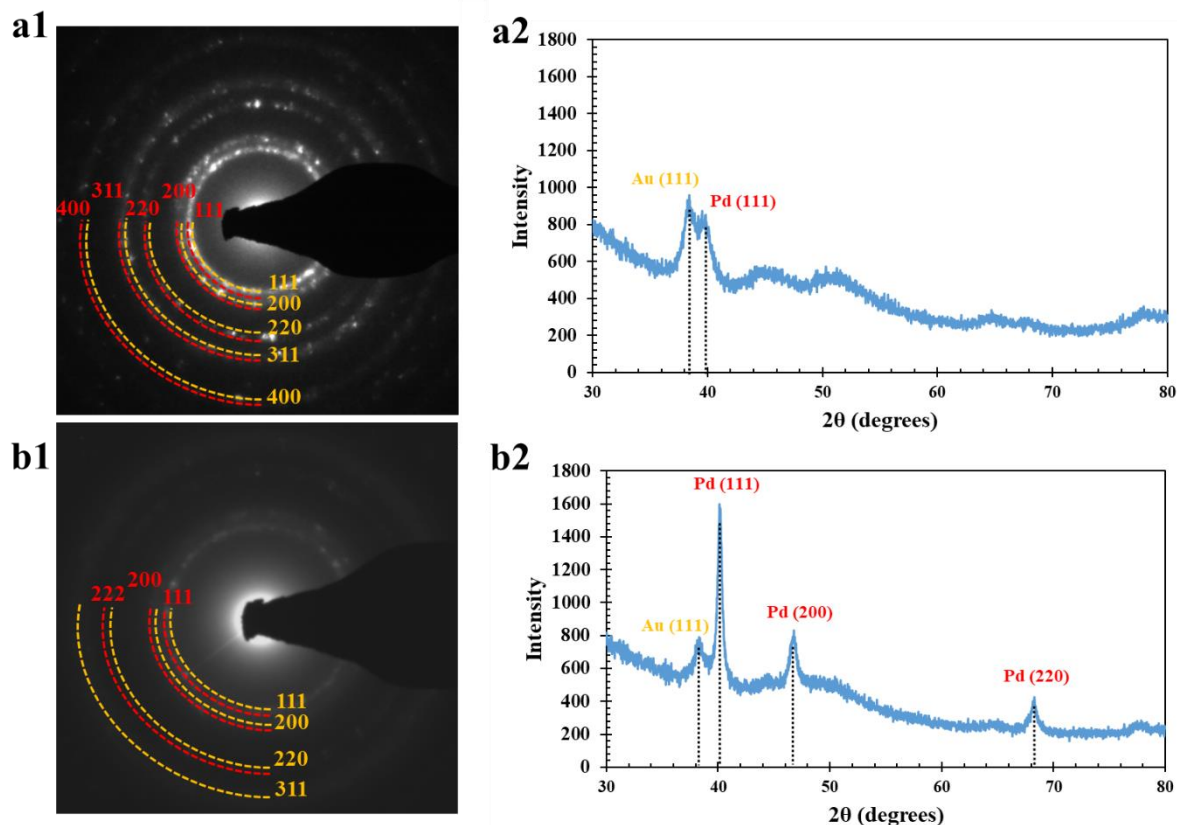
Figure 42. *SAED patterns of the a1) AuPd CSs and b1) AuPd NRs indexed with lattice parameters of gold and palladium and XRD diffractogram of a2) AuPd CSs and b2) AuPd NRs. Au peaks are marked in yellow, while Pd peaks in red.*

On the XRD diffractogram for AuPd CSs (Figure 42a2), there is one high intensity double peak observed at 38.46° and 39.86°, which is observed when two separated phases constitute the sample. The peak at lower angles corresponds to the (111) plane of gold. The peak at 39.86° originates from the (111) plane of palladium. These peaks are in good agreement with standard values (ICDD, 00-004-0784 and 00-005-0681). The peaks visible at around 45°, 64.5° and 77.5° corresponding to the (200), (220) and (311) planes are broader, most probably due to the fact, that Pd is covering the Au core, and additionally the Pd shell might not be perfectly crystallized. The NPs calculated size was to be ≈ 13.5 nm. This value is however lower than indicated by TEM. In turn, for AuPd NRs, four diffraction peaks located at 38.28°, 40.19°, 46.85° and 68.26° are observed (Figure 42b2). The peak at the lowest angle corresponds to the (111) plane of gold and the three peaks at higher angles originate from palladium (111), (200) and (220) planes (ICDD, 00-004-0784 and 00-005-0681). These peaks confirm the fcc structure of the AuPd NRs. The intensities for the palladium peaks were compared to standard values. The ratio for (200)/(111) was calculated to be 0.50 and the ratio for (220)/(111) was calculated to be 0.27. These values are close to the standard values of 0.53 and 0.32. Other gold peaks can almost be seen around 44.5° and 77.5°. However, these are not well defined. These NPs were calculated to have an average size of 17.1 nm. This calculation was in line with the value obtained from TEM imaging.

Figure 43 shows the UV-Vis spectra for both AuPd CSs and AuPd NRs samples. In the spectrum of the AuPd CSs (Figure 43a) no peak was observed, meaning that Pd NPs covered the entire Au NPs surface. This is an additional proof that a AuPd core-shell structure was obtained. In turn, for AuPd NRs (Figure 43b) a very low intensity peak at 525 nm was detected, meaning that the Pd NPs did not cover the entire Au NPs surface.
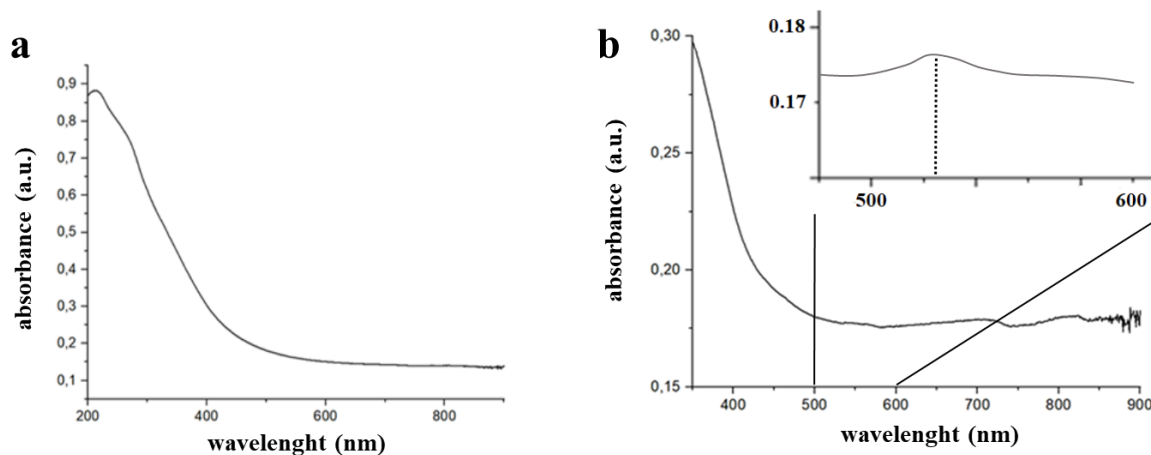
Figure 43. *UV-Vis spectra of a) AuPd CSs and b) AuPd NRs.*

The measured zeta potential value was – 16.99 mV and + 2.66 mV for AuPd CSs and AuPd NRs, respectively. Figure 44a and b show the estimated diameter of AuPd CSs and AuPd NRs obtained by the NTA. These values, however, significantly differed from the actual diameters of the NPs.
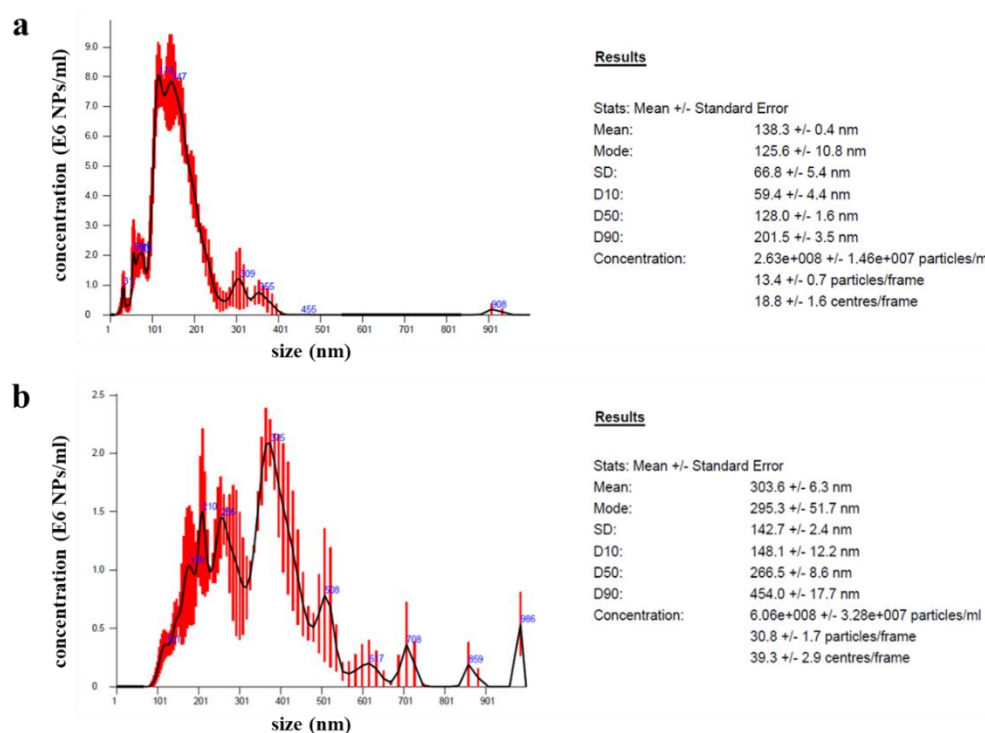
Figure 44. *NTA results for a) AuPd CSs and b) AuPd NRs.*

3.1.2.2.   Characterization of bimetallic platinum-decorated gold NPs

Figure 45a1 shows the HAADF STEM image of the obtained AuPt NPs having an approximate diameter of 22 nm, as shown in Figure 45b. The NPs consist of a spherical Au core with a bright contrast, $Z_{Au} = 79$ decorated by small, ≈ 3 nm spherical Pt NPs with $Z_{Pt} = 78$. Although the difference in the atomic number values is very small, it is possible to distinguish between Au and Pt in the HAADF images. The EDS maps (Figure 45a2-a4) show the distribution of Au and Pt, confirming that the Pt NPs are decorating the surface of the Au cores.
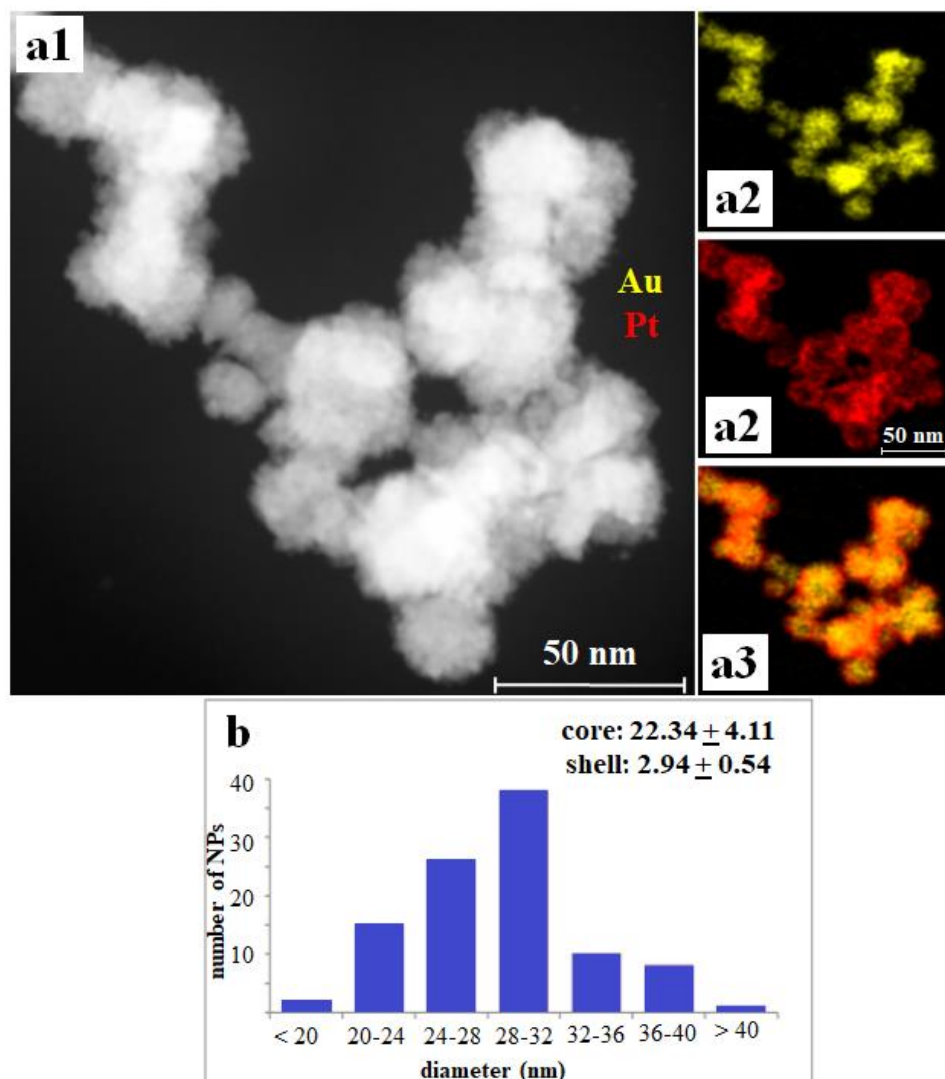
Figure 45. *a1) STEM image of AuPt NPs with the corresponding individual EDS maps of distribution of a2) gold, a3) platinum and a4) superposed gold and platinum. b) size distribution of AuPt NPs.*

The structural information for the AuPt NPs was obtained from SAED patterns (Figure 46a) and XRD (Figure 46b). The SAED patterns confirmed that the AuPt NPs have a crystalline structure. The double rings in the SAED patterns correspond to (111), (200), (220) and (311) lattice planes of gold and platinum with fcc lattice.
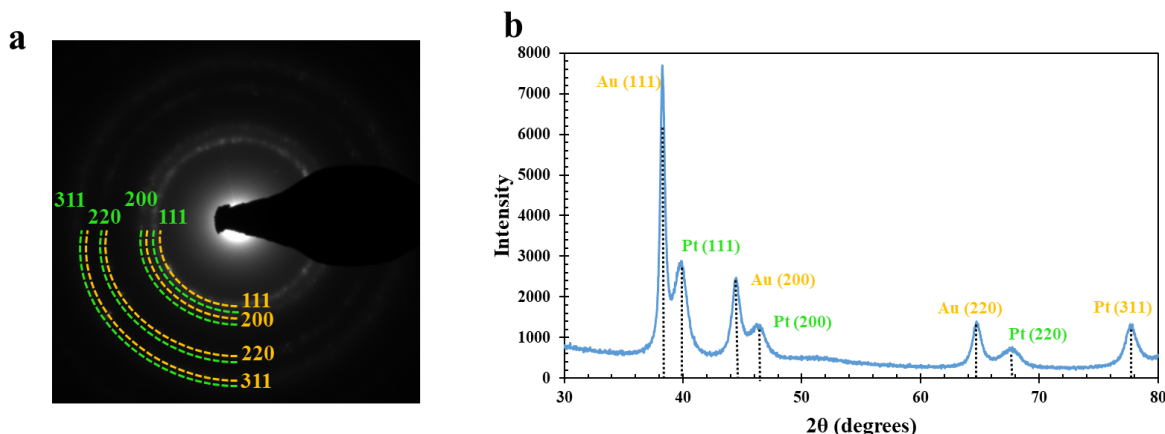
Figure 46. *a) SAED patterns of the AuPt NPs indexed with lattice parameters of gold and platinum. b) XRD diffractogram of AuPt NPs. Au peaks are marked in yellow, while Pt peaks in green.*

The XRD diffractogram for AuPt NPs is presented in Figure 46b. Four peaks at 38.28°, 44.53°, 64.74°, and 77.67° confirm the fcc structure of gold with (111), (200), (220), and (311) planes, which is in good agreement with the standard values (ICDD, 00-004-00784). The other three peaks originate from the fcc structure of platinum: 39.86°, 46.56°, and 67.75° which are also in good agreement with the standard values (ICDD, 00-005-0681). The latter peaks correspond to the (111), (200), (220), and (311) planes of Pt, respectively. The comparison of the peak intensities for gold was calculated to be 0.31, 0.18, and 0.17 for (200)/(111), (220)/(111), and (311)/(111) ratios, respectively. These values are well below the standard values of 0.53, 0.33, and 0.37 (ICDD, PDF 00-004-0784), showing that the NPs are preferentially oriented in the (111) plane, compared to the standard values. Conversely, no huge difference from the standard values for the platinum intensities was observed. The values calculated were 0.44 and 0.27, respectively. The standard values are 0.42 and 0.26 for (200)/(111) and (220)/(111) (ICDD, PDF 00-005-0681). The average size of NPs was calculated to be 16.8 nm. This is in line with the TEM characterization showing an average size of 18.7 ± 4.7 nm.

In the UV-Vis spectrum of AuPt (Figure 47) no peak was observed, documenting that Pt NPs covered the entire Au NPs surface.
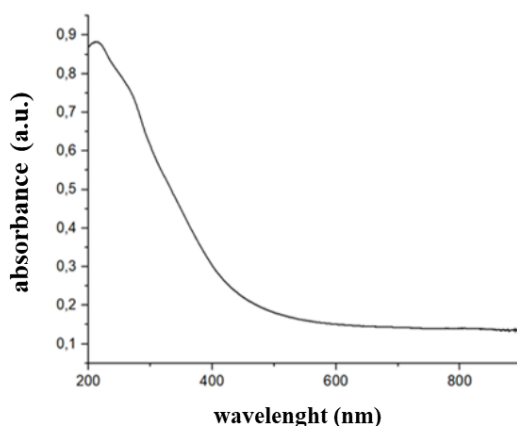
Figure 47. *UV-Vis spectrum of AuPt NPs.*

The value of zeta potential of AuPt NPs was estimated as -7.26 mV. Similarly to Au NPs and bimetallic AuPd NPs, in the case of AuPt NPs, their diameter determined by NTA was overestimated by several times (Figure 48).

Results

Stats: Mean +/- Standard Error
Mean:	115.2 +/- 2.5 nm
Mode:	147.6 +/- 26.3 nm
SD:	62.2 +/- 3.3 nm
D10:	34.3 +/- 2.0 nm
D50:	102.5 +/- 6.4 nm
D90:	206.9 +/- 9.4 nm
Concentration:	1.43e+008 +/- 3.50e+006 particles/ml
	7.2 +/- 0.2 particles/frame
	10.5 +/- 0.3 centres/frame
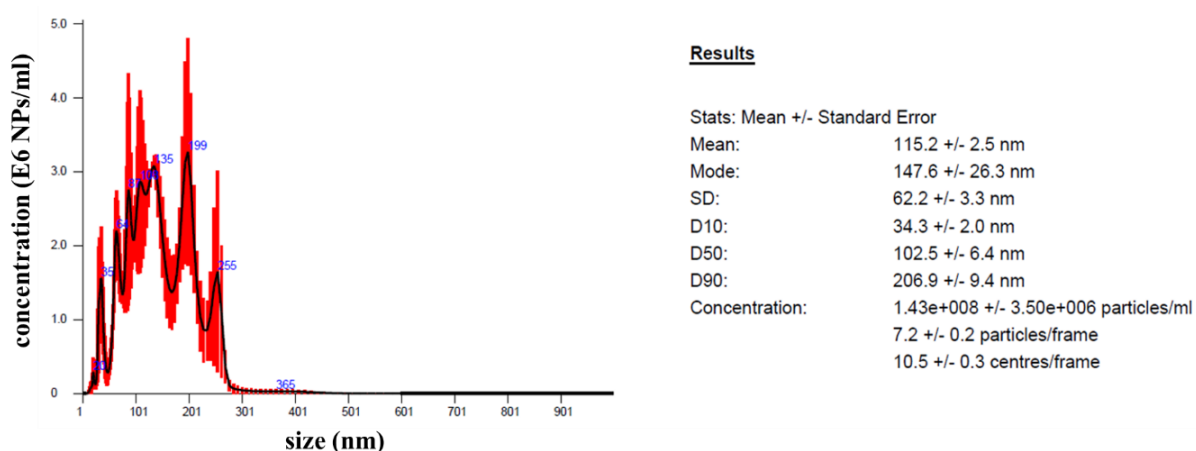
Figure 48. *NTA results for AuPt NPs.*

3.1.3. Introduction of a third element: ternary AuPdPt NPs

Figure 49a1 shows the HAADF STEM image of the synthesized AuPdPt NPs. The obtained NPs were spherical in shape, had a rough surface and a relatively small size distribution (Figure 49b). The EDS maps, shown in Figure 49a2-a5) confirmed, confirm that the spherical core ($\approx$ 19 nm) was made of gold. It is surrounded by a continuous layer of palladium having a thickness of $\approx$ 1.5 nm. The irregular outer layer was composed of $\approx$ 2 nm small, spherical platinum NPs, forming a continuous outer layer on the AuPd NPs.
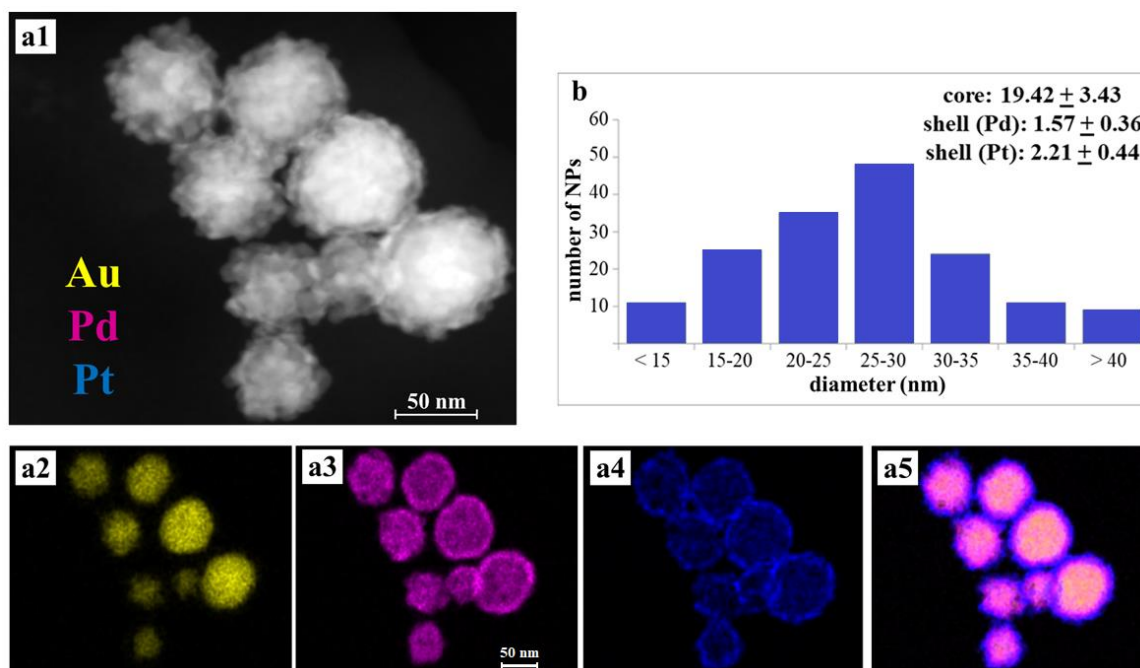
Figure 49. *a1) STEM image of AuPdPt NPs with the corresponding individual EDS distribution maps of a2) gold, a3) palladium, a4) platinum and a5) superposed Au, Pd and Pt.*
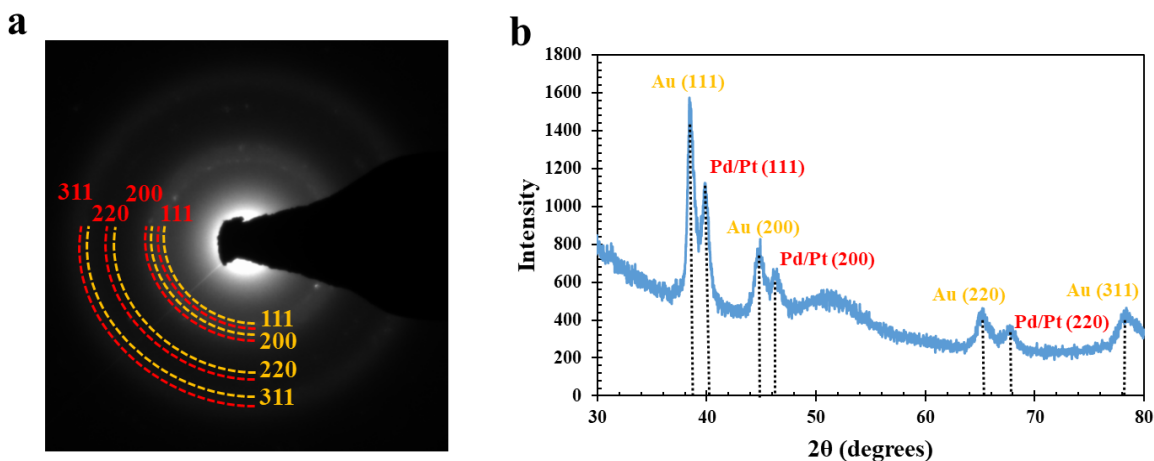
Figure 50. *a) SAED patterns of the AuPdPt NPs indexed with lattice parameters of gold, platinum and palladium. b) XRD diffractogram of AuPdPt NPs. Au peaks are marked in yellow, while Pd or Pt peaks in red.*

The SAED diffraction pattern, shown in Figure 50a consists of sharp diffraction rings indexed with the (111), (200), (220) and (311) lattice planes of fcc gold. Moreover, a second set of rings originating from platinum and palladium, attributed also to the (111), (200), (220) and (311) lattice planes. The rings from Pt and Pd overlap due to the small differences in the lattice parameters $a_{Pd} = 0.389$ nm and $a_{Pt} = 0.392$ nm. The X-ray diffractogram (Figure 50b) displays seven different diffraction peaks. The peaks appearing at 38.40°, 44.88°, 65.29° and 78.63° originate from fcc gold peaks according to standard values (ICDD, 00-004-0784) and correspond to (111), (200), (220) and (311) planes. The peaks observed at 39.82°, 46.29° and 67.89° are very close to standard values for both platinum and palladium, therefore it is impossible to attribute the peaks to the respective metals (ICDD, 00-004-0802 and 00-005-0681). Thus, it is assumed that the peaks correspond to (111), (200) and (220) planes for fcc Pd and fcc Pd. The calculated average size of the NPs is 22.1 nm. This is in good agreement with the TEM characterization showing an average size of 24 nm.

In the UV-Vis spectrum (Figure 51) of the AuPdPt NPs no peaks were observed, which means that Pt NPs and Pd NPs covered the entire Au NPs surface.

The determined value of the zeta potential for AuPdPt NPs is – 24.12 mV. As for the other tested NPs, NTA also showed that AuPdPt NPs have a much larger diameter than in reality, which was evaluated by the TEM and XRD methods.
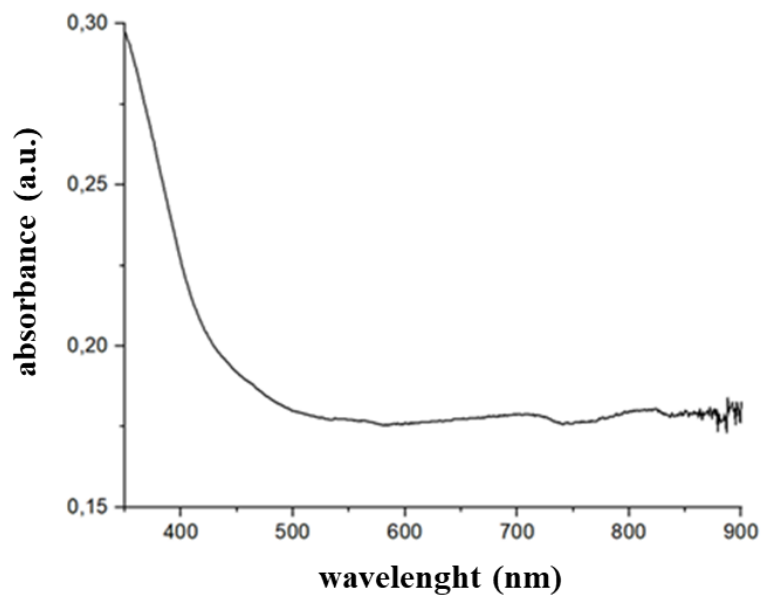
Figure 51. *UV-Vis spectrum of AuPdPt NPs.*

Results

Stats: Mean +/- Standard Error
Mean:	120.1 +/- 4.9 nm
Mode:	167.2 +/- 20.0 nm
SD:	79.9 +/- 1.3 nm
D10:	24.4 +/- 3.9 nm
D50:	109.2 +/- 4.3 nm
D90:	221.2 +/- 3.2 nm
Concentration:	2.58e+008 +/- 1.35e+007 particles/ml
	13.1 +/- 0.7 particles/frame
	34.4 +/- 1.3 centres/frame
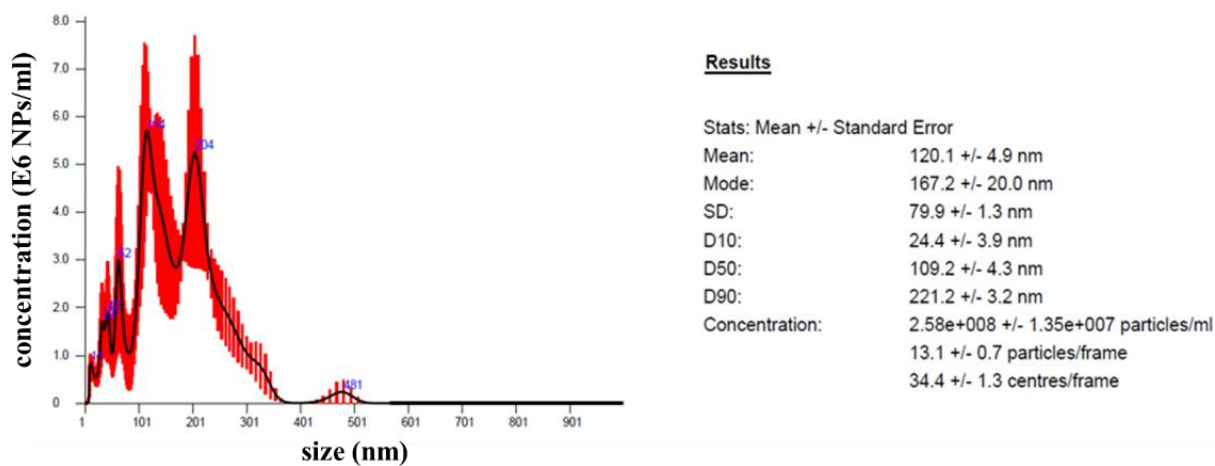
Figure *52. NTA results for AuPdPt NPs.*

3.2. Interaction of proton beam with NPs – ChPAA results

ChPAA allowed to assess whether the nuclear reaction occurs through the interaction of high-energy protons with the NPs solution, so it is possible to observe the emitted prompt or decay gamma radiation characteristic for individual nuclei. Figure 53 shows gamma-ray spectra of a control and an activated sample of synthesized NPs.
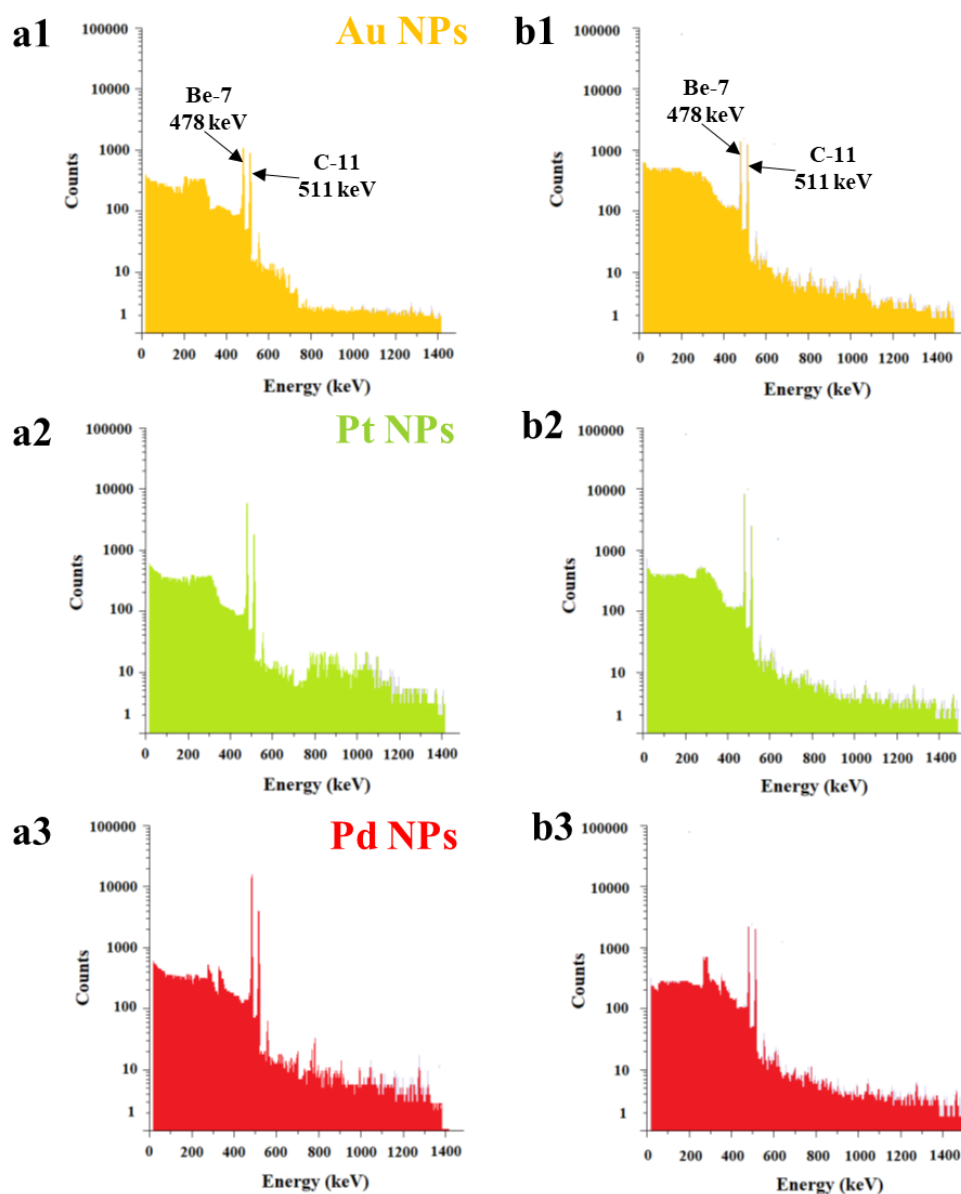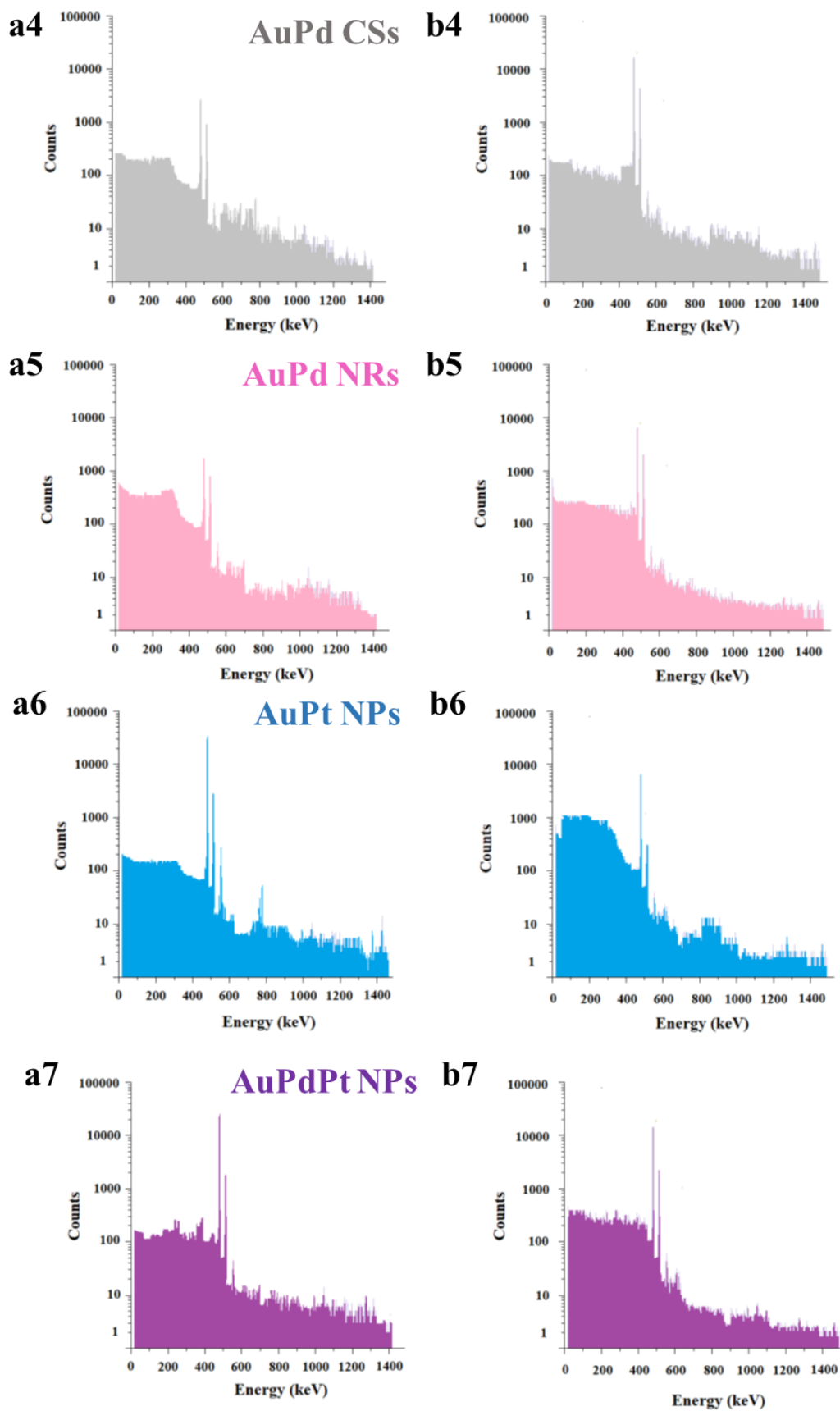
Figure 53. *Gamma-ray spectrum of a1-a7) control and b1-b7) activated samples of the Au NPs, Pt NPs, Pd NPs, AuPd CSs, AuPd NRs, AuPt NPs and AuPdPt NPs, respectively.*

It was confirmed that the proton beam used was not sufficient to induce a nuclear reaction in Au, Pt or Pd, which would emit gamma rays, characteristic for these elements or other nuclides/isotopes, formed as a result of the nuclear reaction. It is possible to see the line (478 keV) for Be-7 produced *via* oxygen spallation ^{16}O (p, spall)[7] characterized by half-life $T_{1/2} = 53.12$ days. Moreover, the characteristic line (511 keV) for short-lived isotope C-11 created as a result of oxygen spallation can be observed [163].

3.3. Nanoparticle-assisted proton irradiation *in vitro*

3.3.1. MTS viability assay

The MTS assay was performed for two reasons: i) determination of the maximum concentration of the respective NPs type, which is non-toxic for the cells used; ii) evaluation of the changes in viability of colon cancer and normal epithelium cells caused by NPs-PIr. The description of all the samples analyzed in biological *in vitro* studies is shown in Table 1.

Table 1. *Description of the investigated samples. Where C = SW480, SW620, HCT116 or CRL-1790; NPs = Au NPs, Pt NPs, Pd NPs, AuPt NPs, AuPd CSs, AuPd NRs or AuPdPt NPs.*

Sample	Sample acronym
Cells without addition of NPs and PIr (control)	Ctrl
Cells cultured with NPs	C@NPs
Cells irradiated by the proton beam (PR$^+$)	C@PR$^+$
Cells cultured with NPs and irradiated by the proton beam	C@NPs@PR$^+$

a) Maximum non-toxic NPs concentration

The results are presented only for Pd NPs, because they were most promising at the preliminary stage. The respective graphs for all other investigated NPs are shown in the „Supplementary information" (Figure 65-70). Figure 54 presents data of the cell viability in relation to the Pd NPs concentration and incubation time. These data indicate that for all cell lines analyzed, there was a tendency for decreased cell viability with an increase of the concentration of Pd NPs, although at low concentrations of Pd NPs, no statistically significant cytotoxic effect was observed. In addition, for all tested concentrations of Pd NPs, the decrease in cell viability was less pronounced after a short, 3 h incubation time, comparing to 18 h or 24 h. Moreover, an extension of the incubation time from 18 h to 24 h did not significantly change the cytotoxic effect of NPs on cancer and normal cells.
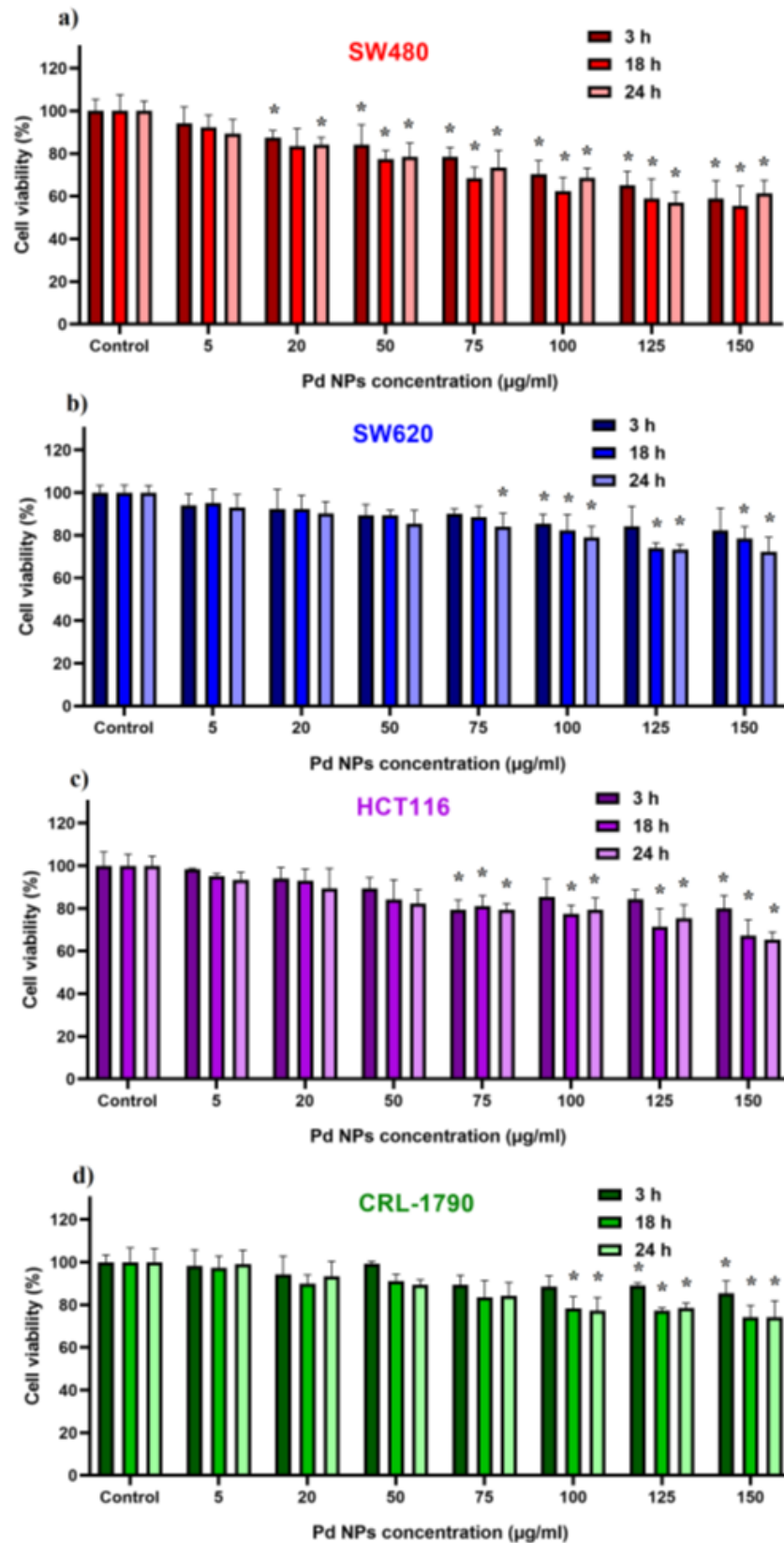
Figure 54. *Cytotoxicity of Pd NPs against a) SW480 (red bars), b) SW620 (blue bars), c) HCT116 (violet bars) and d) CRL-1790 (green bars) cells after 3, 18 and 24 h of incubation. Data were considered significant when *p-value < 0.05 vs control.*

Based on these data, the non-toxic concentrations of the Pd NPs, defined as the concentration not causing decrease in cell viability by more than 15 %, were established as follows: 20 μg/ml for SW480 cells, 50 μg/ml for SW620 and HCT116 cells, and 75 μg/ml for CRL-1790 cells. Determination of the non-toxic concentration of NPs was performed in the same way for all synthesized NPs and for all time points. Below (Table 2) the non-toxic concentrations of NPs established for 18 h incubation with the cells, have been presented. The 18 h incubation time was further selected for the evaluation of the effectiveness of the NPs-PIr.

Table 2. *Non-toxic concentration of all NPs types after 18 h incubation with four studied cell lines.*

	SW480	SW620	HCT116	CRL-1790
Au NPs	50	125	125	125
Pt NPs	50	100	100	100
Pd NPs	20	50	50	75
AuPt NPs	50	75	100	100
AuPd CSs	75	100	100	150
AuPd NRs	75	100	100	150
AuPdPt NPs	20	50	50	75

The data presented in Table 2 show, that the established non-toxic concentrations of the NPs types depend on their composition and the targeted cells. Concerning the composition of the NPs, the least toxic effect was observed for two bimetallic AuPd NPs. In respect to the target cells, the highest cytotoxicity of all types of NPs used was observed for SW480 cancer cells. These cells are least aggressive, least metastatic and least sensitive to the experimental treatment [164], [165]. Furthermore, all used cancer cell lines were more sensitive to the treatment with NPs, comparing to normal ones.

b) NPs-PIr

The effectiveness of the noble metal NPs-PIr was investigated. The results are presented, as previously, only for Pd NPs (Figure 55). The obtained graphs for other NPs investigated are shown in the „Supplementary information" (Figure 71-76). From these data it can be concluded that PIr alone, did not significantly affect the viability of cancer nor normal cells. However, after irradiation of the cells cultured in the presence of NPs, a significant decrease of only cancer cell viability was noticed.
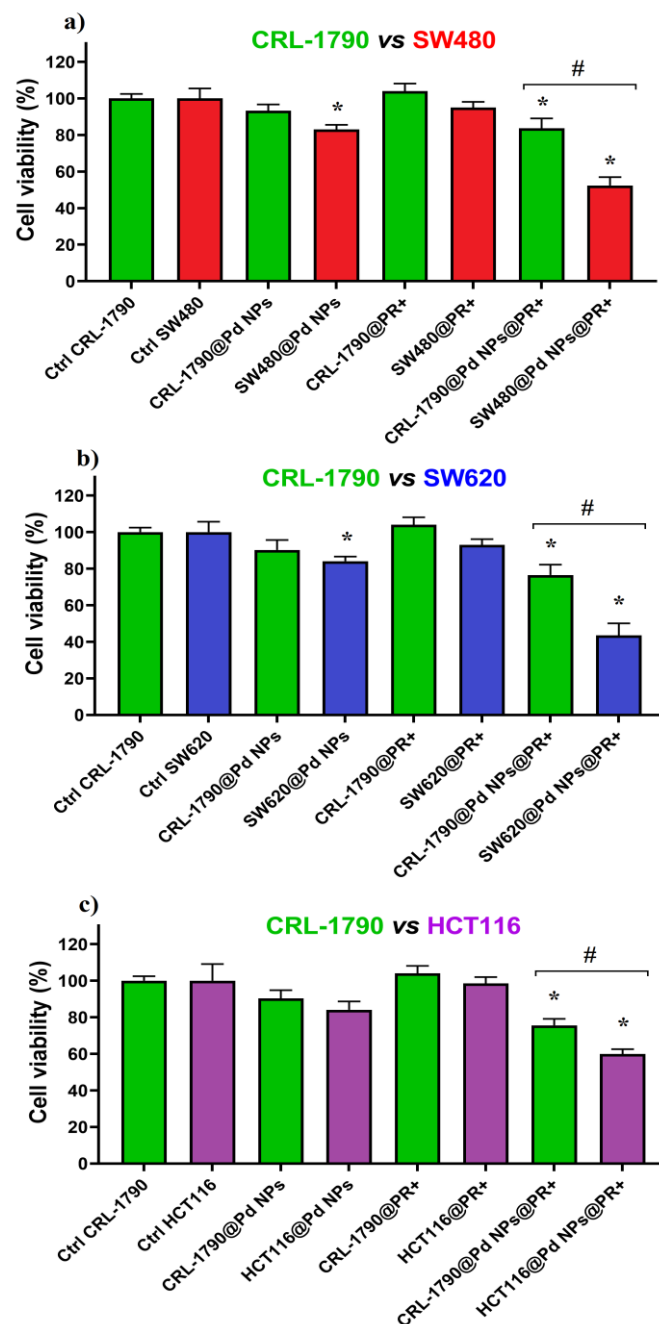
Figure 55. *The MTS assay assessed viability of a) SW480 (red bars), b) SW620 (blue bars) and c) HCT116 (violet bars) cancer cells compared to the viability of CRL-1790 normal colon epithelium cells (green bars) after their incubation with Pd NPs and PIr (total dose of 15 Gy). The MTS test was performed after 18 h of cell irradiation, which was preceded by 3 h culture of cells with a non-toxic NPs concentration. Data were considered significant, if *p-value < 0.05 vs control and #p-value < 0.05 – statistically significant differences between the respective cancer and normal cells.*

Tables 3-5 summarize the results of cell viability determined by the MTS assay for all tested cell lines subjected to NPs-PIr. This type of treatment showed a toxic effect on colon cancer cells, while the overall viability of normal colon epithelium cells was not significantly decreased. As shown in Table 2, the SW620 and HCT116 cells were most often treated with the same concentration of NPs (except for AuPt NPs), so it was possible to statistically compare the NPs-PIr against these two lines. PIr had a stronger effect on the

SW620 cells in the presence of the tested NPs because the SW620 line is characterized by higher radiosensitivity than the HCT116 cells. After PIr, the viability of the cells cultured with Pt NPs decreased to 52 %, 54 % and 56 % for SW480, SW620 and HCT116 cells, respectively, while for the Pd NPs the cell viability was 53 %, 44 %, 60 %, for SW480, SW620 and HCT116 cells, respectively.

Table 3. *MTS viability assay results for NPs-PIr. Comparison of the survival of normal CRL-1790 (green) and cancer SW480 (red) cell lines.*

	C@NPs	C@PR⁺	C@NPs@PR⁺
Au NPs	95/85	104/95	91/71
Pt NPs	93/88	104/95	79/52
Pd NPs	93/83	104/95	84/53
AuPt NPs	91/83	104/95	89/70
AuPd CSs	98/91	104/95	97/82
AuPd NRs	96/89	104/95	94/60
AuPdPt NPs	96/84	104/95	94/64

Table 4. *MTS viability test results for NPs-PIr. Comparison of the survival of normal CRL-1790 (green) and cancer SW620 (blue) cell lines.*

	C@NPs	C@PR⁺	C@NPs@PR⁺
Au NPs	86/83	104/93	85/64
Pt NPs	81/85	104/93	76/54
Pd NPs	90/84	104/93	77/44
AuPt NPs	87/83	104/93	83/61
AuPd CSs	93/87	104/93	95/76
AuPd NRs	93/87	104/93	92/58
AuPdPt NPs	92/84	104/93	92/64

Table 5. *MTS viability test results for NPs-PIr. Comparison of the survival of normal CRL-1790 (green) and cancer HCT116 (violet) cell lines.*

	C@NPs	C@PR⁺	C@NPs@PR⁺
Au NPs	86/88	104/99	85/76
Pt NPs	81/89	104/99	76/56
Pd NPs	90/84	104/99	75/60
AuPt NPs	82/86	104/99	90/72
AuPd CSs	93/87	104/99	92/84
AuPd NRs	93/83	104/99	83/72
AuPdPt NPs	92/84	104/99	87/68

From the data presented in Table 3-5, it can be concluded that – despite the similar cytotoxicity level of the AuPd NRs and AuPdNPs – there is a significant difference in their radiosensitizing properties in combined NPs-PIr. AuPd NRs with a highly porous surface

of palladium shell decreased viability of the SW480, SW620 and HCT116 cells after PIr to 60 %, 58 % and 72 %, respectively. The treatment with AuPd CSs having a continuous, non-porous shell, resulted in a less pronounced decrease in cell viability after irradiation: 82 %, 78 %, 84 % for SW480, SW620 and HCT116 cells, respectively.

3.3.2. Evaluation of cells death by Annexin-V binding and flow cytometry analysis

Figure 56 shows the results from the Annexin-V binding assay obtained for all four cell lines treated with the non-toxic concentration of Pd NPs and/or irradiated with protons. For these experiments the Pd NPs were chosen, as the ones giving the most pronounced radiosensitizing effect. Dot-plots show live (annexin-V-negative) and apoptotic (annexin-V-positive) cells. Graphical presentations of the corresponding data for other types of NPs have been included in the „Supplementary information" (Figure 77-82).
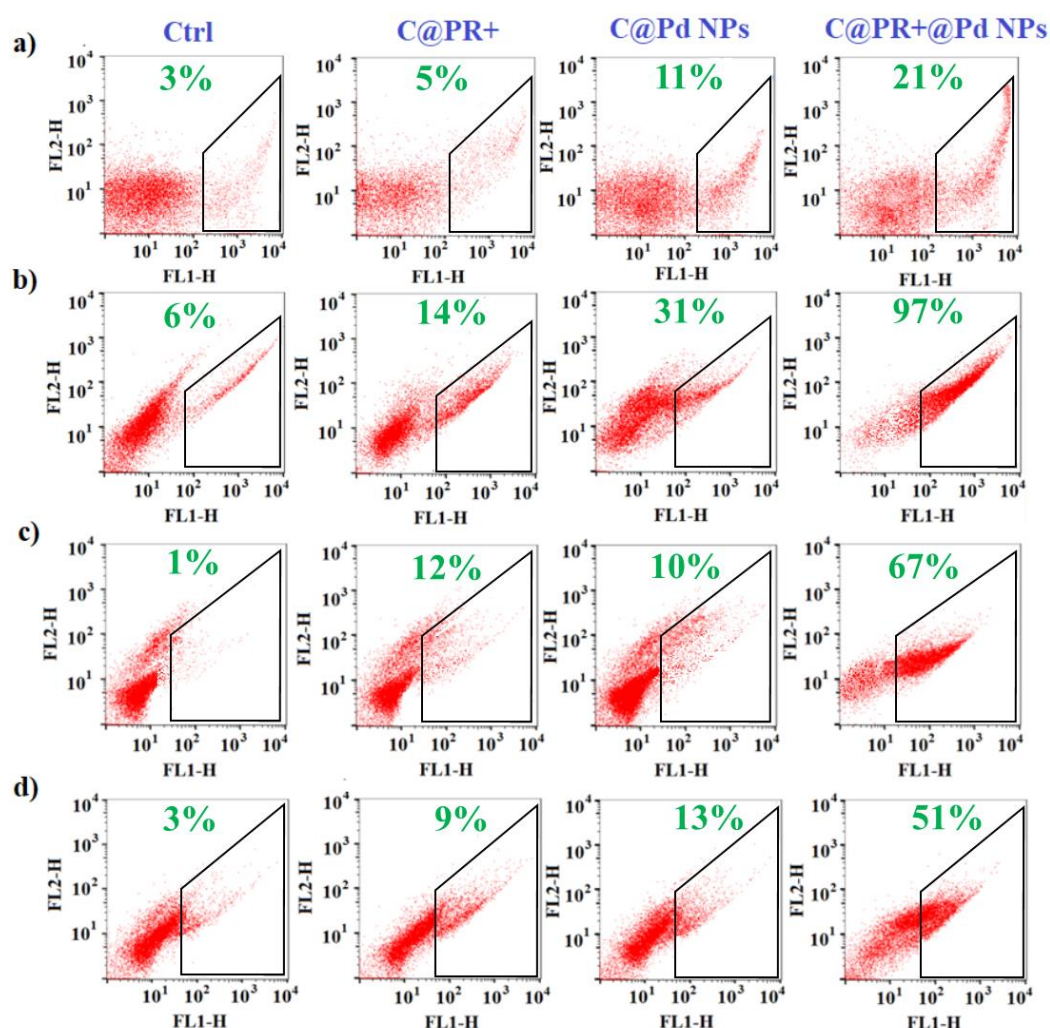
Figure 56. *Flow cytometry dot plots of the FL1-H (green fluorescence) vs FL2-H (red fluorescence) of a) CRL-1790, b) SW480, c) SW620 and d) HCT116 cells after addition of Pd NPs, followed by PIr. The percentages of apoptotic cells are marked in green.*

Table 6-8 summarize the results of cell apoptosis obtained by flow cytometry analysis. Normal CRL-1790 cells turned out to be less sensitive to this type of treatment, comparing to colon cancer cells. In some cases, no changes in viability of these cells after NPs-PIr was noticed. These data confirmed the previous results obtained by MTS tests. Similarly, it was also confirmed that the highest percentage of apoptotic cancer cells was detected, when ultra-small Pt NPs (91 %, 55 % and 48 % for SW480, SW620 and HCT116 cells, respectively) and Pd NPs (96 %, 67 % and 51 % for SW480, SW620 and HCT116 cells, respectively) were used for the cell treatment. Comparing AuPd CSs and AuPd NRs, there was also a difference in their radiosensitizing potential in favor of AuPd NRs. In turn, Au NPs, AuPt NPs and AuPdPt NPs showed similar radiosensitizing properties – only for SW480 cells the Au NPs showed a weaker effect than the other two NPs. Exemplary flow cytometry analysis of cells stained with propidium iodide (PI) was also performed (Figure 57), however the percentage of necrotic cells identified was negligible. Thus, it was concluded that the primary mechanism of cell death after the NPs-PIr treatment is apoptosis.

Table 6. *Annexin-V binding test results for NPs-PIr. The table shows the percentages of apoptotic CRL-1790 (green) and cancer SW480 (red) cells after the respective mode of treatment.*

	Ctrl	C@NPs	C@ PR⁺	C@NPs@PR⁺
Au NPs	3/6	7/5	5/14	9/37
Pt NPs	3/6	6/6	5/14	17/91
Pd NPs	3/6	11/31	5/14	21/97
AuPt NPs	3/6	6/17	5/14	11/72
AuPd CSs	3/6	4/5	5/14	5/24
AuPd NRs	3/6	4/19	5/14	6/82
AuPdPt NPs	3/6	5/28	5/14	12/82

Table 7. *Annexin-V binding test results for NPs-PIr. The table shows the percentage of apoptotic CRL-1790 (green) and cancer SW620 (blue) cells after the respective mode of treatment.*

	Ctrl	C@NPs	C@ PR⁺	C@NPs@PR⁺
Au NPs	3/1	7/4	5/12	9/34
Pt NPs	3/1	6/5	5/12	17/55
Pd NPs	3/1	12/10	5/12	25/67
AuPt NPs	3/1	9/1	5/12	13/40
AuPd CSs	3/1	5/1	5/12	8/25
AuPd NRs	3/1	6/7	5/12	12/50
AuPdPt NPs	3/1	7/6	5/12	13/44

Table 8. *Annexin-V binding test results for NPs-PIr. The table shows the percentage of apoptotic CRL-1790 (green) and cancer HCT116 (violet) cells after the respective mode of treatment.*

	Ctrl	C@NPs	C@ PR$^+$	C@NPs@PR$^+$
Au NPs	3/3	12/7	5/9	14/42
Pt NPs	3/3	15/13	5/9	22/48
Pd NPs	3/3	14/13	5/9	33/51
AuPt NPs	3/3	11/3	5/9	15/45
AuPd CSs	3/3	6/4	5/9	11/37
AuPd NRs	3/3	6/11	5/9	17/48
AuPdPt NPs	3/3	8/8	5/9	17/43
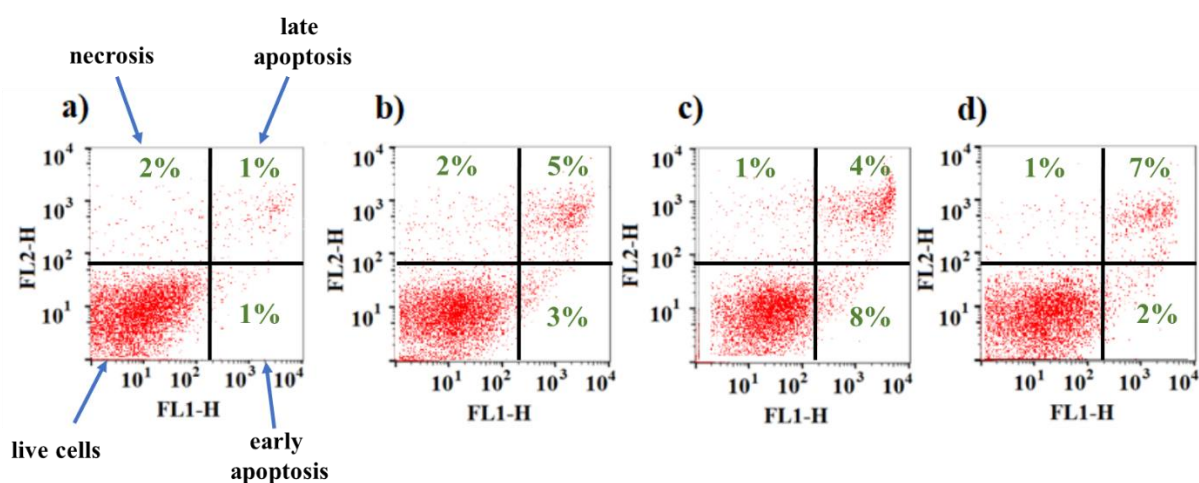
Figure 57. *Flow cytometry analysis of Annexin V binding and propidium iodide staining of CRL-1790 cells a) without and after the addition of b) Au NPs, c) Pd NPs and d) AuPd NRs, followed by PIr. Dot plots FL1-H (green fluorescence) vs FL2-H (red fluorescence) show the percent of live, early apoptotic, late apoptotic and necrotic cells.*

3.4. Interactions of NPs with cancer and normal cells determined by 3D holotomographic microscopy

To determine the interaction between the cells and the NPs, the holotomographic 3D microscopy technique was used. The reconstruction of the obtained holograms allowed to visualize in 3D, the accumulation of the NPs on the surface or inside the cells. This was investigated only for the non-toxic concentrations of NPs determined by MTS assay. Below, only images of cells cultured with or without Pd NPs are presented.

To determine whether the NPs penetrate the cell and to obtain information about the cellular location of NPs accumulation, the RI distribution was analyzed, as shown below.
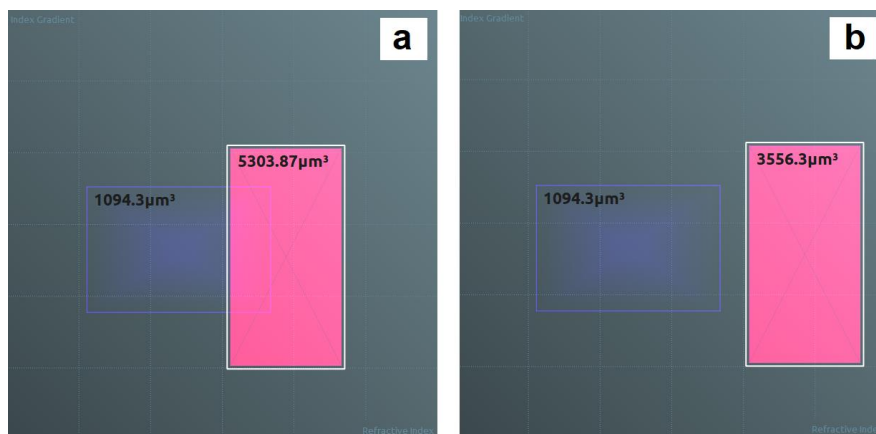
Figure 58. *Distribution of RI with the value of RI volume corresponding to individual structures: NPs (red color) and cell membrane (blue color).*

If the RI corresponding to NPs and cell membrane overlap, the NPs occupy the entire depth of the observed field, meaning they are located both inside and outside the cells (Figure 58a). Consequently, if the RI corresponding to the NPs and the cell membrane do not overlap, then the NPs are located on the cell surface - the cell membrane (Figure 58b).

In this paragraph, the first, preliminary results, obtained using the newly acquired Nanolive 3D holotomographic microspore have been presented. This microscope acquires a 3D tomogram of the live cells, and although the illumination source is a laser, this instrument reaches a nanometer resolution, because the image reconstruction is performed using the refractive indexes of the respective elements of the cells and of the NPs, respectively. Only a few possibilities of the Nanolive 3D are demonstrated below for four cell lines: CRL-1790 normal epithelium cells, SW480, SW620, HCT116 colon cancer cells during their interaction with Pd NPs. To evaluate, how deep the Pd NPs penetrate the cells during the incubation time, holotomographic slices, taken at approximately 13 μm (Z1), 17 μm (Z2) and 21.6 μm (Z3) in depth, corresponding respectively to cell surface, nucleus and bottom part of the cell, were analyzed. Moreover, to indicate the accumulation site of NPs, e.g. nucleus or cell membrane, the refractive index (RI) of the Pd NPs in red, nuclei in blue and cell membrane in green color were marked on the Z1-Z3 holotomographic images.

a) CRL-1790 normal epithelium cells

The morphology of normal epithelium cells cultured with Pd NPs was compared with the images of cells cultured without NPs (control) (Figure 59a). The analysis revealed that Pd NPs added to the culture of CRL-1790 normal epithelium cells, already after 1 h of incubation, caused the formation of stress fibers, which remained present during the entire observation period (Figure 59b). Moreover, after 18 h of culture, changes in the structure of cells' nuclei were noticed. The 3D reconstruction images showed, that the volume of NPs located inside the cells was increasing in time (Figure 59c). The analysis of the 3D reconstruction combined with Z-axis images suggests, that Pd NPs started to penetrate the cells already after 1 h (Figures 59c and d). The Z1-Z3 images document that after 1 h some of the Pd NPs were still outside the cells, while the others attached to the cell membrane and penetrated the cells around the nuclei. This was proven by the overlapping values of the RIs, corresponding to Pd NPs, nuclei and cell membrane, respectively. After 6 h, the NPs were

detected only inside the cells, while after 18 h of culture, Pd NPs were observed also on the cell membrane and outside the cells. The volume of Pd NPs reached a maximum value after 18 h of culture.
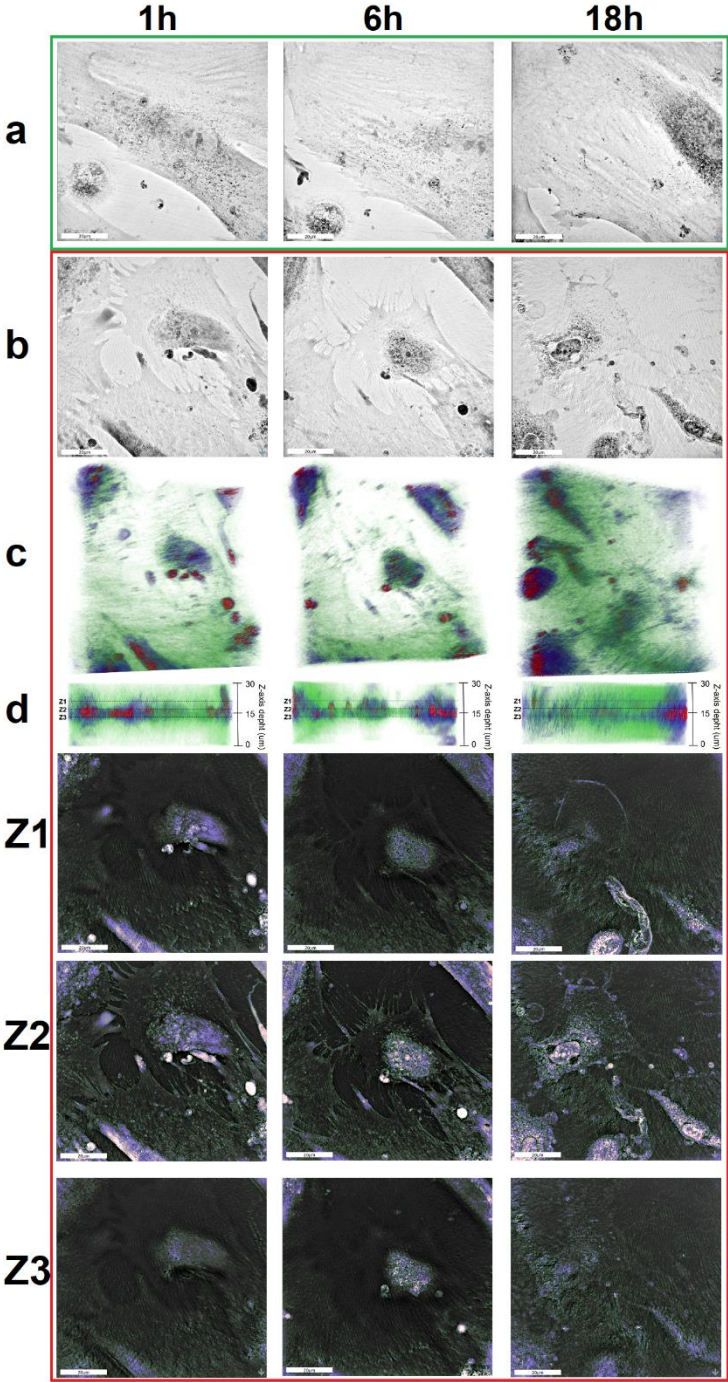
Figure 59. *Holotomographic images of the CRL-1790 normal epithelium cells cultured a) without and b) with Pd NPs taken after 1 h (left column), 6 h (middle column) and 18 h (right column). c) Reconstructed 3D holotomographic images based on the RI value of: Pd NPs (red color), nuclei (blue color) and cell membrane (green color). d) Z-axis reconstruction of holotomographic images with indicated thickness of slices approximately 13μm (Z1), 17μm (Z2) and 21.6 μm (Z3), while Z1, Z2 and Z3 panels show holotomographic images with marked RI of Pd NPs (red color), nuclei (blue color) and cell membrane (green color). Scale bar ≈ 20 μm.*

b) SW480 colon cancer cells

The Pd NPs added to the culture of SW480 colon cancer cells caused, after 6 h, alterations in the cell membranes, which look like „membrane budding" (Figure 60b). Similarly to cells cultured without Pd NPs, the cells in the presence of Pd NPs continued their division process, detected as an increasing number of cells in the observation area after 6 h and 18 h. Furthermore, Figure 60c combined with Figure 60d shows that, at first Pd NPs did not accumulate at any preferential site. Conversely, after 18 h of culture, the majority of Pd NPs accumulated in the central part of the cell – the nucleus. The Z1 images document, that Pd NPs were detected outside the cells after 1 h and 18 h of culture. The Z2 images show, that after 6 h and 18 h, the Pd NPs were located inside the cells, specifically around nuclei. However, after 18 h of culture in the Z3 projection the Pd NPs were located between the nucleus and the „bottom" of the cells (overlapping blue and red colors).
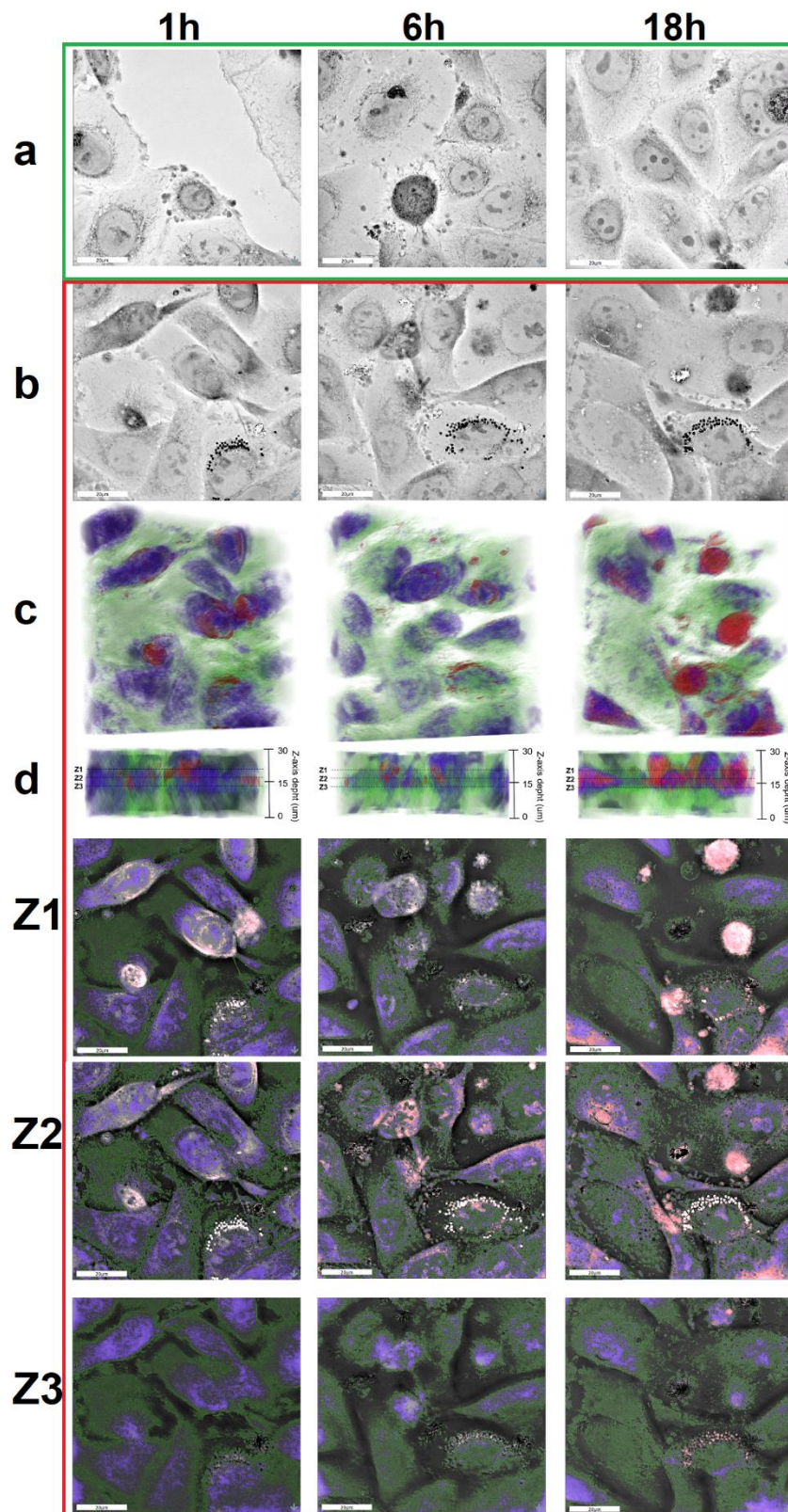
Figure 60. *Holotomographic images of SW480 colon cancer cells cultured a) without and b) with Pd NPs taken after 1 h (left column), 6 h (middle column) and 18 h (right column). c) Reconstructed 3D holotomographic images based on the RI value of: Pd NPs (red color), nuclei (blue color) and cell membrane (green color). d) Z-axis reconstruction of holotomographic images with indicated thickness of slices approximately 13µm (Z1), 17µm (Z2) and 21.6 µm (Z3), while Z1, Z2 and Z3 panels show holotomographic images with marked RI of Pd NPs (red color), nuclei (blue color) and cell membrane (green color). Scale bar ≈ 20 µm.*

c) SW620 colon cancer cells

From the beginning of the imaging „membrane budding" was observed both in control and Pd NPs-treated SW620 cells (Figure 61a and b), but it disappeared after 6 h. Moreover, Pd NPs caused detaching of some cells from the substrate (likely dead cells). After 18 h, apoptotic cells with condensed nuclei were noticed in the field of view (Figure 61b). The 3D reconstruction images showed, that during the first 6 h of culture, the Pd NPs did not accumulate preferentially in any location, but after 18 h, the majority of the Pd NPs were detected around cell nuclei (Figure 61c), which was confirmed by the Z-axis images (Figure 61d). The Z1-Z3 projections document that after 1 h, the Pd NPs are visible outside the cells, on the cell membrane and inside the cells around nuclei, while after 6 h of culture all NPs penetrated the cells. Moreover after 18 h, Pd NPs were located in the entire depth of the cells. The Z2 and Z3 images acquired after 18 h of culture showed, that the cells with the entire volume loaded with Pd NPs, became apoptotic.
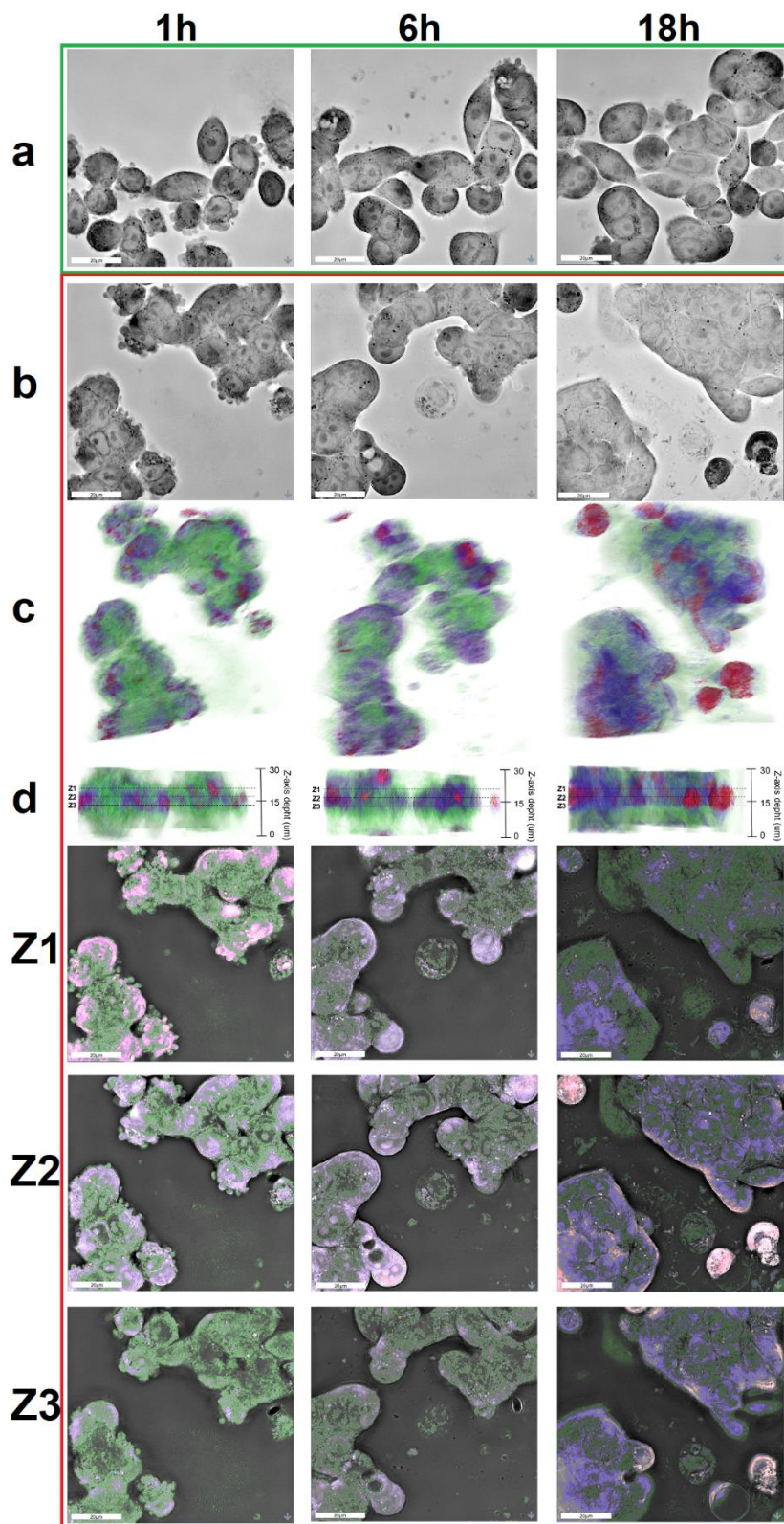
Figure 61. *Holotomographic images of SW620 colon cancer cells cultured a) without and b) with Pd NPs taken after 1 h (left column), 6 h (middle column) and 18 h (right column). c) Reconstructed 3D holotomographic images based on the RI value of: Pd NPs (red color), nuclei (blue color) and cell membrane (green color). d) Z-axis reconstruction of holotomographic images with indicated thickness of slices approximately 13μm (Z1), 17μm (Z2) and 21.6 μm (Z3), while Z1, Z2 and Z3 panels show holotomographic images with marked RI of Pd NPs (red color), nuclei (blue color) and cell membrane (green color). Scale bar ≈ 20 μm.*

d) HCT116 colon cancer cell line

The addition of Pd NPs to the culture of HCT116 cells did not cause significant alterations in their morphology in comparison to the cells cultured without Pd NPs (Figure 62a and 62b). Furthermore, the NPs were uniformly distributed over the entire cell surface (Figure 62c and 62d). Analysis of the Z1-Z3 images showed, that after 1 h the Pd NPs were located on the cell membrane (top of the cells) and inside the cells. Similar results were obtained after 6 h of culture, while after 18 h, the Pd NPs were accumulated in the whole cell depth (red color on the Z1-Z3 images overlapping with green and blue colors originating from the cell membrane and the nuclei).
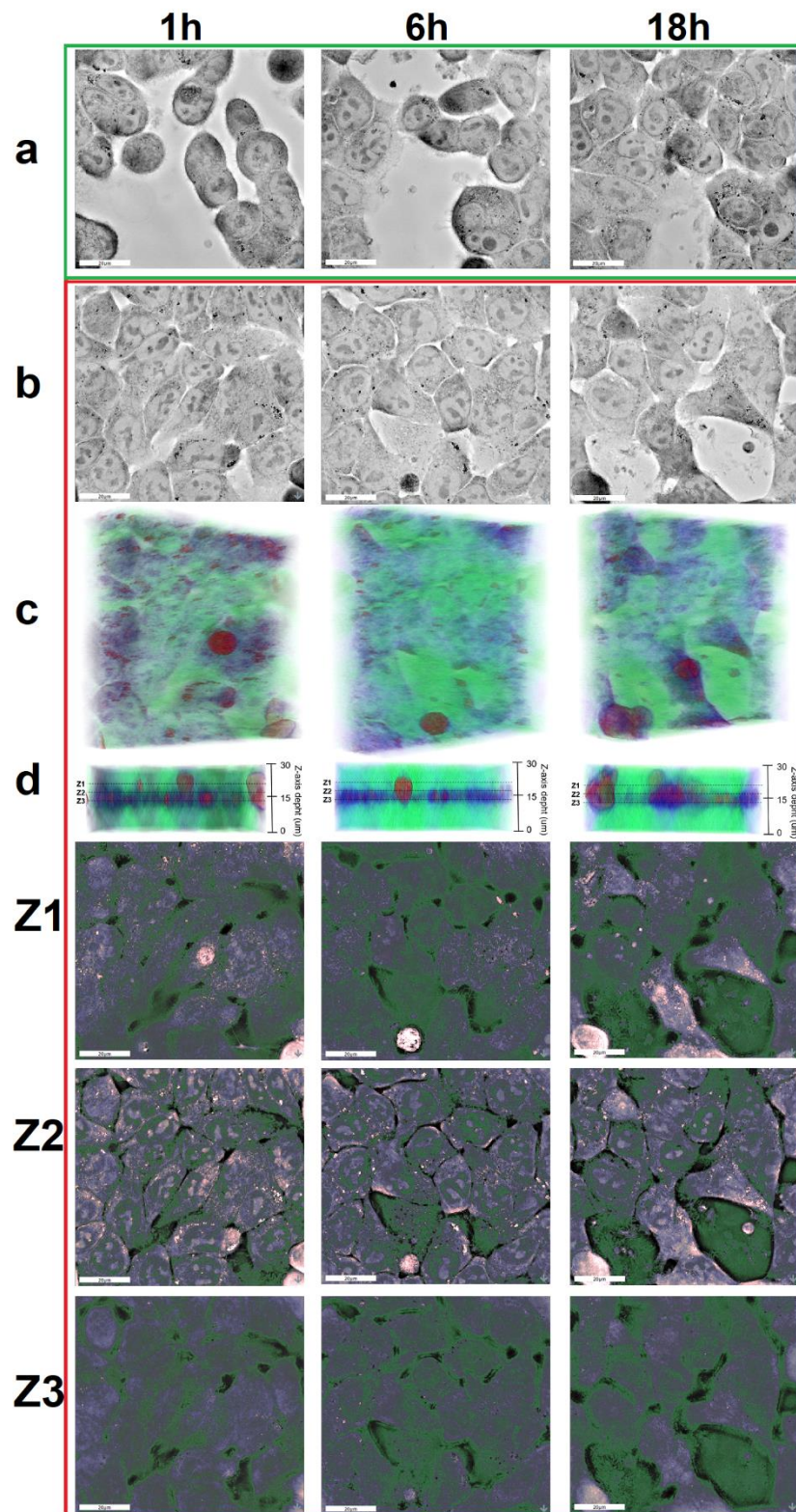
Figure 62. *Holotomographic images of HCT116 colon cancer cells cultured a) without and b) with Pd NPs taken after 1 h (left column), 6 h (middle column) and 18 h (right column). c) Reconstructed 3D holotomographic images based on the RI value of: Pd NPs (red color), nuclei (blue color) and cell membrane (green color). d) Z-axis reconstruction of holotomographic images with indicated thickness of slices approximately 13μm (Z1), 17μm (Z2) and 21.6 μm (Z3), while Z1, Z2 and Z3 panels show holotomographic images with marked RI of Pd NPs (red color), nuclei (blue color) and cell membrane (green color). Scale bar ≈ 20 μm.*

e) Volume of the Pd NPs accumulated in the cells in relation to the incubation time

To show the dynamics of Pd NPs accumulation within the cells, changes in the RI values originating from the Pd NPs after 1 h, 6 h and 18 h of incubation was calculated for each of the cell lines. As presented in Figure 63, for all cell lines used, the cellular volume occupied by NPs increased linearly with time of culture, albeit with different, cell specific, magnitude – being most pronounced for the SW620 cells. This means, that the absorption dynamics of the Pd NPs was different for the respective cell lines.
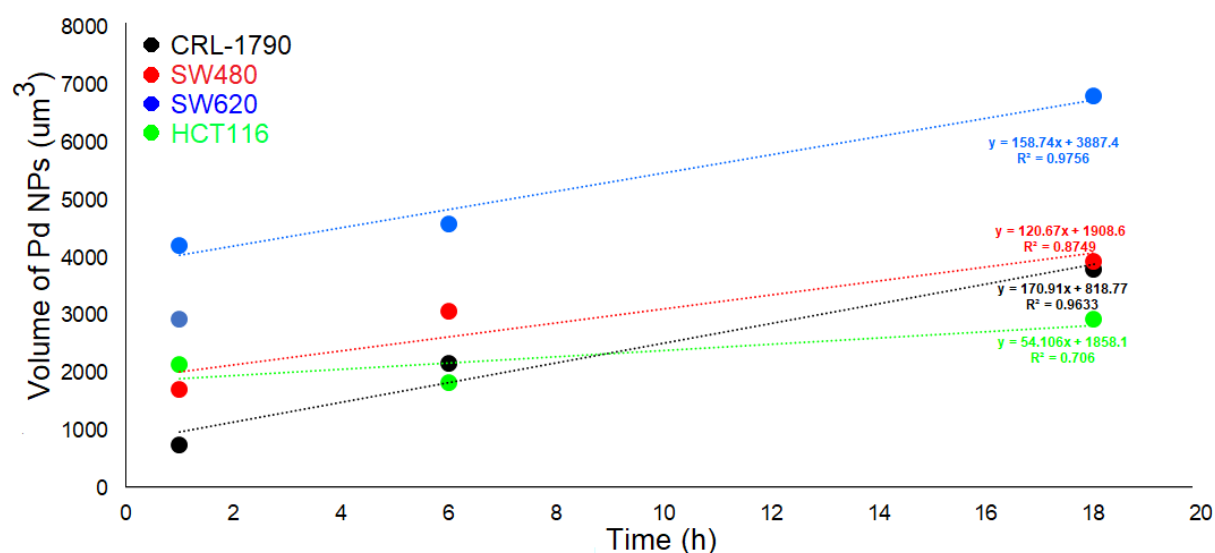
Figure 63. *Cell volume occupied by NPs as a function of the incubation time with a) CRL-1790, b) SW480, c) SW620 and d) HCT116 cells. The linear equations and the R^2 values are shown.*

Chapter 4: Discussion

Cancer is the second most common cause of death in Poland. The latest data from the National Cancer Registry show that every year almost 170 000 people are diagnosed with cancer. Among them, about 100 000 patients die and around a million live with the diagnosis [166]. Such a high mortality indicates that commonly available cancer treatment methods, such as surgery, chemo- or conventional radiotherapy, are ineffective, while modern forms of targeted immunotherapy are dedicated only to highly selected groups of patients. Therefore, it is important to search for new anticancer therapies that will increase the patient's chance for a full recovery, and additionally will not cause numerous negative side effects [167].

Ionizing radiation was used in the treatment of cancer as early as the beginning of the 20th century. the treatment at that time was limited to superficial neoplasms, easily accessible without the use of additional imaging methods – e.g. skin cancer [98]. Contemporary radiation techniques, such as proton therapy, are a natural consequence of technological development. As technology progressed over the past decades, more and more advanced methods of delivering radiation to cancer cells deep into the patient's body, were developed. The aim was to improve the precision of treatment both, by limiting the scope of exposure of normal tissues and by using and developed methods to verify the tumor location [168]. However, also these modern anticancer therapies can be enhanced by the use of radiosensitizers, which can be e.g. noble metal NPs [105]. Therefore, the aim of this PhD dissertation was to obtain spherical, mono-, bi-, and trimetallic NPs. Due to their nanometer size, and hence the high surface to volume ratio, they can be attractive candidates to be used in sensitizing the cancer cells to irradiation with the proton beam. In the present study, NPs were added to the cancer and normal cell line cultures, which were subsequently irradiated by the proton beam to investigate the cell death.

NPs may exhibit different properties. Therefore, it is important, when planning their synthesis protocol, to know what application they will be applied for. NPs used in medicine and diagnostics should be characterized by low toxicity, biocompatibility, the possibility of surface functionalization and a small size, so that they can reach specific organs [169]. Moreover, for proton therapy, according to the Bethe-Bloch formula, NPs should be composed of a metal with a high-Z value [170]. Consequently, the present study is focused on NPs synthesized from gold, palladium, and platinum precursors. In biological applications of NPs, the structure of these materials is also important. The correlation between the crystal structure and toxicity of NPs was observed especially in respect to the human bronchial epithelium cell lines, which were treated by the same NPs differing only in their crystalline structure. It was shown, that rutile-like crystal structure was responsible for oxidative damage of DNA, lipid peroxidation, formation of micronuclei, which indicates abnormal chromosome segregation during mitosis, while NPs with anatase-like crystal structure were non-toxic for cancer cells [171]. Also, amorphous structured NPs are non-toxic for cancer cells [172]. Therefore, in order to obtain the joined effect of cells killing by NPs-PIr, NPs were synthesized as crystalline mono-, bi- and ternary NPs. Furthermore, the size of the NPs plays a very important role in their anticancer properties. The small size of NPs, below 50 nm, allows them to penetrate through epithelial and endothelial barriers into almost all organs, causing apoptosis

of the cells [173], [174]. While larger NPs lead to perforation of the cell membranes and the resultant entry of the NPs into the cells causing cell necrosis, as evidenced by the release of lactate dehydrogenase [175]. The obtained results from flow cytometry (Table 6-8) showed that in all cases, the NPs used caused apoptosis of the cells. Furthermore (Figure 30, Figure 34, Figure 37, Figure 40, Figure 45 and Figure 49) showed, that the size of all NPs types synthesized in the frame of this study was below 50 nm. Importantly, the NPs were added into the cells, which was also the reason why a small size of NPs was used. Modeling experiments show that small NPs may enter not only organs, tissues, and cells, but also cell organelles e.g., mitochondria and nuclei – this may drastically alter cell metabolism and cause DNA lesions, mutations and finally cell death [176]. Moreover, the synthesis method and the substrates used for reactions, as well as the chemical compositions of the NPs, determine the value of zeta potential of NPs, which directly affects the type of their interaction with the cells and their accumulation inside. The positive or negative values of zeta potential obtained for the synthesized NPs corroborate with the available literature data. The negative potential of the Au NPs obtained by Turkevich method results from the stabilization of nano-gold with negatively charged sodium citrate [177]. A similar result was obtained for monometallic Pt NPs, where polyethylene glycol also gives a negative value of this potential [45]. Conversely, for monometallic ultra-small Pd NPs, the sign of zeta potential is positive, due to the presence of positively charged stabilizing agents (CTAB) on the Pd NPs surface [178]. Both NPs obtained with gallic acid as reducing agents and stabilizers (AuPt NPs and AuPdPt NPs) show negative values of zeta potential, because gallic acid and its oxidation products are negatively charged [43], [179]. Interesting are the differences in zeta potential of both types of bimetallic AuPd NPs obtained by the reduction of palladium on pre-synthesized Au NPs. As shown earlier, Au NPs possess a negative zeta potential value. The nano-palladium reduced on the surface of Au NPs has also a negative zeta potential – ascorbic acid and its oxidation products are characterized by a negative value of zeta potential. A clear situation is for AuPd CSs, where palladium continuously covers the gold core and the surrounding solution is in contact only with palladium. This explains the clearly negative value of zeta potential of these non-porous NPs. On the other hand, for AuPd NRs with a porous shell structure, a positive charge of zeta potential was noticed. The solution surrounding the NPs is in contact with both, gold and palladium (both negatively charged), which may disturb the distribution of ions in the electrical double layer, resulting in a positive zeta potential value of AuPd NRs. The effect of the NPs location on the cell viability was also reflected in the MTS results (Table 3), where smaller a concentration of Pd NPs penetrating the cells caused a similar decrease in cell viability, like for Au NPs.

It was also shown that the stabilizing agents used to synthesize NPs, as well as the chemical composition of the NPs, determine the NPs cytotoxicity on cells. Table 3 showed, that the least toxic effect was observed for both bimetallic AuPd NPs. This is probably due to the fact that the ascorbic acid – vitamin C used as a stabilizer in the synthesis of these NPs stimulates cell growth and protects the cells from oxidative stress [180], [181]. Conversely, the ternary AuPdPt NPs are highly cytotoxic, because gallic acid , which is known for its anticancer properties, is used as a stabilizer [134]. Interestingly, AuPt NPs were also obtained using gallic acid, but a higher concentration of the AuPt NPs was needed to obtain

the same cytotoxic effect as for the AuPdPt NPs. This might be due to a joined effect of Pt and Pd against cancer cells. The role of the stabilizer in the toxicity of the NPs was also observed in the case of Pd NPs, synthesized using CTAB, which interacts with phospholipid bilayer, destabilizing the cell membrane composition [182]. Moreover, the toxic effect of the NPs depends also on the charge of zeta potential and the size of the NPs. NPs with a positive value of zeta potential exhibit bigger cytotoxicity than negatively charged ones [183], [184]. Indeed, positively charged NPs interact with the cell membrane through negatively charged phospholipids or membrane proteins, resulting in increased cellular uptake. Obviously, the charge of zeta potential is not the only determinant of cellular uptake. Small NPs may also be better internalized by cells than larger particles, since they require less energy and involvement of fewer receptors, supporting their internalization [185]. Consequently, non-toxic concentrations of the ultra-small Pt NPs and Pd NPs were the lowest in comparison with other obtained NPs. Finally, also the type of cells played a role in the toxicity of NPs. The highest cytotoxicity of all types of NPs used, was observed against SW480 cancer cells (Figure 54). These cells are least aggressive, least metastatic and most sensitive to the experimental treatment [164], [165], comparing to others used. Furthermore, all types of cancer cells used were more sensitive to the culture with NPs comparing to non-cancer cells.

Summarizing, small, crystalline, composed of high-Z metal atoms NPs, were obtained and investigated as radiosensitizers against three colon cancer cell lines, differed differing by aggressiveness and metastatic levels. High energy PIr was selected for the experiments, because for tumors located inside the body (such as colon tumor), it is necessary that the radiation will reaches the desired depth. In turn, the total dose of 15 Gy was considered non-toxic and was estimated from previous experiments conducted on the potential application of noble metal NPs to enhance X-ray radiotherapy (details can be found in the „Supplementary information", Table 9-11). Taking into account that the RBE for protons is equal 1.1, it can be assumed that a similar biological effect will be observed in the case of NPs-supported PIr. However, it must be remembered that much lower total radiation doses are used in the radiation therapy of colon cancer (≈ 2 Gy), but cells in cultures often show a different sensitivity to this type of treatment than tumors in the human body [186].

Although, a trend in the radiosensitizing effect of each type of NPs, determined by both MTS and flow cytometry methods, was generally similar, a higher antitumor effect was observed by cytometric analysis. Research studies show that cells treated with protons (both low and high energy), are more likely to die through apoptosis rather than necrosis [187]–[190]. Nevertheless, some analyzes using PI to assess the number of necrotic cells were also performed. The results of flow cytometry analysis generally correlate with those obtained from by the MTS test, however, it should be remembered that flow cytometry analysis of Annexin V stained cells allows for direct detection of early apoptotic cells, while in the MTS test, the percentage of viable cells is assessed indirectly, in relation to control cells, where cell viability is assumed as 100 %. Thus, it is not known, what percentage of cells in the control is damaged. These allowed to assume that the ultra-small NPs are indeed characterized by the best radiosensitizing properties, especially since both biological tests provides different information about the condition of cells: MTS – information about the cell metabolism – activity of mitochondrial enzymes, and flow cytometry – information on cell apoptosis.

Therefore, MTS as well as flow cytometry tests were used to show anticancer effects of the application of noble metal NPs and the proton beam (Table 3-8). The strongest cytotoxic effect of such a treatment (for MTS test) was observed for the SW620 cells. This is most likely due to the fact, that the metastatic SW620 line is cells are characterized by faster growth, comparing to other tested, while PIr is directed mainly against cells, which divide more intensively proliferating, causing their death. Furthermore, concerning the relationship between the radiosensitizing effect and the composition of the NPs used, it turns out that it is possible to replace the Au NPs, used as radiosensitizers in PT so far, by other metals giving even stronger radio-enhancing effect. Among the tested NPs, the ultra-small Pt and Pd NPs showed the best radiosensitizing properties. Especially the ultra-small Pd NPs seem promising, because in their case, the radiosensitizing effect was observed at the lowest (compared to other NPs tested) concentration. Interestingly, the literature data confirm that Pt NPs can act as both radiosensitizers and radioprotectors [191]. The small size of these NPs is a key parameter determining their radiosensitizing potential. This is due to the fact, that smaller NPs – having greater a bigger surface to volume ratio – deposit larger doses amount in the vicinity of cells. Thus, these smaller NPs, under the influence of PIr can generate an increased amount of ROS or free electrons, confirming that they are more effective radiosensitizers in radiation-based anticancer therapies than larger NPs. This result corresponds well with to other *in vitro* studies [8], [17], as well as Monte Carlo simulations [192]. Furthermore, the leakage of free ions of metals contained in the small NPs cores can occur. These may be absorbed by mitochondria and upon oxidation by environmental agents may cause morphological changes and dysfunction of the organelles [193]. All of them can enhance the irradiation effect of the proton beam on the cells cultured with the ultra-small NPs. Interestingly, the porosity of the shell in the case of bimetallic AuPd NPs had a substantial impact on their radiosensitizing properties. Porous AuPd NRs and non-porous AuPd CSs are of similar size and were synthesized by the same method with the use of the same reagents. Therefore, these NPs are suitable for comparing their radiosensitizing properties because they differ only by porosity. In this context, the intensified effect of the AuPd NRs could be caused by result from the increased contact of these NPs with the cells, provided by the more developed surface, in comparison to AuPd CSs. Due to the porous shell, the cells are in contact with both gold and palladium, which may differ in the radiosensitizing mechanism of these metals may be different. The positive charge of zeta potential may also determine the superiority of AuPd NRs over AuPd CS. A similar trend was observed for the same cells treated with NPs and irradiated with X-ray with a total dose of 15 Gy („Supplementary information", Table 9-11).

Finally, the radiosensitizing effect of each type of NPs can be explained by physical or biological – chemical mechanisms. The physical mechanism is related to interactions between the NPs and the proton beam. The proton energy used in our experiments was as high as 225 MeV. In the case of these high-energy protons, the probability that a nuclear reaction between protons and metals will occur (so-called nuclear cross-section) is relatively low. This is because the total non-elastic cross-section for proton-induced reaction increases up to about 20 MeV and then decreases asymptotically. It has been shown that for low-energy protons, nuclear reaction on ^{197}Au can be induced, leading to e.g. isotopes of gold (^{196}Au, ^{194}Au or ^{191}Au), as well as mercury (^{197}Hg, ^{195}Hg), iridium (^{192}Ir) or platinum (^{191}Pt) [194]. Similarly,

high-energy proton-induced nuclear reaction on ^{195}Pt results in formation of platinum (^{191}Pt, ^{189}Pt or ^{188}Pt), gold (^{198}Au, ^{196}Au) and iridium (^{194}Ir, ^{192}Ir, ^{190}Ir) isotopes [195]. In turn, it is also possible to obtain the isotopes of palladium (^{101}Pd, ^{100}Pd), silver (^{106}Ag, ^{103}Ag, ^{101}Ag) and ruthenium (^{97}Ru) during the proton-induced nuclear reaction on ^{106}Pd [196]. However, the presented in Figure 53 did not show any of the above-described nuclear reactions. This suggests that due to the use of high-energy protons, the physical mechanism of radiosensitization will not play an important role in the NPs-assisted PIr. For the investigated NPs mainly biological and/or chemical mechanisms seem to be responsible for the observed radiosensitizing effect. This is because – according to the Bethe-Bloch formula – the NPs-related enhancement of proton beam is nearly independent of the atomic number Z. Bethe-Bloch formula describes proton interactions in relation to Z/A (atomic number/mass number) ratio, and is a very slowly varying function. This explains, why bimetallic AuPd NPs and ternary AuPdPt NPs do not show significantly better radiosensitizing properties when compared to monometallic Au NPs (of a similar size, structure and zeta potential). Therefore, it seems that the radiosensitizing effect in PT depends more on the size and/or microstructure of NPs, but only slightly on the metals used. Exemplary, it was shown that in LS180 colon cancer cells, octaarginine-modified Au NPs induced cell-cycle arrest in the G2/M phase, sensitive for irradiation, significantly promoting apoptosis [197]. A similar effect of Au NPs was also observed e.g. in prostate cancer cells [198]. It should be expected that a similar mechanism of radiosensitization, and a possible bystander effect, occurs for the NPs obtained as part of this PhD dissertation [199].

Chapter 5: Summary and conclusions

The preset work resulted in the development of seven types of spherical-like and crystalline noble metal-based NPs: citrate-stabilized ($\approx$ 16 nm) Au NPs, ultra-small ($\approx$ 2 nm) Pt and Pd NPs obtained, respectively, by the polyol method and the reduction with sodium borohydride, two types of bimetallic AuPd NPs ($\approx$ 20 nm) with different palladium shell nanostructures (continuous shell for AuPd CSs and porous one for AuPd NRs), bimetallic AuPt NPs ($\approx$ 28 nm) and ternary AuPdPt ($\approx$ 27 nm) NPs prepared by the green chemistry method with the use of gallic acid. The diameter of the NPs was estimated on the basis of XRD and NTA results, which in some cases differ from those determined directly by TEM. The acquisition of EDS maps made it possible to assess the distribution of elements (Au, Pt and Pd) in multicomponent NPs, confirming that individual metals form separate layers without forming nano-alloy structures. The zeta potential values of these NPs at pH $\approx$ 7 were also determined. These NPs were obtained in order to determine their potential application as nanostructures enhancing the effect of colon (cancer and normal cells irradiation with a proton beam. Colorectal cancer cells (SW480, SW620 and HCT116), as well as normal colon epithelial cells (CRL-1790) were selected for the experiments. For individual cell lines, the maximal non-toxic concentration of NPs was added.

The concentrations of all seven types of NPs (Table 5) and the total PIr dose were determined. The highest toxicity against all cell lines was exhibited for the ultra-small Pd NPs (the toxic effect of CTAB as a NPs stabilizer) and trimetallic AuPdPt NPs (the joined effect of Pt and Pd on the surface of these NPs). On the other hand, the lowest cytotoxicity was found for bimetallic AuPd NPs, for the synthesis with the use of cell-friendly ascorbic acid was used.

The results of PIr of cells cultured with noble metal NPs, as well as holotomographic 3D images of cells cultured with NPs confirmed the hypotheses put forward at the beginning of the PhD dissertation.

- NPs-PIr gives a higher cancer cell death than PIr without the use of NPs.

Both, the results of the MTS cytotoxic assay (Tables 3-5), as well as the determination of cell death by flow cytometry (Tables 6-8), showed that PIr supported by NPs gives a better cytotoxic effect compared to PIr without the use of NPs. This confirms the rationale for the application of nanoradiosensitizers in anticancer therapies. For all tested types of NPs, to a greater or lesser extent, an enhanced effect of such combined PIr was observed. This is confirmed by earlier reports in the literature, where metallic NPs were used to enhance the effect of PIr on cells *in vitro*, but also in the *in vivo* animal model [200]–[203].

- NPs-PIr is selective for cancer cells, being generally non-harmful to normal cells.

In vitro biological studies showed that there is a combined effect of PIr assisted with noble metal NPs. However, this enhancement effect varies between the cell lines. Cancer cell lines, characterized by intensified cell division, are more effectively destroyed by this type of irradiation, which results in a decrease in their proliferation and increased apoptosis rate. Each cancer cell line also has a different response to this combined irradiation scheme, but only

the SW620 and HCT116 cells could be compared with each other, because they were treated with the same non-toxic concentration of NPs (except AuPt NPs, Table 5). The HCT116 cells are-characterized by higher aggressiveness and high resistance even to this scheme of irradiation compared to the SW620 cells.

- NPs with a smaller size and bigger porosity show better radiosensitizing properties.

The final effect of combined PIr depends not so much on the type of the metals used, but rather on the size and nanostructure (porosity) of the NPs. It was showed that the ultra-small Pt NPs and Pd NPs have the larger radiosensitizing effect compared to the others. The small size of NPs provides a highly developed surface, and thus possess more effective radiosensitizing properties. The ultra-small Pd NPs seem to be the best radiosensitizer as its maximum non-toxic concentration was lower than the ultra-small Pt NPs, and the final effect of Pd NPs was mostly more effective than of Pt NPs. The effect of NPs porosity was compared based on two AuPd NPs structures: AuPd CSs with non-porous palladium shell, and AuPd NRs characterized by porous palladium shell. Importantly, both NPs have a similar diameter, consist of the same metals, and were obtained using the same reagents. Thus, they can ideally be compared in terms of their radiosensitizing effect. Decisively better radiosensitizing properties were shown for porous AuPd NRs, which provide a highly developed surface and thus a better contact with cells. Additionally the cells are in contact with both gold and palladium, thus enhancing the toxicity.

- The radiosensitizing effect was mainly due to the biological and chemical mechanism of radiosensitization, rather than to the physical aspects of the interactions of protons with NPs.

The results of the ChPAA showed that the gamma radiation, characteristic for nuclides/isotopes, which could arise from a nuclear reaction of gold, platinum or palladium, was not observed. High PIr energy (225 MeV) means that the chance for a nuclear reaction (cross-section) was relatively low, and therefore the physical effect of radiosensitization is likely to play a negligible role. Therefore, it should sooner be expected that radiosensitization involves the biological-chemical effect of e.g. generating ROS and/or inhibiting the cell cycle in the G2/M phase, when the cells are characterized by the highest radiosensitivity.

- The dynamics of NPs penetration into the cells differs depending on the selected cell line.

3D holotomographic microscopy allowed to evaluate the dynamics of NPs penetration into cells. The location of NPs accumulation differs depending on the selected cell line. After several hours of contact with cells, the NPs locate in the specific sites of cells inside the cell nuclei or arrange uniformly throughout the cell cytoplasm. Figure 63 showed that, the cellular volume occupied by NPs increased linearly with time of culture for all cell lines, although with different – cell specific – magnitude, being most pronounced for the SW620 cells. This means, that the absorption dynamics of the Pd NPs was different for the respective cell lines.

As nano-palladium proved to be the most promising NPs, studies about the use of Pd NPs as radiosensitizers are under development. The preliminary research was appreciated, and I was awarded a research grant in the Preludium 19 call, organized by National Science Centre in Poland. As a part of this project, the influence of the size and shape (spherical and cubic Pd NPs) of NPs on the effectiveness of glioblastoma cells irradiation with proton beam is tested. Additionally, Pd NPs will be coated with polyethylene glycol (PEG), which reduces the cytotoxicity of NPs. Moreover, the Pd NPs will be functionalized by saccharide derivatives, such as glucose or chitosan, which will attach covalently to the cells. These compounds increase the affinity of NPs for e.g. glioblastoma cells, because cancer cells are characterized by increased glucose metabolism (Figure 64). It can be expected that in the future this nanoradiosensitizers could be examined in an *in vivo* model.
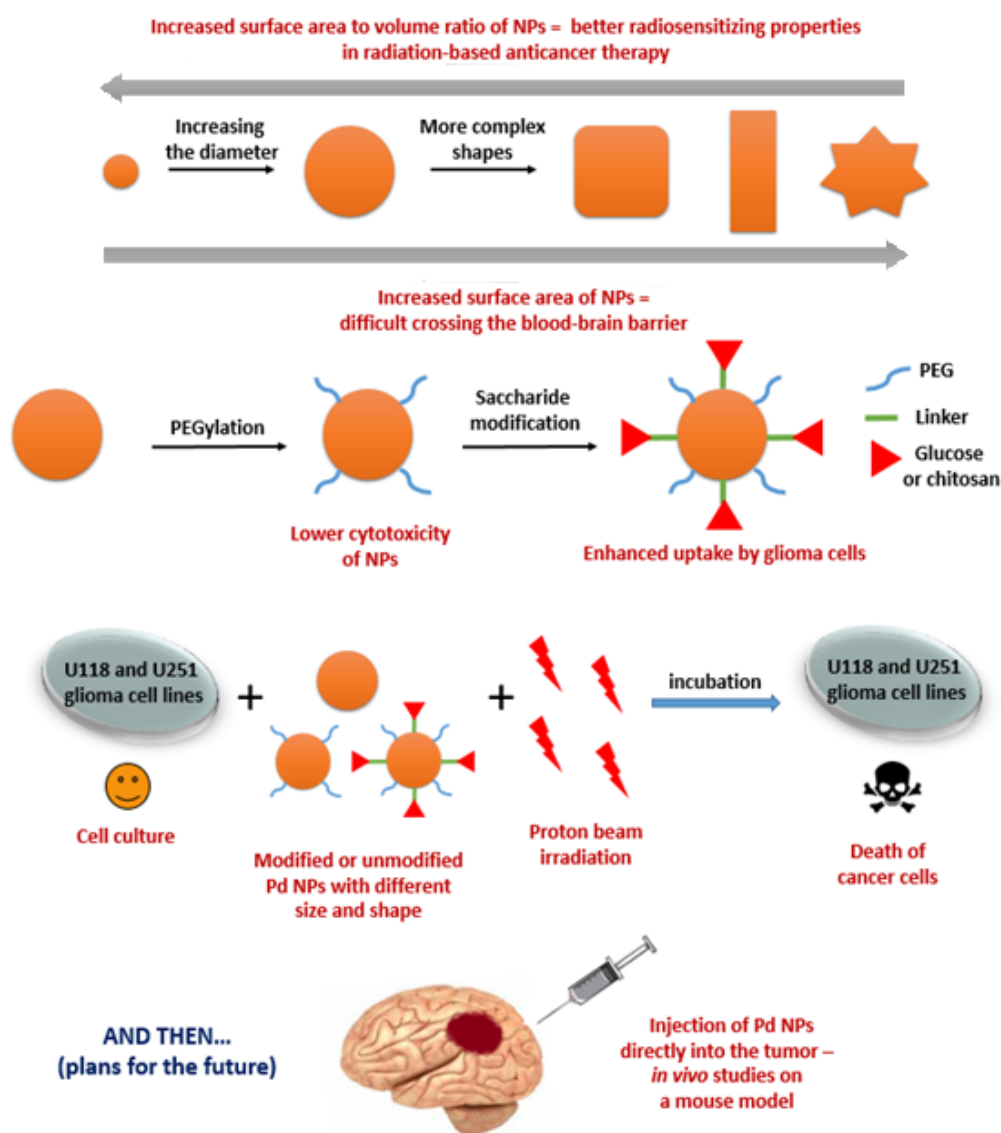
Figure 64. *General idea of further research.*

References

[1] H. Sung *et al.*, "Global Cancer Statistics 2020: GLOBOCAN Estimates of incidence and mortality worldwide for 36 cancers in 185 countries," *CA. Cancer J. Clin.*, vol. 71, no. 3, pp. 209–249, 2021.

[2] Y. Liu, *et al.*, "Molecular mechanisms of chemo- and radiotherapy resistance and the potential implications for cancer treatment," *MedComm*, vol. 2, no. 3, pp. 315–340, 2021.

[3] İ. Altun and A. Sonkaya, "The most common side effects experienced by patients were receiving first cycle of chemotherapy," *Iran. J. Public Health*, vol. 47, no. 8, pp. 1218–1219, 2018.

[4] A. Pearce *et al.*, "Incidence and severity of self-reported chemotherapy side effects in routine care: a prospective cohort study," *PLoS One*, vol. 12, no. 10, e0184360, 2017.

[5] V. Dilalla *et al.*, "Radiotherapy side effects: integrating a survivorship clinical lens to better serve patients," *Curr. Oncol.*, vol. 27, no. 2, pp. 107–112, 2020.

[6] W. D. Newhauser and R. Zhang, "The physics of proton therapy," *Phys. Med. Biol.*, vol. 60, no. 8, pp. R155–R209, 2015.

[7] D. Howard *et al.*, "Chemical mechanisms of nanoparticle radiosensitization and radioprotection: A review of structure-function relationships influencing reactive oxygen species," *Int. J. Mol. Sci.*, vol. 21, no. 2, 579, 2020.

[8] S. Rosa *et al.*, "Biological mechanisms of gold nanoparticle radiosensitization," *Cancer Nanotechnol.*, vol. 8, no. 1, 2, 2017.

[9] B. Klębowski *et al.*, "Applications of noble metal-based nanoparticles in medicine," *Int. J. Mol. Sci.*, vol. 19, no. 12, 4031, 2018.

[10] K. V. Morozov *et al.*, "Radiosensitization by gold nanoparticles: impact of the size, dose rate, and photon energy," *Nanomaterials*, vol. 10, no. 5, 952, 2020.

[11] J. Depciuch *et al.*, "Synthesis method-dependent photothermal effects of colloidal solutions of platinum nanoparticles used in photothermal anticancer therapy," *Appl. Organomet. Chem.*, vol. 34, no. 3, e5401, 2020.

[12] N. Ma *et al.*, "Shape-dependent radiosensitization effect of gold nanostructures in cancer radiotherapy: comparison of gold nanoparticles, nanospikes, and nanorods," *ACS Appl. Mater. Interfaces*, vol. 9, no. 15, pp. 13037–13048, 2017.

[13] N. N. M. Adnan *et al.*, "Effect of gold nanoparticle shapes for phototherapy and drug delivery," *Polym. Chem.*, vol. 7, pp. 2888–2903, 2016.

[14] D. Peukert *et al.*, "Gold nanoparticle enhanced proton therapy: Monte Carlo modeling of reactive species' distributions around a gold nanoparticle and the effects of nanoparticle proximity and clustering," *Int. J. Mol. Sci.*, vol. 20, no. 17, 4280, 2019.

[15] K. Haume *et al.*, "Gold nanoparticles for cancer radiotherapy : a review," *Cancer Nanotechnol.*, vol. 7, 8, 2016.

[16] P. G. Calavia *et al.*, "Photosensitiser-gold nanoparticle conjugates for photodynamic therapy of cancer," *Photochem. Photobiol.* Sci., vol. 17, pp. 1534–1552, 2018.

[17] S. Penninckx *et al.*, "Gold nanoparticles as a potent radiosensitizer: a transdisciplinary approach from physics to patient," *Cancers.*, vol. 12, no. 8, 2021, 2020.

[18] T. T. V. Phan, *et al.*, "An up-to-date review on biomedical applications of palladium nanoparticles," *Nanomaterials*, vol. 10, no. 1, 66, 2020.

[19] S. Alarifi *et al.*, "ROS-mediated apoptosis and genotoxicity induced by palladium nanoparticles in human skin malignant melanoma cells," *Oxid. Med. Cell. Longev.*, vol. 2017, 8439098, 2017.

[20] S. Mukherjee *et al.*, "Improved delivery of doxorubicin using rationally designed PEGylated platinum nanoparticles for the treatment of melanoma," *Mater. Sci. Eng. C*, vol. 108, 110375, 2020.

[21] A. Naseer *et al.*, "Biogenic and eco-benign synthesis of platinum nanoparticles (Pt NPs) using plants aqueous extracts and biological derivatives: environmental, biological and catalytic applications," *J. Mater. Res. Technol.*, vol. 9, no. 4, pp. 9093–9107, 2020.

[22] F. Daneshvar *et al.*, "Combined X-ray radiotherapy and laser photothermal therapy of melanoma cancer cells using dual-sensitization of platinum nanoparticles," *J. Photochem. Photobiol. B Biol.*, vol. 203, 111737, 2020.

[23] S. Li *et al.*, "Platinum nanoparticles: an exquisite tool to overcome radioresistance," *Cancer Nanotechnol.*, vol. 8, no. 1, 4, 2017.

[24] F. G. Wu *et al.*, "Palladium nanosheets as safe radiosensitizers for radiotherapy," *Langmuir*, vol. 36, no. 39, pp. 11637–11644, 2020.

[25] H. Nosrati *et al.*, "Iron oxide and gold bimetallic radiosensitizers for synchronous tumor chemoradiation therapy in 4T1 breast cancer murine model," *J. Mater. Chem. B*, vol. 9, no. 22, pp. 4510–4522, 2021.

[26] S. Ahmed *et al.*, "One pot synthesis of pegylated bimetallic gold–silver nanoparticles for imaging and radiosensitization of oral cancers," *Int. J. Nanomedicine*, vol. 16, pp. 7103–7121, 2021.

[27] J. Cho *et al.*, "Development of bimetallic (Zn@Au) nanoparticles as potential PET-imageable radiosensitizers," *Med. Phys.*, vol. 43, no. 8, pp. 4775–4788, 2016.

[28] J. Jeevanandam *et al.*, "Review on nanoparticles and nanostructured materials: history, sources, toxicity and regulations," *Beilstein J. Nanotechnol.*, vol. 9, no. 1, pp. 1050–1074, 2018.

[29] I. Khan *et al.*, "Nanoparticles: properties, applications and toxicities," *Arab. J. Chem.*, vol. 12, no. 7, pp. 908–931, 2019.

[30] N. T. K. Thanh, *et al.*, "Mechanisms of nucleation and growth of nanoparticles in solution," *Chem. Rev.*, vol. 114, no. 15, pp. 7610–7630, 2014.

[31] C. N. R. Rao, A. Müller, and A. K. Cheetham, *Nanomaterials chemistry: recent developments and new directions*, WILEY-VCH Verlag Gmbh & Co. KGaA, Weinheim, 2007.

[32] H. Lu *et al.*, "Modular and integrated systems for nanoparticle and microparticle synthesis - a review," *Biosensors*, vol. 10, no. 11, 165, 2020.

[33] S. Nabavifard *et al.*, "Application of dendrimer/gold nanoparticles in cancer therapy: a review," *J. Inorg. Organomet. Polym. Mater.*, vol. 30, no. 11, pp. 4231–4244, 2020.

[34]   N. Baig *et al.*, "Nanomaterials: a review of synthesis methods, properties, recent progress, and challenges," *Mater. Adv.*, vol. 2, no. 6, pp. 1821–1871, 2021.

[35]   M. Parashar *et al.*, "Metal oxides nanoparticles via sol–gel method: a review on synthesis, characterization and applications," *J. Mater. Sci. Mater. Electron.*, vol. 31, no. 5, pp. 3729–3749, 2020.

[36]   A. Zieliska-Jurek, J. Reszczyska, E. Grabowska, and A. Zaleska, *Nanoparticles preparation using microemulsion systems*. In: R. Najjar (ed.), *Microemulsions – an introduction to properties and applications.* IntechOpen, London, 2012.

[37]   A. Cid, *Synthesis of NPs by microemulsion method*. In: J. C. Mejuto (ed.), *Microemulsions – a chemical nanoreactor*. IntechOpen, London, 2018.

[38]   Y. J. Zhu and F. Chen, "Microwave-assisted preparation of inorganic nanostructures in liquid phase," *Chem. Rev.*, vol. 114, no. 12, pp. 6462–6555, 2014.

[39]   G. Habibullah *et al.*, "Current strategies for noble metal nanoparticle synthesis," *Nanoscale Res. Lett.*, vol. 16, no. 1, 47, 2021.

[40]   J. Polte, "Fundamental growth principles of colloidal metal nanoparticles – a new perspective," *CrystEngComm*, vol. 17, no. 36, pp. 6809–6830, 2015.

[41]   C. Tan *et al.*, "A self-supporting bimetallic Au@Pt core-shell nanoparticle electrocatalyst for the synergistic enhancement of methanol oxidation," *Sci. Rep.*, vol. 7, no. 1, pp. 6347, 2017.

[42]   M. Aioub *et al.*, "Platinum-coated gold nanorods: efficient reactive oxygen scavengers that prevent oxidative damage toward healthy, untreated cells during plasmonic photothermal therapy," *ACS Nano*, vol. 11, no. 1, pp. 579–586, 2017.

[43]   B. Klebowski *et al.*, "Fancy-shaped gold–platinum nanocauliflowers for improved proton irradiation effect on colon cancer cells," *Int. J. Mol. Sci.*, vol. 21, no. 24, 9610, 2020.

[44]   G. Zhang *et al.*, "Green synthesis and characterization of Au@Pt core-shell bimetallic nanoparticles using gallic acid," *J. Phys. Chem. Solids*, vol. 81, pp. 79–87, 2015.

[45]   E. Drzymała *et al.*, "Design and assembly of ternary Pt/Re/SnO2 NPs by controlling the zeta potential of individual Pt, Re, and SnO2 NPs," *J. Nanoparticle Res.*, vol. 20, no. 5, 144, 2018.

[46]   A. Owen "The application of nanotechnology in medicine: treatment and diagnostics," *Nanomedicine*, vol. 9, no *et al.*,. 9, pp. 1291–1294, 2014.

[47]   S. Soares *et al.*, "Nanomedicine: principles, properties, and regulatory issues," *Front. Chem.*, vol. 6, 360, 2018.

[48]   E. Alphandéry, "Natural metallic nanoparticles for application in nano-oncology," *Int. J. Mol. Sci.*, vol. 21, no. 12, 4412, 2020.

[49]   W. Zhang *et al.*, "Development of polymeric nanoparticles for blood–brain barrier transfer— strategies and challenges," *Adv. Sci.*, vol. 8, no. 10, pp. 1–32, 2021.

[50]   E. Blanco *et al.*, " Principles of nanoparticle design for overcoming biological barriers to drug delivery," *Nat. Biotechnol.*, vol. 33, no. 9, pp. 941–951, 2015.

[51]   J. A. Champion and S. Mitragotri, "Shape induced inhibition of phagocytosis of polymer

particles," *Pharm. Res.*, vol. 26, no. 1, pp. 244–249, 2009.

[52]   G. Thurston *et al.*, "Cationic liposomes target angiogenic endothelial cells in tumors and chronic inflammation in mice.," *J. Clin. Invest.*, vol. 101, no. 7, pp. 1401–1413, 1998.

[53]   G. Vinci and M. Rapa, "Noble metal nanoparticles applications: recent trends in food control," *Bioengineering*, vol. 6, no. 1, 10, 2019.

[54]   H. T. Phan and A. J. Haes, "What does nanoparticle stability mean?," *J. Phys. Chem. C Nanomater. Interfaces*, vol. 123, no. 27, pp. 16495–16507, 2019.

[55]   P. N. Navya and H. K. Daima, "Rational engineering of physicochemical properties of nanomaterials for biomedical applications with nanotoxicological perspectives," *Nano Converg.*, vol. 3, no. 1, 1, 2016.

[56]   B. Halamoda-Kenzaoui *et al.*, "The agglomeration state of nanoparticles can influence the mechanism of their cellular internalisation," *J. Nanobiotechnology*, vol. 15, no. 1, pp. 1–15, 2017.

[57]   F. Boateng and W. Ngwa, "Delivery of nanoparticle-based radiosensitizers for radiotherapy applications," *Int. J. Mol. Sci.*, vol. 21, no. 1, 273, 2020.

[58]   K. Habiba *et al.*, "Enhancing colorectal cancer radiation therapy efficacy using silver nanoprisms decorated with graphene as radiosensitizers," *Sci. Rep.*, vol. 9, no. 1, 17120, 2019.

[59]   G. Sanità *et al.*, "Nanoparticle surface functionalization: how to improve biocompatibility and cellular internalization," *Front. Mol. Biosci.*, vol. 7, 587012, 2020.

[60]   Y. Chen *et al.*, "Surface modification of gold nanoparticles with small molecules for biochemical analysis," *Acc. Chem. Res.*, vol. 50, no. 2, pp. 310–319, 2017.

[61]   J. Zhou *et al.*, "Ovalbumin-modified nanoparticles increase the tumor accumulation by a tumor microenvironment-mediated 'giant,'" *J. Mater. Chem. B*, vol. 8, no. 33, pp. 7528–7538, 2020.

[62]   C. D. Zhu *et al.*, "Synthesis of novel galactose functionalized gold nanoparticles and its radiosensitizing mechanism," *J. Nanobiotechnology*, vol. 13, no. 1, 67, 2015.

[63]   A. C. Quevedo *et al.*, "Mechanisms of silver nanoparticle uptake by embryonic zebrafish cells," *Nanomaterials*, vol. 11, no. 10, 2699, 2021.

[64]   T. Wang *et al.*, "Cellular uptake of nanoparticles by membrane penetration: a study combining confocal microscopy with FTIR spectroelectrochemistry," *ACS Nano*, vol. 6, no. 2, pp. 1251–1259, 2012.

[65]   J. J. Rennick *et al.*,, "Key principles and methods for studying the endocytosis of biological and nanoparticle therapeutics," *Nat. Nanotechnol.*, vol. 16, no. 3, pp. 266–276, 2021.

[66]   M. Miaczynska and H. Stenmark, "Mechanisms and functions of endocytosis," *J. Cell Biol.*, vol. 180, no. 1, pp. 7–11, 2008.

[67]   P. Sabourian *et al.*, "Effect of physico-chemical properties of nanoparticles on their intracellular uptake," *Int. J. Mol. Sci.*, vol. 21, no. 21, 8019, 2020.

[68]   L. Treuel *et al.*,, "New views on cellular uptake and trafficking of manufactured nanoparticles," *J. R. Soc. Interface*, vol. 10, no. 82, 20120939, 2013.

[69]	L. Palanikumar *et al.*, "pH-responsive high stability polymeric nanoparticles for targeted delivery of anticancer therapeutics," *Commun. Biol.*, vol. 3, no. 1, 95, 2020.

[70]	X. Ma *et al.*, "Gold nanoparticles induce autophagosome accumulation through size-dependent nanoparticle uptake and lysosome impairment," *ACS Nano*, vol. 5, no. 11, pp. 8629–8639, 2011.

[71]	P. Ughachukwu and P. Unekwe, "Efflux pump-mediated resistance in chemotherapy," *Ann. Med. Health Sci. Res.*, vol. 2, no. 2, pp. 191–198, 2012.

[72]	M. S. Moghaddam *et al.*, "Enhanced cellular uptake of nanoparticles by increasing the hydrophobicity of poly(lactic acid) through copolymerization with cell-membrane-lipid components," *Chem. Commun.*, vol. 51, no. 78, pp. 14605–14608, 2015.

[73]	D. Zhang *et al.*, "The morphology and surface charge-dependent cellular uptake efficiency of upconversion nanostructures revealed by single-particle optical microscopy," *Chem. Sci.*, vol. 9, no. 23, pp. 5260–5269, 2018.

[74]	X. Cheng *et al.*, "Protein corona influences cellular uptake of gold nanoparticles by phagocytic and nonphagocytic cells in a size-dependent manner," *ACS Appl. Mater. Interfaces*, vol. 7, no. 37, pp. 20568–20575, 2015.

[75]	K. Riehemann *et al.*, "Nanomedicine – challenge and perspectives," *Angew. Chemie – Int. Ed.*, vol. 48, no. 5, pp. 872–897, 2009.

[76]	S. Tenzer *et al.*, "Rapid formation of plasma protein corona critically affects nanoparticle pathophysiology," *Nat. Nanotechnol.*, vol. 8, no. 10, pp. 772–781, 2013.

[77]	S. J. Park, "Protein–nanoparticle interaction: corona formation and conformational changes in proteins on nanoparticles," *Int. J. Nanomedicine*, vol. 15, pp. 5783–5802, 2020.

[78]	C. T. Lu *et al.*, "Current approaches to enhance CNS delivery of drugs across the brain barriers," *Int. J. Nanomedicine*, vol. 9, no. 1, pp. 2241–2257, 2014.

[79]	S. Y. Fam *et al.*, "Stealth coating of nanoparticles in drug-delivery systems," *Nanomaterials*, vol. 10, no. 4, 787, 2020.

[80]	B. Fraser *et al.*, "Biocompatible nanomaterials as an emerging technology in reproductive health; a focus on the male," *Front. Physiol.*, vol. 12, 753686, 2021.

[81]	D. Hanahan, "Hallmarks of Cancer: New Dimensions," *Cancer Discov.*, vol. 12, no. 1, pp. 31–47, 2022.

[82]	D. Hanahan and R. A. Weinberg, "Hallmarks of cancer: The next generation," *Cell*, vol. 144, no. 5, pp. 646–674, 2011.

[83]	L. Kelland, "Targeting the limitless replicative potential of cancer: the telomerase/telomere pathway," *Clin. Cancer Res.*, vol. 13, no. 17, pp. 4960–4963, 2007.

[84]	L. M. Phan *et al.*,"Cancer metabolic reprogramming: importance, main features, and potentials for precise targeted anti-cancer therapies," *Cancer Biol. Med.*, vol. 11, no. 1, pp. 1–19, 2014.

[85]	D. S. Vinay *et al.*, "Immune evasion in cancer: mechanistic basis and therapeutic strategies," *Semin. Cancer Biol.*, vol. 35, pp. S185–S198, 2015.

[86]	T. L. Vincent and R. A. Gatenby, "An evolutionary model for initiation, promotion

and progression in carcinogenesis," *Int. J. Oncol.*, vol. 32, no. 4, pp. 729–737, 2008.

[87] W. Troll and R. Wiesner, "The role of oxygen radicals as a possible mechanism of tumor promotion," *Annu. Rev. Pharmacol. Toxicol.*, vol. 25, no. 5, pp. 509–528, 1985.

[88] F. D. Shah *et al.*, "A review on salivary genomics and proteomics biomarkers in oral cancer," *Indian J. Clin. Biochem.*, vol. 26, no. 4, pp. 326–334, 2011.

[89] P. M. Speight, "Update on oral epithelial dysplasia and progression to cancer," *Head Neck Pathol.*, vol. 1, no. 1, pp. 61–66, 2007.

[90] O. A. M. Carlo *et al.*, "Evaluation of classical mathematical models of tumor growth," *Appl. Sci.*, vol. 11, no. 11, 5241, 2021.

[91] C. Vaghi *et al.*, "Population modeling of tumor growth curves and the reduced Gompertz model improve prediction of the age of experimental tumors," *PLoS Comput. Biol.*, vol. 16, no. 2, e1007178, 2020.

[92] E. Akin *et al.*, "Parameter identification for gompertz and logistic dynamic equations," *PLoS One*, vol. 15, no. 4, e0230582, 2020.

[93] A. Paumier and C. Le Péchoux, "Post-operative radiation therapy," *Transl. Lung Cancer Res.*, vol. 2, no. 5, pp. 423–432, 2013.

[94] S. T. Lutz, *et al.*, "Role of radiation therapy in palliative care of the patient with cancer," *J. Clin. Oncol.*, vol. 32, no. 26, pp. 2913–2919, 2014.

[95] E. S. Shibu *et al.*, "Nanomaterials formulations for photothermal and photodynamic therapy of cancer," *J. Photochem. Photobiol. C Photochem. Rev.*, vol. 15, no. 1, pp. 53–72, 2013.

[96] C. X. Huang *et al.*, "Controlled synthesis of upconverting nanoparticles/CuS yolk-shell nanoparticles for: *in vitro* synergistic photothermal and photodynamic therapy of cancer cells," *J. Mater. Chem. B*, vol. 5, no. 48, pp. 9487–9496, 2017.

[97] X. G. Xu *et al.*, "A review of dosimetry studies on external-beam radiation treatment with respect to second cancer induction," *Phys. Med. Biol*, vol. 53, no. 13, pp. R193–R241, 2008.

[98] S. Gianfaldoni *et al.*, "An overview on radiotherapy: from its history to its current applications in dermatology," *Open Access Maced. J. Med. Sci.*, vol. 5, no. 4, pp. 521–525, 2017.

[99] A. Sahgal *et al.*, "Stereotactic body radiotherapy versus conventional external beam radiotherapy in patients with painful spinal metastases: an open-label, multicentre, randomised, controlled, phase 2/3 trial," *Lancet Oncol.*, vol. 22, no. 7, pp. 1023–1033, 2021.

[100] T. D. Malouff *et al.*, "Boron neutron capture therapy: A review of clinical applications," *Front. Oncol.*, vol. 11, 601820, 2021.

[101] Y. Matsumoto *et al.*, "A critical review of radiation therapy: from particle beam therapy (proton, carbon, and bnct) to beyond," *J. Pers. Med.*, vol. 11, no. 8, 825, 2021.

[102] S. C. Kamran *et al.*, "Proton versus photon-based radiation therapy for prostate cancer: emerging evidence and considerations in the era of value-based cancer care," *Prostate Cancer Prostatic Dis.*, vol. 22, no. 4, pp. 509–521, 2019.

[103] Z. Kuncic and S. Lacombe, "Nanoparticle radio-enhancement: principles, progress

and application to cancer treatment,", *Phys. Med. Phys.*, vol. 63, no 2, 02TR01, 2018.

[104] D. Kwatra *et al*., "Nanoparticles in radiation therapy: a summary of various approaches to enhance radiosensitization in cancer," *Transl. Cancer Res.*, vol. 2, no. 4, pp. 330–342, 2013.

[105] L. Gong *et al*., "Application of radiosensitizers in cancer radiotherapy," *Int. J. Nanomedicine*, vol. 16, pp. 1083–1102, 2021.

[106] E. Q. Youkhana *et al*., "Titanium dioxide nanoparticles as radiosensitisers : an *in vitro* and phantom-based study," *Int. J. Med. Sci.,* vol. 14, no. 6, pp. 602–614, 2017.

[107] N. B. T. Sisin *et al*., "Synergetic influence of bismuth oxide nanoparticles, cisplatin nd baicalein-rich fraction on reactive oxygen species generation and radiosensitization effects for clinical radiotherapy beams," *Int. J. Nanomedicine*, vol. 15, pp. 7805–7823, 2020.

[108] T. J. Meyer *et al.*, "The radiosensitizing effect of zinc oxide nanoparticles in sub-cytotoxic dosing as associated with oxidative stress *in vitro*," *Materials*, vol. 12, no. 24, 4062, 2019.

[109] H. Yang, "Enhancement of radiosensitization by silver nanoparticles functionalized with polyethylene glycol and aptamer As1411 for glioma irradiation therapy," *Int. J. Nanomedicine*, vol. 14, pp. 9483–9496, 2019.

[110] A. Konefał *et al.*, "Influence of a shape of gold nanoparticles on the dose enhancement in the wide range of gold mass concentration for high-energy X-ray beams from a medical linac," *Rep. Pract. Oncol. Radiother.,* vol. 25, no. 4, pp. 579–585, 2020.

[111] E. S. Shiryaeva *et al.*, "Hafnium oxide as a nanoradiosensitizer under X-ray irradiation of aqueous organic systems: a model study using the spin-trapping technique and Monte Carlo simulations," *J. Phys. Chem.*, vol. 123, no. 45, pp. 27375–27384, 2019.

[112] C. Cunningham *et al.*, "Radiosensitization effect of gold nanoparticles in proton therapy," *Front. Public Heal.*, vol. 9, 600822, 2021.

[113] https://pocketdentistry.com/5-the-biological-effects-associated-with-x-rays-risk-and-practical-radiation-protection/ (accessed: 28.12.2021 r).

[114] O. Desouky *et al.*, "Targeted and non-targeted effects of ionizing radiation," *J. Radiat. Res. Appl. Sci.*, vol. 8, no. 2, pp. 247–254, 2015.

[115] F. Hespeels *et al.*, "Experimental measurements validate the use of the binary encounter approximation model to accurately compute proton induced dose and radiolysis enhancement from gold nanoparticles," *Phys. Med. Biol.*, vol. 64, no. 6, 065014, 2019.

[116] J. Choi *et al.*, "Radiosensitizing high-Z metal nanoparticles for enhanced radiotherapy of glioblastoma multiforme," *J. Nanobiotechnology*, vol. 18, 122, 2020.

[117] A. Marín *et al.*, "Bystander effects and radiotherapy," *Reports Pract. Oncol. Radiother.*, vol. 20, no. 1, pp. 12–21, 2015.

[118] R. Abdul Rashid *et al.*, "Radiosensitization effects and ROS generation by high Z metallic nanoparticles on human colon carcinoma cell (HCT116) irradiated under 150 MeV proton beam," *OpenNano*, vol. 4, 100027, 2019.

[119] S. J. Seo *et al.*, "Reactive oxygen species-based measurement of the dependence of the Coulomb nanoradiator effect on proton energy and atomic Z value," *Int. J. Radiat. Biol.*, vol. 93, no. 11,

pp. 1239–1247, 2017.

[120] A. Jamil *et al.*, "Radiosensitization effects by bismuth oxide nanorods of different sizes in megavoltage external beam radiotherapy," *Reports Pract. Oncol. Radiother.*, vol. 26, no. 5, pp. 773–784, 2021.

[121] N. Aunps *et al.*, "Hypoxia and cellular localization influence the radiosensitizing fffect of gold hypoxia and cellular localization influence the radiosensitizing fffect of gold nanoparticles (AuNPs) in breast cancer cells," *Radiat. Res.*, vol. 182, no. 5, 475–488, 2014.

[122] https://clinicaltrials.gov/ct2/show/NCT03818386 (accessed 3.01.2022 r).

[123] P. Hu *et al.*, "Gadolinium-based banoparticles for theranostic MRI-guided radiosensitization in hepatocellular carcinoma," *Front. Bioeng. Biotechnol.*, vol. 7, 368, 2019.

[124] F. Shan *et al.*, "Investigation of simultaneously existed Raman scattering enhancement and inhibiting fluorescence using surface modified gold nanostars as SERS probes," *Sci. Rep.*, vol. 7, no. 1, 6813, 2017.

[125] Y. Gao and L. Torrente-Murciano, "Mechanistic insights of the reduction of gold salts in the Turkevich protocol," *Nanoscale*, vol. 3, pp. 2740–2751, 2020.

[126] J. Dong *et al.*, "Synthesis of precision gold nanoparticles using Turkevich method." *Kona*, vol. 37, 224–232, 2020.

[127] J. Schröder *et al.*, "Anion dependent particle size control of platinum nanoparticles synthesized in ethylene glycol," *Nanomaterials*, vol. 11, no. 8, 2092, 2021.

[128] M. Wei *et al.*, "Seed-mediated synthesis of gold nanorods at low concentrations of CTAB," *ACS Omega*, vol. 6, no. 13, 9188–9195, 2021.

[129] A. M. Mecan *et al.*, "Therapeutic perspective of vitamin C and its derivatives," *Antioxidants*, vol. 8, no. 8, 247, 2019.

[130] M. G. Montes De Oca *et al.*, "Hydrogen adsorption at strained Pd nanoshells," *J. Phys. Chem. C*, vol. 115, no. 21, pp. 10489–10496, 2011.

[131] A. K. Mittal *et al.*, "Quercetin and gallic acid mediated synthesis of bimetallic (Ag-Se) nanoparticles and their antitumor and antimicrobial potential," *J. Colloid Interface Sci.*, vol. 431, 194–199, 2014.

[132] M. F. Zayed *et al.*, "Gallic acid-assisted growth of cuprous oxide within polyvinyl alcohol; a separable catalyst for oxidative and reductive degradation of water pollutants," *J. Clean. Prod.*, vol. 279, 123826, 2021.

[133] A. Lunkov *et al.*, "Synthesis of silver nanoparticles using gallic acid-conjugated chitosan derivatives," *Carbohydr. Polym.*, vol. 234, 115916, 2020.

[134] T. Zhang *et al.*, "Gallic acid has anticancer activity and enhances the anticancer effects of cisplatin in non-small cell lung cancer A549 cells via the JAK/STAT3 signaling pathway," *Oncol. Rep.*, vol. 44, no. 3, pp. 1779–1788, 2019.

[135] L. E. Franken *et al.*, "A technical introduction to transmission electron microscopy for soft-matter: imaging, possibilities, choices, and technical developments," *Small*, vol. 16, no. 14, 1906198, 2020.

[136] D. B. Williams and C. B. Carter, *Transmission electron microscopy*. Springer, New York, 2009.

[137] https://commons.wikimedia.org/wiki/File:Scheme_TEM_en.svg (accessed 13.01.2022 r).

[138] https://commons.wikimedia.org/wiki/File:EDX-scheme.svg (accessed 13.01.2022 r).

[139] M. Scimeca *et al.*, "Energy Dispersive X-ray (EDX) microanalysis: a powerful tool in biomedical research and diagnosis," *Eur. J. Histochem.*, vol. 62, no. 1, 2841, 2018.

[140] M. A. Asadabad and M. J. Eskandari, *Electron diffraction*. In: M. Janecek and R. Kral (eds.), *Modern electron microscopy in physical and life sciences.* IntechOpen, London, 2016.

[141] M. Piešová *et al.*, "Experimental quantification of the austenitic phase in steels using the average peak method of X-ray diffractometry," *Procedia Eng.*, vol. 13, no. 2, pp. 34–36, 2017.

[142] Z. Jiang *et al.*, "Reconstruction of evolving nanostructures in ultrathin films with X-ray waveguide fluorescence holography," *Nat. Commun.*, vol. 11, 3197, 2020.

[143] M. O. Fatehah *et al.*, "Nanoparticle properties, behavior, fate in aquatic systems," *J. Colloid Sci. Biotechnol.* vol. 3, no. 2, pp. 111–140, 2014.

[144] C. N. Lunardi *et al.*, "Experimental methods in chemical engineering: zeta potential," *Can. J. Chem. Eng.*, vol. 99, no. 3, pp. 627–639, 2021.

[145] G. V. Lowry *et al.*, "Guidance to improve the scientific value of zeta-potential measurements in nanoEHS," *Environ. Sci. Nano*, vol. 3, no. 5, pp. 953–965, 2016.

[146] R. A. Dragovic *et al.*, "Sizing and phenotyping of cellular vesicles using nanoparticle tracking analysis," *Nanomed.: Nanotechnol. Biol. Med.*, vol. 7, no. 6, pp. 780–788, 2011.

[147] A. Kim *et al.* "Validation of size estimation of nanoparticle tracking analysis on polydisperse macromolecule assembly," *Sci. Rep.*, vol. 9, no. 1, 2639, 2019.

[148] A. Vertes, S. Nagy, Z. Klencsar, R. G. Lovas and F. Rosch, *Handbook of nuclear chemistry,* Springer, New York, 2011.

[149] M. B. Krzyworzeka *et al.* "Colorectal cancer - derived microvesicles modulate differentiation of human monocytes to macrophages," *J. Transl. Med.*, vol. 14, 36, 2016.

[150] C. Ares *et al.*, "Pencil beam scanning proton therapy for pediatric intracranial ependymoma," *J. Neurooncol.*, vol. 128, no. 1, pp. 137–145, 2016.

[151] D. Wlodkowic *et al.*, "Apoptosis and beyond: cytometry in studies of programmed cell death," *Methods Cell Biol.*, vol. 103, pp. 55-98, 2011.

[152] R. Nunez, "DNA measurement and cell cycle analysis by flow cytometry," *Curr. Issues Mol. Biol.*, vol. 3, no. 3, pp. 67–70, 2001.

[153] E. Schepers *et al.*, "Flow cytometric calcium flux assay: evaluation of cytoplasmic calcium kinetics in whole blood leukocytes," *J. Immunol. Methods*, vol. 348, no. 1–2, pp. 74–82, 2009.

[154] A. Adan *et al.*, "Flow cytometry: basic principles and applications," *Crit. Rev. Biotechnol.*, vol. 37, no. 2, pp. 163–176, 2017.

[155] https://commons.wikimedia.org/wiki/Category:Flow_cytometry#/media/File:Flow_cytometry (accessed: 17.01.2022 r)

[156] T. A. Stanly *et al.*, "Quantitative optical diffraction tomography imaging of mouse platelets," *Front Physiol.*, vol. 11, 568087, 2020.

[157] S. Salucci *et al.*, "Holotomographic microscopy: a new approach to detect apoptotic cell features," *Microsc. Res. Tech.*, vol. 83, no. 12, pp. 1464–1470, 2020.

[158] A. Berdeu *et al.*, "Lens-free microscopy for 3D + time acquisition of 3D cell culture", *Sci. Rep.*, vol. 8, 16135, 2018.

[159] C. Wang and D. Astruc, " Nanogold plasmonic photocatalysis for organic nanogold plasmonic photocatalysis for organic synthesis and clean energy conversion," *Chem. Soc. Rev.*, vol. 43, pp. 7188–7216, 2014.

[160] N. Tran *et al*., "Rough-surface gold nanoparticles for plasmonic light absorption enhancement in organic," *Sci. Adv. Mater.*, vol. 9, no. 9, pp. 1522–1526, 2017.

[161] S.R. Atriardi *et al*., "Modification of boron-doped diamond electrodes with platinum-iridium for carbon dioxide electroreduction" *IOP Conf. Ser.: Mater. Sci. Eng.*, vol. 496, 012040, 2019.

[162] K. S. Siddiqi and A. Husen, "Green synthesis, characterization and sses of palladium/platinum nanoparticles," *Nanoscale Res. Lett.*, vol. 11, 482, 2016.

[163] A. K. Wójcik *et al*., "Determination of iodine concentration in aqueous solutions by proton activation analysis: preliminary results for digested human thyroids," *J. Radioanal. Nucl. Chem.*, vol. 291, no. 2, pp. 415–419, 2012.

[164] M. Kutwin *et al.*, "Nanocomplexes of graphene oxide and platinum nanoparticles against colorectal cancer colo205, HT-29, HTC-116, SW480, liver cancer HepG2, human breast cancer MCF-7, and adenocarcinoma LNCaP and human cervical Hela B cell lines," *Materials*, vol. 16, no. 6, 909, 2019.

[165] F. Luo *et al.*, "Comparative profiling between primary colorectal carcinomas and metastases identifies heterogeneity on drug resistance," *Oncotarget*, vol. 7, no. 39, pp. 63937–63949, 2016.

[166] http://onkologia.org.pl/ (accessed 18.01.2022 r)

[167] C. Pucci *et al.*, "Innovative approaches for cancer treatment: current perspectives and new challenges," *Ecancermedicalscience*, vol. 13, 961, 2019.

[168] M. Vidal *et al.*,"Future technological developments in proton therapy – a predicted technological breakthrough," *Cancer Radiother.*, vol. 25, no. 6–7, pp. 554–564, 2021.

[169] M. Kus-Liśkiewicz *et al.*, "Biocompatibility and cytotoxicity of gold nanoparticles: recent advances in methodologies and regulations," *Int. J. Mol. Sci.*, vol. 22, no. 20, 10952, 2021.

[170] S. Penninckx *et al.*, "Metallic nanoparticles: a useful prompt gamma emitter for range monitoring in proton therapy?," *Radiation*, vol. 1, no. 4, pp. 305–316, 2021.

[171] J. R. Gurr *et al.* "Ultrafine titanium dioxide particles in the absence of photoactivation can induce oxidative damage to human bronchial epithelial cells," *Toxicology*, vol. 213, no. 1–2, pp. 66–73, 2005.

[172] E. J. Petersen and B. C. Nelson, "Mechanisms and measurements of nanomaterial-induced oxidative damage to DNA," *Anal. Bioanal. Chem.*, vol. 398, no. 2, pp. 613-650, 2010.

[173] S. S. Dukhin and M. E. Labib, "Convective diffusion of nanoparticles from the epithelial barrier toward regional lymph nodes," *Adv. Colloid Interface Sci.*, vol. 199–200, pp. 23–43, 2013.

[174] G. Oberdörster *et al.*, "Principles for characterizing the potential human health effects from exposure to nanomaterials: elements of a screening strategy," *Part. Fibre Toxicol.*, vol. 2, 8, 2005.

[175] P. Ruenraroengsak *et al.*, "Respiratory epithelial cytotoxicity and membrane damage (holes) caused by amine-modified nanoparticles," *Nanotoxicology*, vol. 6, no. 1, pp. 94–108, 2012.

[176] S. Barua and S. Mitragotri, "Challenges associated with penetration of nanoparticles across cell and tissue barriers: a review of current status and future prospects," *Nano Today*, vol. 9, no. 2, pp. 223–243, 2014.

[177] B. Contreras-Trigo *et al.*, "Slight pH fluctuations in the gold nanoparticle synthesis process influence the performance of the citrate reduction method," *Sensors*, vol. 18, no. 7, 2246, 2018.

[178] J. Guo *et al.*, "Positively charged, surfactant-free gold nanoparticles for nucleic acid delivery," *RSC Adv.*, vol. 5, no. 23, pp. 17862–17871, 2015.

[179] Y. Z. Wu *et al.*, "Evaluation of gallic acid-coated gold nanoparticles as an anti-aging ingredient," *Pharmaceuticals*, vol. 14, no. 11, 1071, 2021.

[180] A. Chakraborty and N. R. Jana, "Vitamin C-conjugated nanoparticle protects cells from oxidative stress at low doses but induces oxidative stress and cell death at high doses," *ACS Appl. Mater. Interfaces*, vol. 9, no. 48, pp. 41807–41817, 2017.

[181] E. Pawlowska *et al.*, "Pro- and antioxidant effects of vitamin C in cancer in correspondence to its dietary and pharmacological concentrations," *Oxid. Med. Cell. Longev.*, vol. 2019, 7286737, 2019.

[182] M. Bhamidipati and L. Fabris, "Multiparametric assessment of gold nanoparticle cytotoxicity in cancerous and healthy cells: the role of size, shape, and surface chemistry," *Bioconjug. Chem.*, vol. 28, no. 2, pp. 449–460, 2017.

[183] M. Weiss *et al.*, "Density of surface charge is a more predictive factor of the toxicity of cationic carbon nanoparticles than zeta potential," *J. Nanobiotechnology*, vol. 19, 6, 2021.

[184] X. R. Shao *et al.*, "Independent effect of polymeric nanoparticle zeta potential/surface charge, on their cytotoxicity and affinity to cells," *Cell Prolif.*, vol. 48, no. 4, pp. 465–474, 2015.

[185] C. Carnovale *et al.*, "Identifying trends in gold nanoparticle toxicity and uptake: size, shape, capping ligand, and biological corona," *ACS Omega*, vol. 4, no. 1, pp. 242–256, 2019.

[186] S. Park and J. Kim, "Preoperative chemoradiation for locally advanced rectal cancer: comparison of three radiation dose and fractionation schedules,", *Radiat. Oncol. J.*, vol. 34, no. 2, pp. 96–105, 2016.

[187] K.B. Lee *et al.*, "Low energy proton beam induces tumor cell apoptosis through reactive oxygen species and activation of caspases," *Exp. Mol. Med.*, vol. 40, no. 1, pp. 118–129, 2008.

[188] J. Miszczyk *et al.*, "Therapeutic proton irradiation results in apoptosis and caspase-3 activation in human peripheral blood lymphocytes," *Transl. Cancer Res.*, vol. 7, no. 4, pp. 879–889, 2018.

[189] C. Choi *et al.* "Comparison of proton and photon beam irradiation in radiation-induced intestinal

injury using a mouse model," *Int. J. Mol. Sci.*, vol. 20, no. 8, 1894, 2019.

[190] I. Baran *et al.*, "Detailed analysis of apoptosis and delayed luminescence of human leukemia Jurkat T cells after proton irradiation and treatments with oxidant agents and flavonoids," *Oxid. Med. Cell. Longev.*, vol. 2012, pp. 7–9, 2012.

[191] M. U. Rehman *et al.*, "Dual effects of nanoparticles on radiation therapy: as radiosensitizers and radioprotectors," *Radiat. Environ. Med.*, vol. 5, no. 1, pp. 40–45, 2016.

[192] Y. Lin *et al.* "Comparing gold nano-particle enhanced radiotherapy with protons, megavoltage photons and kilovoltage photons: A Monte Carlo simulation," *Phys. Med. Biol.*, vol. 59, no. 24, pp. 7675–7689, 2014.

[193] K. C. Nguyen *et al.*, "Mitochondrial toxicity of cadmium telluride quantum dot nanoparticles in mammalian hepatocytes," *Toxicol. Sci.*, vol. 146, no. 1, pp. 31–42, 2015.

[194] F. Ditroi *et al.*, "Activation cross sections of proton induced nuclear reactions on gold up to 65 MeV," *Appl. Radiat. Isot.*, vol. 113, pp. 96–109, 2016.

[195] F. Ditroi *et al.*, "Extension of activation cross section data of long lived products in deuteron induced nuclear reactions on platinum up to 50 MeV," *Nucl. Instruments Methods Phys. Res. Sect. B Beam Interact. with Mater. Atoms*, vol. 401, pp. 56–70, 2017.

[196] F. Tárkányi *et al.*, "Activation cross sections of proton induced nuclear reactions on palladium up to 80 MeV," *Appl. Radiat. Isot.*, vol. 114, pp. 128–144, 2016.

[197] X. Zhang *et al.*, "Octaarginine-modified gold nanoparticles enhance the radiosensitivity of human colorectal cancer cell line LS180 to megavoltage radiation," *Int. J. Nanomedicine*, vol. 13, pp. 3541–3552, 2018.

[198] W. Roa *et al.*, "Gold nanoparticle sensitize radiotherapy of prostate cancer cells by regulation of the cell cycle," *Nanotechnology*, vol. 20, no. 37, 375101, 2009.

[199] J. Thariat *et al.*, "Hadrontherapy interactions in molecular and cellular biology," *Int. J. Mol. Sci.*, vol. 21, no. 1, 133, 2020.

[200] T. Schlathölter *et al.*, "Improving proton therapy by metal-containing nanoparticles: nanoscale insights," *Int. J. Nanomedicine*, vol. 11, pp. 1549–1556, 2016.

[201] W. B. Li *et al.*, "Application of high-Z gold nanoparticles in targeted cancer radiotherapy–pharmacokinetic modeling, monte carlo simulation and radiobiological effect modeling," *Cancers.*, vol. 13, no. 21, 5370, 2021.

[202] S. Zwiehoff *et al.*, "Enhancement of proton therapy efficiency by noble metal nanoparticles is driven by the number and chemical activity of surface atoms," *Small*, vol. 18, no. 9, e2106383, 2021.

[203] S. Li *et al.*, "Antibody-functionalized gold nanoparticles as tumor-targeting radiosensitizers for proton therapy," *Nanomedicine*, vol. 14, no. 3, pp. 317–333, 2019.

Supplementary information

1) MTS cell viability – detailed results
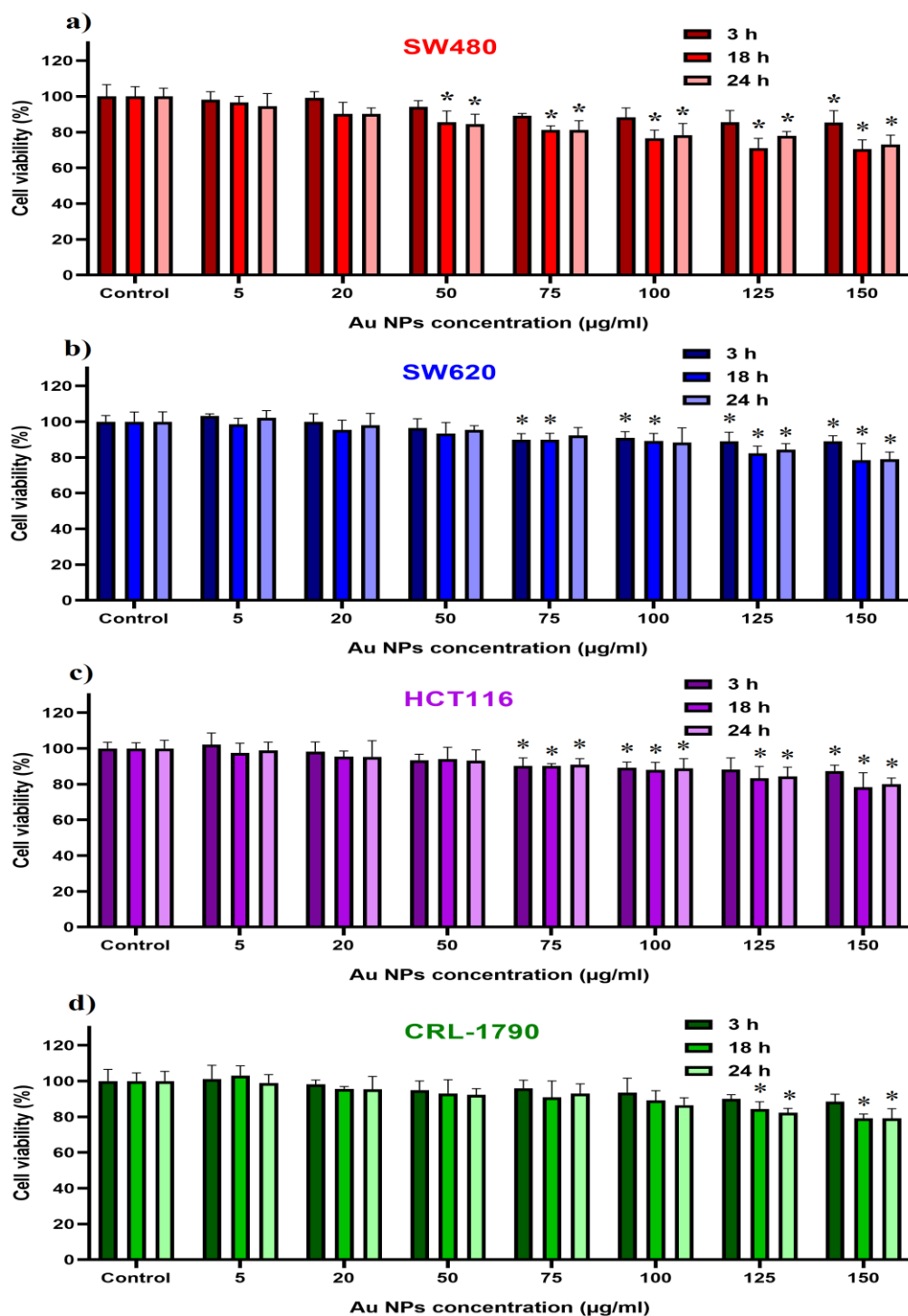
Figure 65. *Cytotoxicity of Au NPs against a) SW480 (red bars), b) SW620 (blue bars), c) HCT116 (violet bars) and d) CRL-1790 (green bars) cells after 3, 18 and 24 h of incubation. Data were considered significant when *p-value < 0.05 vs control.*
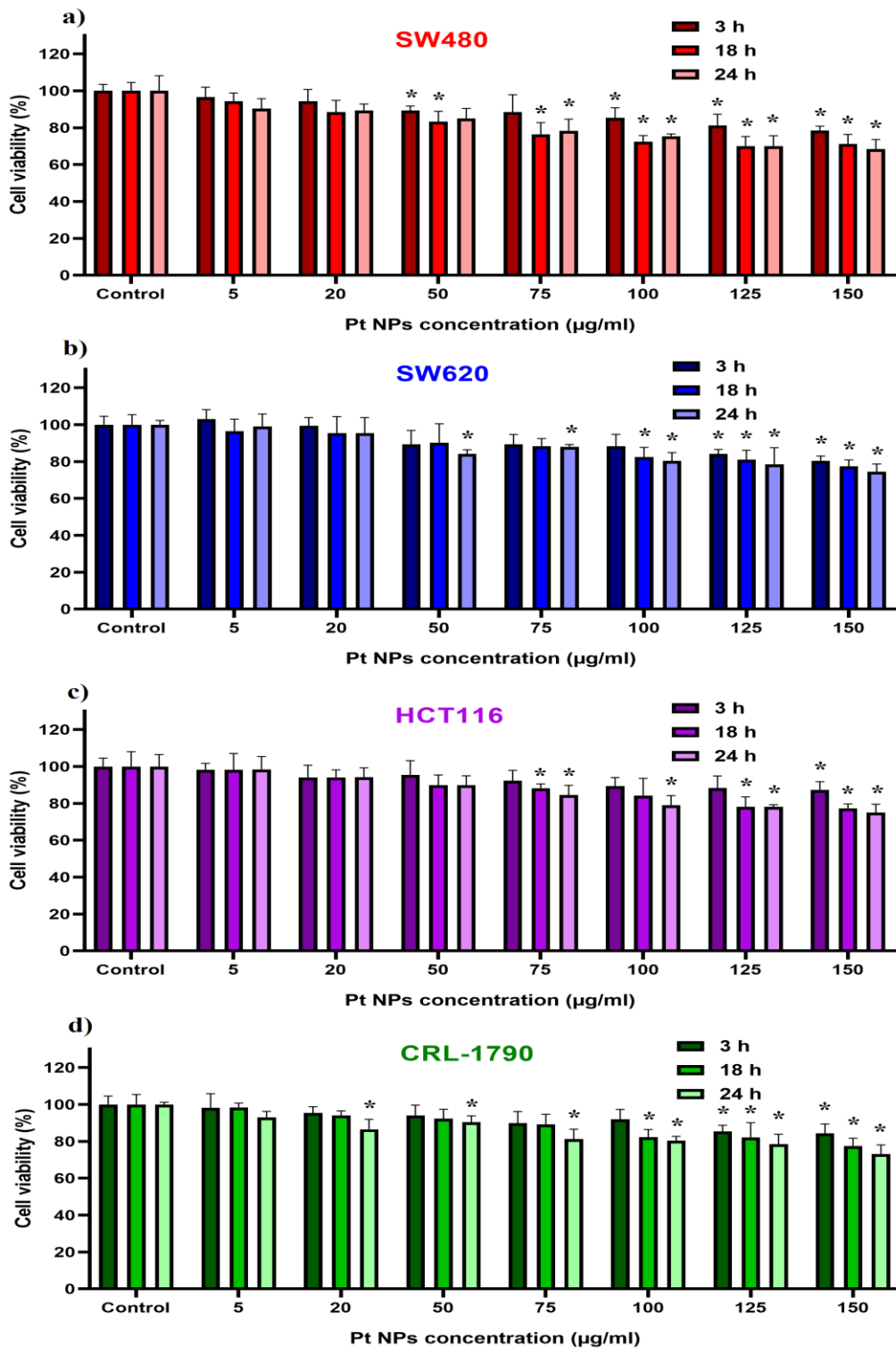
Figure 66. *Cytotoxicity of Pt NPs against a) SW480 (red bars), b) SW620 (blue bars), c) HCT116 (violet bars) and d) CRL-1790 (green bars) cells after 3, 18 and 24 h of incubation. Data were considered significant when *p-value < 0.05 vs control.*
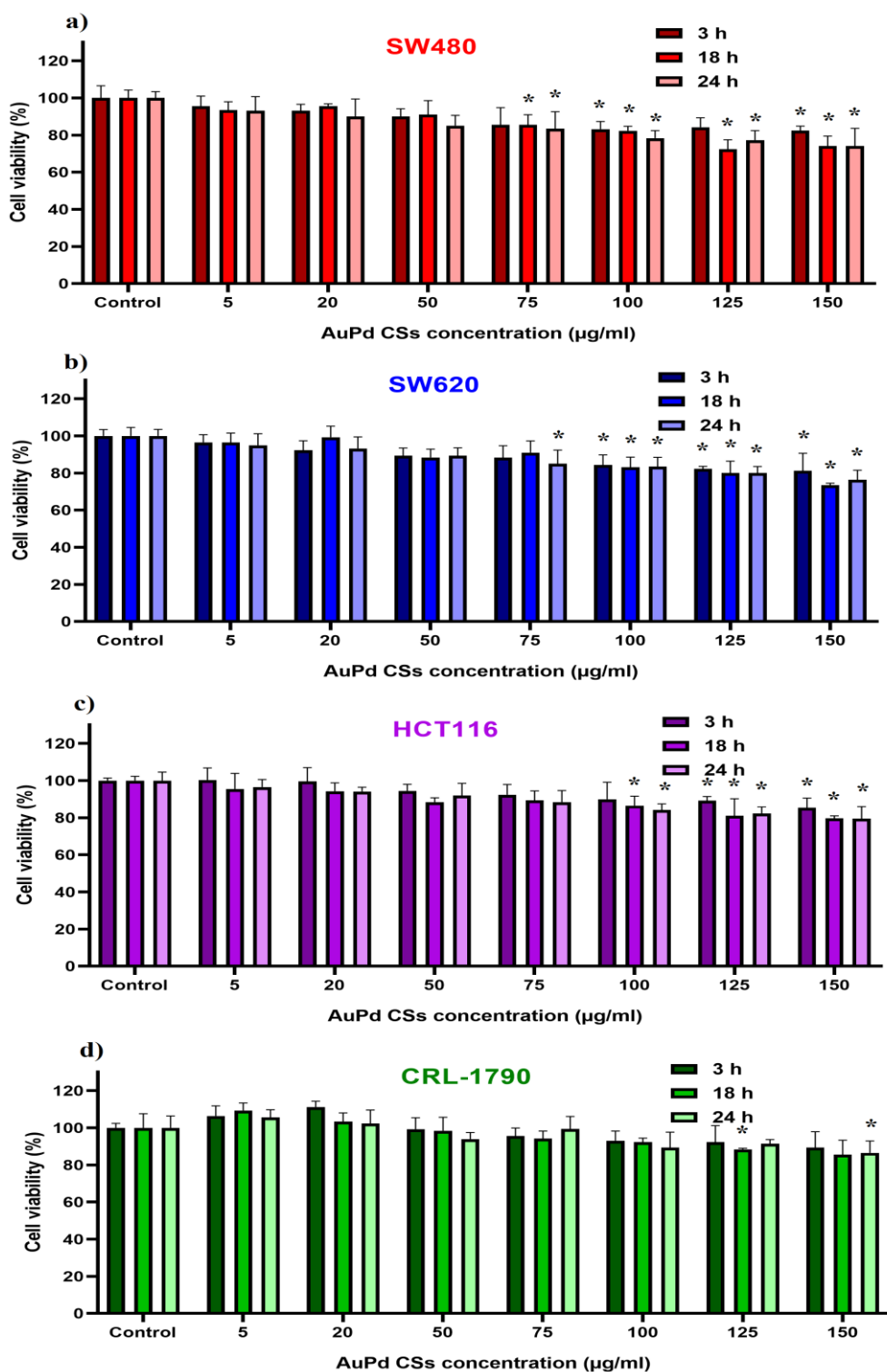
Figure 67. *Cytotoxicity of AuPd CSs against a) SW480 (red bars), b) SW620 (blue bars), c) HCT116 (violet bars) and d) CRL-1790 (green bars) cells after 3, 18 and 24 h of incubation. Data were considered significant when *p-value < 0.05 vs control.*
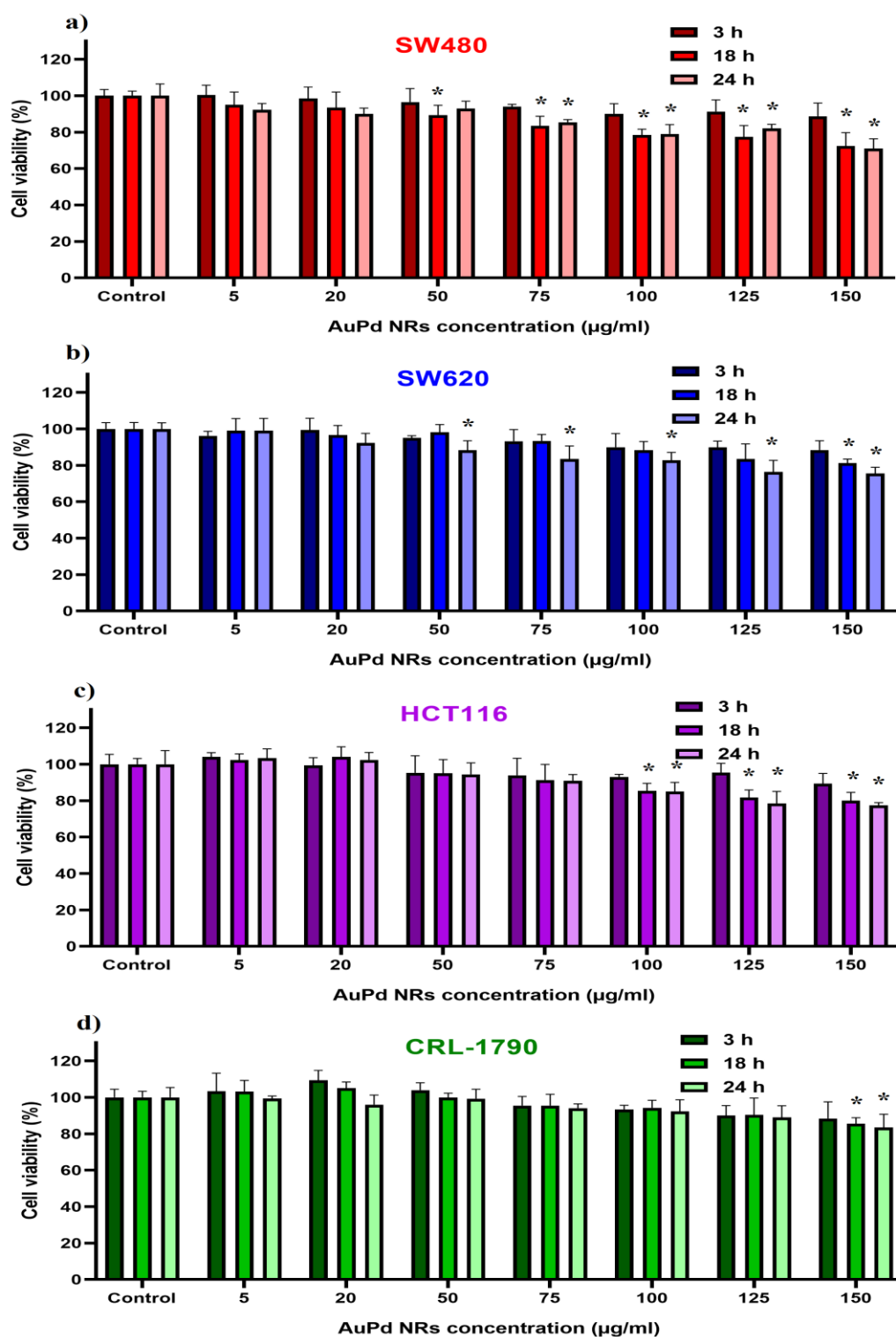
Figure 68. *Cytotoxicity of AuPd NRs against a) SW480 (red bars), b) SW620 (blue bars), c) HCT116 (violet bars) and d) CRL-1790 (green bars) cells after 3, 18 and 24 h of incubation. Data were considered significant when *p-value < 0.05 vs control.*
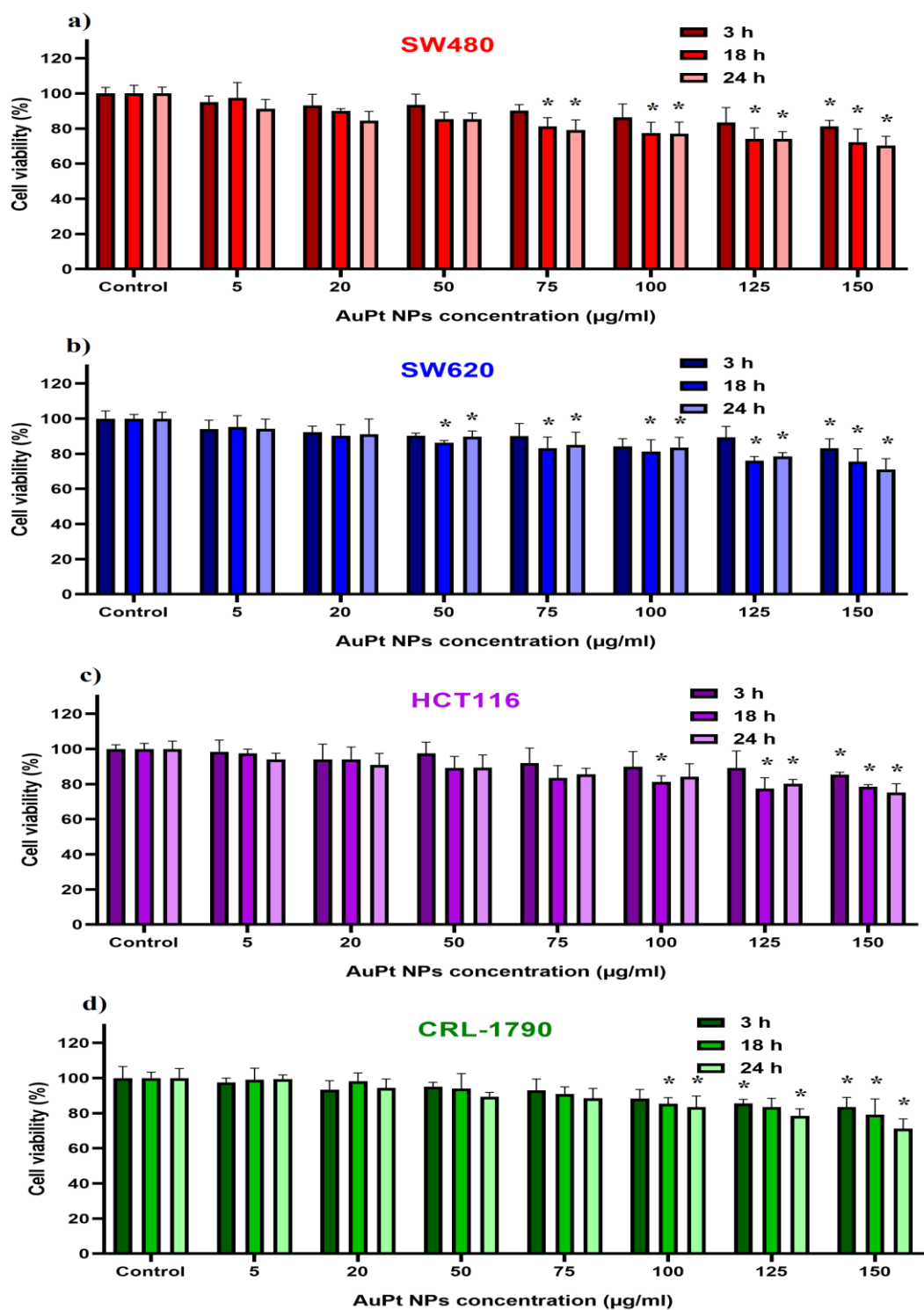
Figure 69. *Cytotoxicity of AuPt NPs against a) SW480 (red bars), b) SW620 (blue bars), c) HCT116 (violet bars) and d) CRL-1790 (green bars) cells after 3, 18 and 24 h of incubation. Data were considered significant when *p-value < 0.05 vs control.*
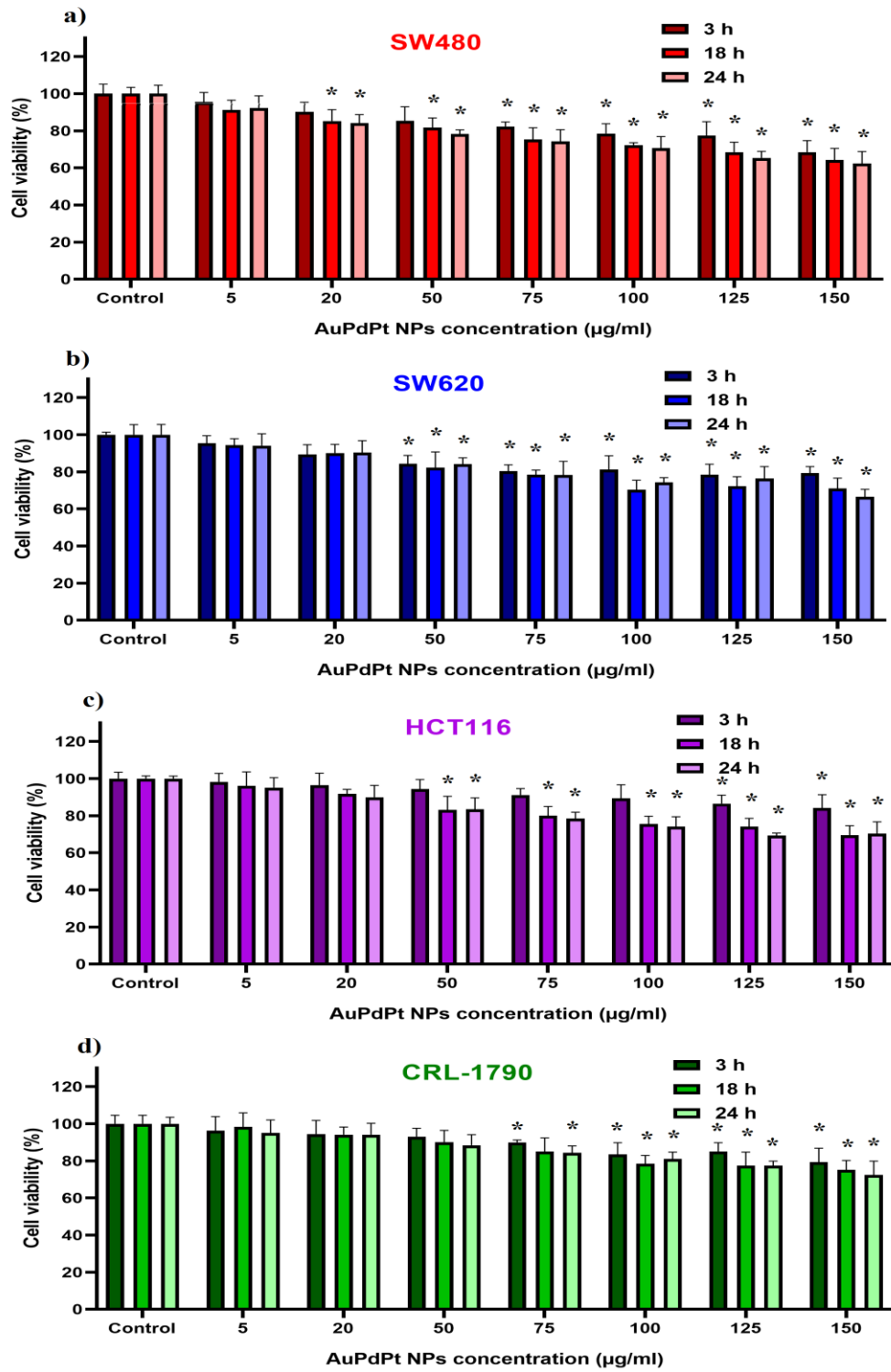
Figure 70. *Cytotoxicity of AuPdPt NPs against a) SW480 (red bars), b) SW620 (blue bars), c) HCT116 (violet bars) and d) CRL-1790 (green bars) cells after 3, 18 and 24 h of incubation. Data were considered significant when *p-value < 0.05 vs control.*
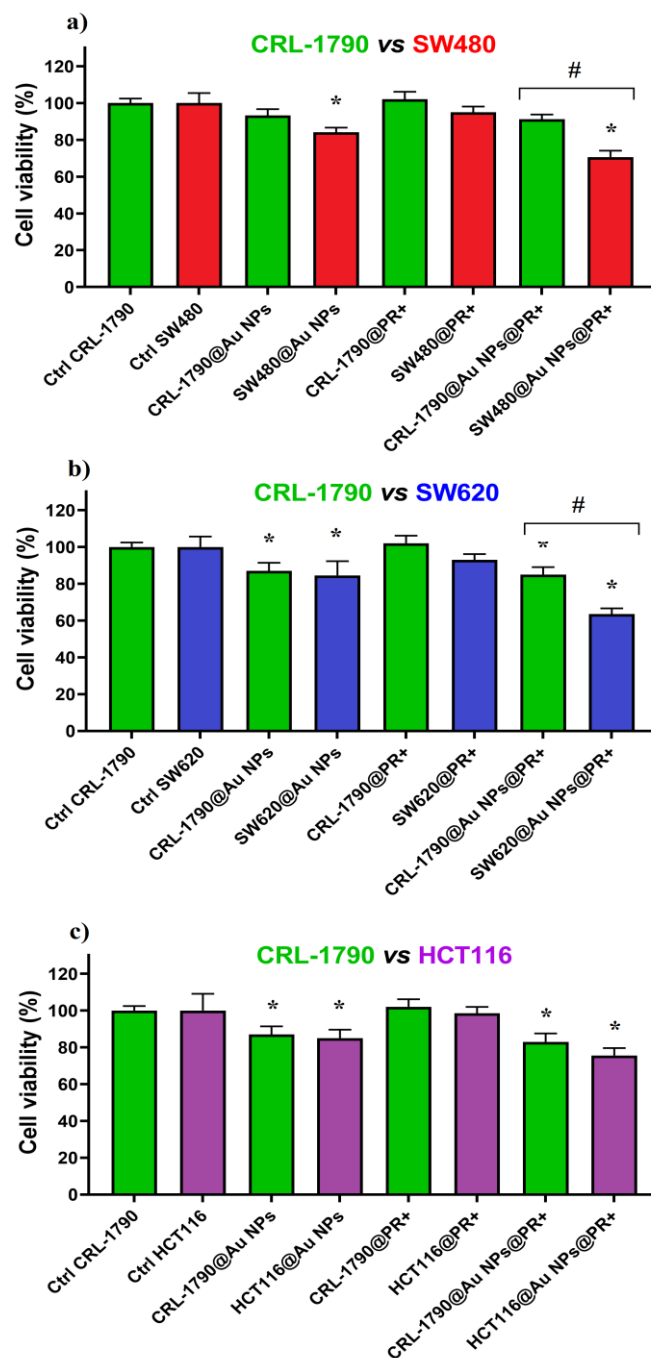
Figure 71. *The MTS assay assessed viability of a) SW480 (red bars), b) SW620 (blue bars) and c) HCT116 (violet bars) cancer cells compared to the viability of CRL-1790 normal colon epithelium cells (green bars) after their incubation with Au NPs and PIr (total dose of 15 Gy). The MTS test was performed after 18 h of cell irradiation, which was preceded by 3 h culture of cells with non-toxic NPs concentration. Data were considered significant if *p-value < 0.05 vs control and #p-value < 0.05 – statistically significant differences between the respective cancer and normal cells.*
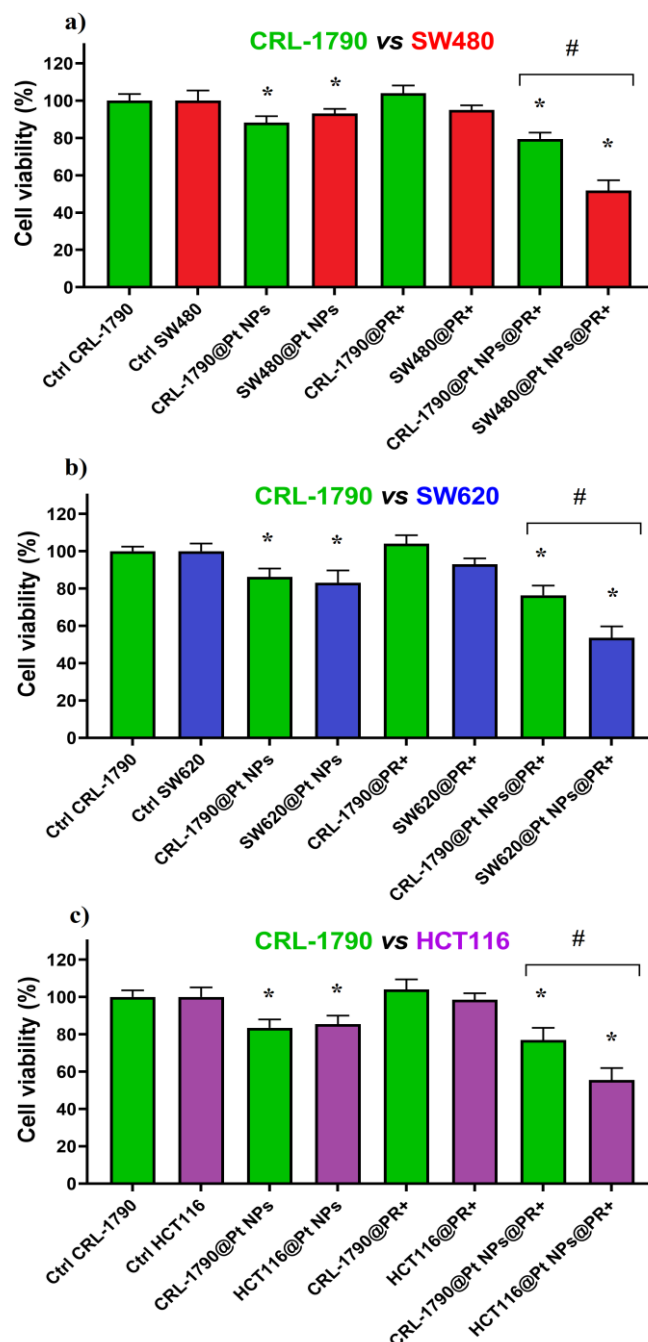
Figure 72. *The MTS assay assessed viability of a) SW480 (red bars), b) SW620 (blue bars) and c) HCT116 (violet bars) cancer cells compared to the viability of CRL-1790 normal colon epithelium cells (green bars) after their incubation with Pt NPs and PIr (total dose of 15 Gy). The MTS test was performed after 18 h of cell irradiation, which was preceded by 3 h culture of cells with non-toxic NPs concentration. Data were considered significant if *p-value < 0.05 vs control and #p-value < 0.05 – statistically significant differences between the respective cancer and normal cells.*
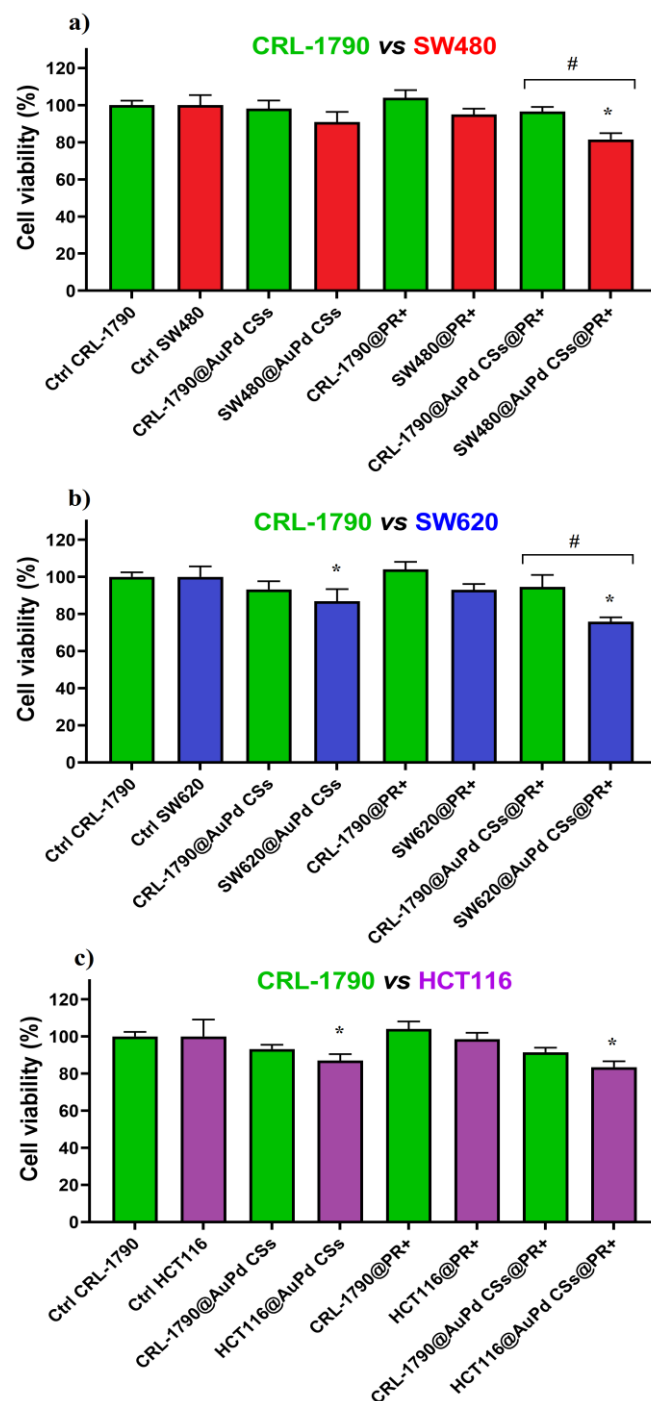
Figure 73. *The MTS assay assessed viability of a) SW480 (red bars), b) SW620 (blue bars) and c) HCT116 (violet bars) cancer cells compared to the viability of CRL-1790 normal colon epithelium cells (green bars) after their incubation with AuPd CSs and PIr (total dose of 15 Gy). The MTS test was performed after 18 h of cell irradiation, which was preceded by 3 h culture of cells with non-toxic NPs concentration. Data were considered significant if *p-value < 0.05 vs control and #p-value < 0.05 – statistically significant differences between the respective cancer and normal cells.*
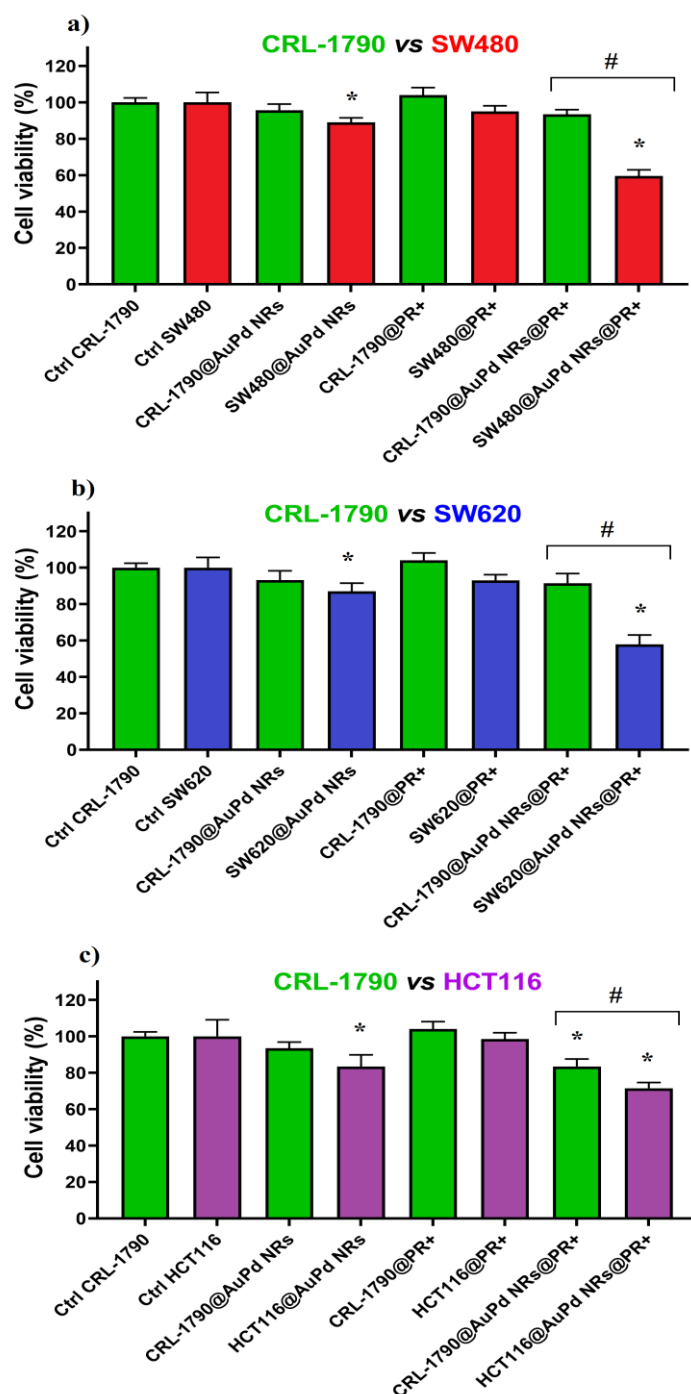
Figure 74. *The MTS assay assessed viability of a) SW480 (red bars), b) SW620 (blue bars) and c) HCT116 (violet bars) cancer cells compared to the viability of CRL-1790 normal colon epithelium cells (green bars) after their incubation with AuPd NRs and PIr (total dose of 15 Gy). The MTS test was performed after 18 h of cell irradiation, which was preceded by 3 h culture of cells with non-toxic NPs concentration. Data were considered significant if *p-value < 0.05 vs control and #p-value < 0.05 – statistically significant differences between the respective cancer and normal cells.*
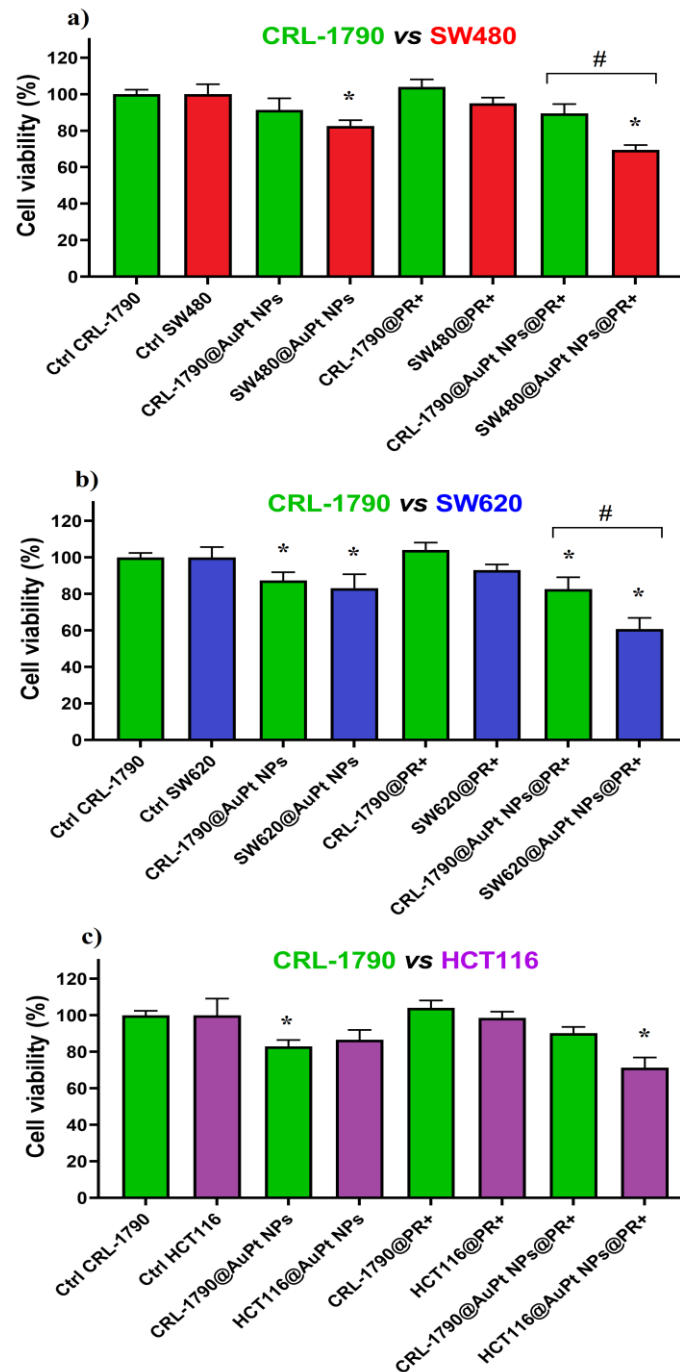
Figure 75. *The MTS assay assessed viability of a) SW480 (red bars), b) SW620 (blue bars) and c) HCT116 (violet bars) cancer cells compared to the viability of CRL-1790 normal colon epithelium cells (green bars) after their incubation with AuPt NPs and PIr (total dose of 15 Gy). The MTS test was performed after 18 h of cell irradiation, which was preceded by 3 h culture of cells with non-toxic NPs concentration. Data were considered significant if *p-value < 0.05 vs control and #p-value < 0.05 – statistically significant differences between the respective cancer and normal cells.*
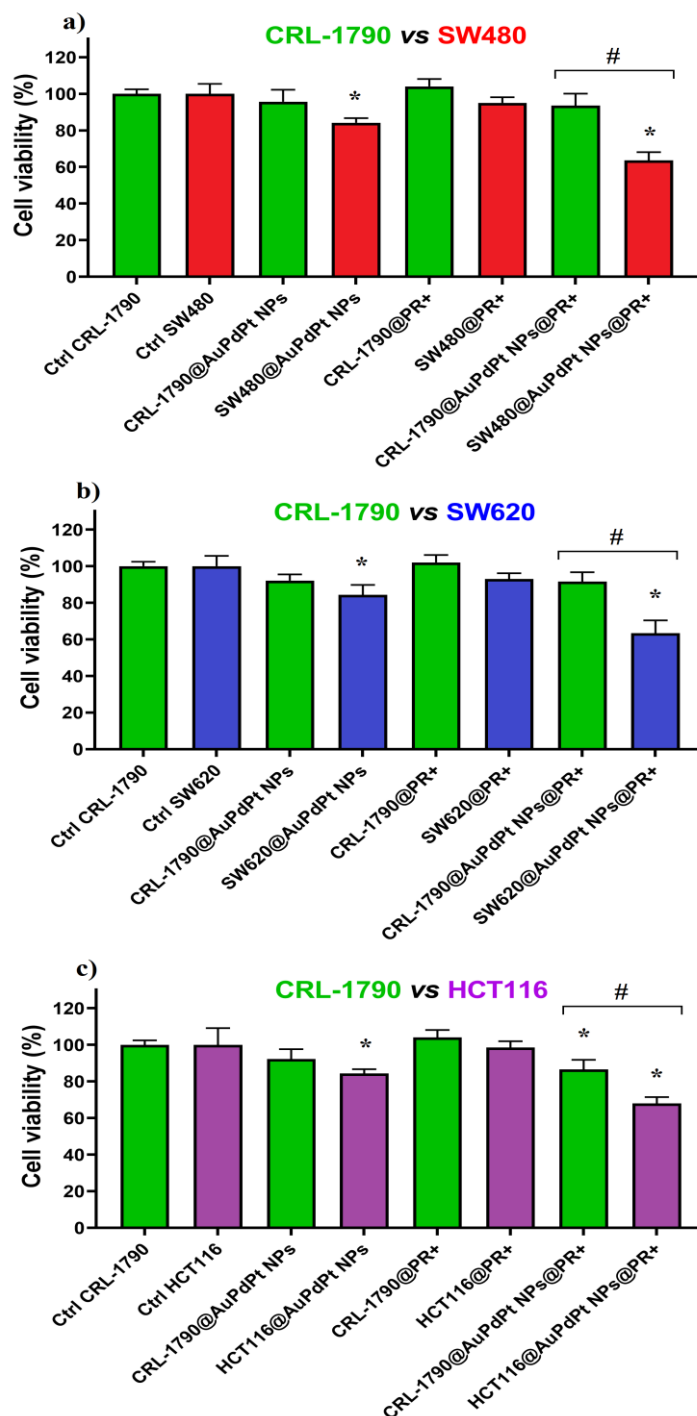
Figure 76. *The MTS assay assessed viability of a) SW480 (red bars), b) SW620 (blue bars) and c) HCT116 (violet bars) cancer cells compared to the viability of CRL-1790 normal colon epithelium cells (green bars) after their incubation with AuPdPt NPs and PIr (total dose of 15 Gy). The MTS test was performed after 18 h of cell irradiation, which was preceded by 3 h culture of cells with non-toxic NPs concentration. Data were considered significant if *p-value < 0.05 vs control and #p-value < 0.05 – statistically significant differences between the respective cancer and normal cells.*

2) Annexin-V binding test – detailed results
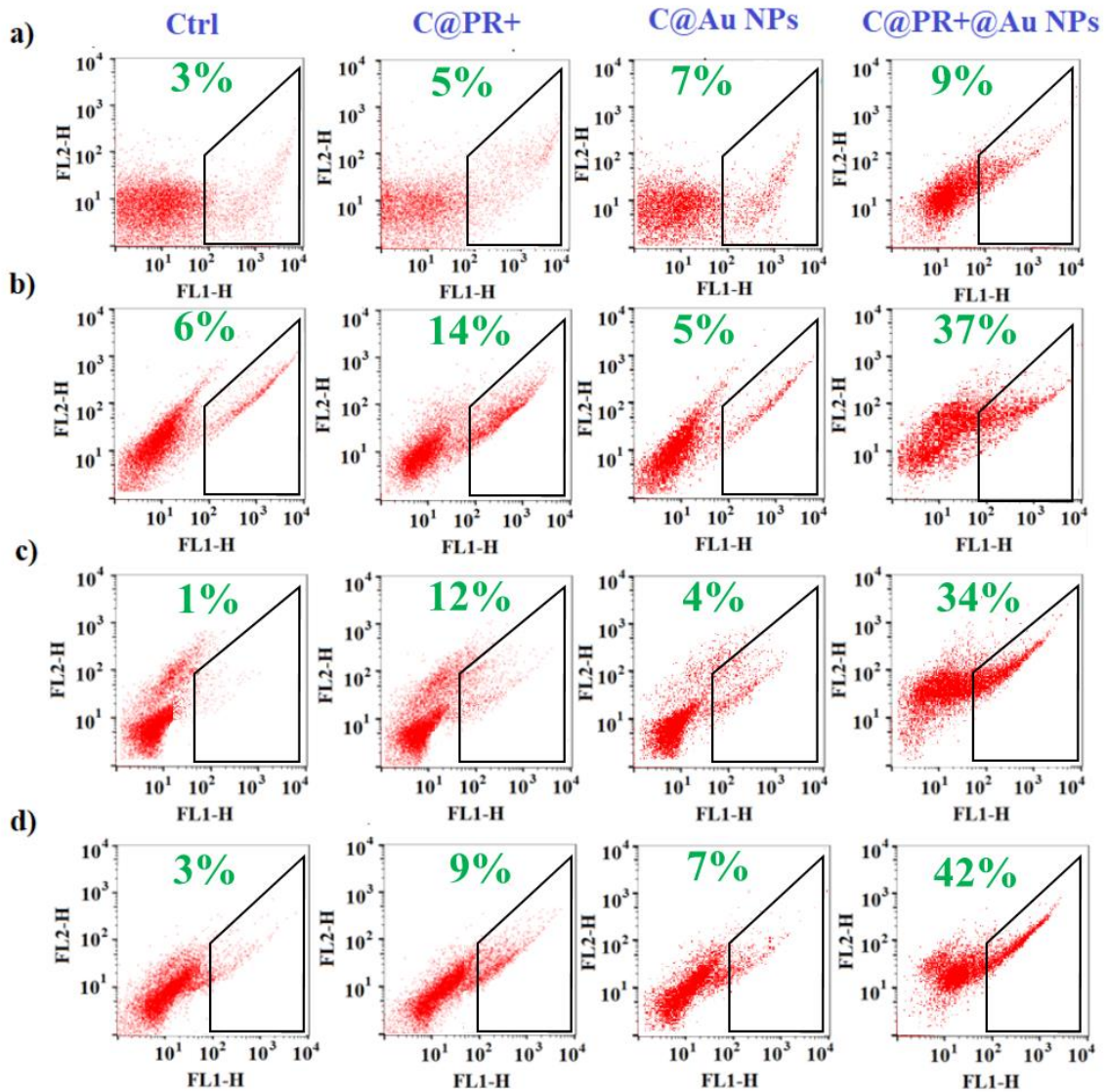
Figure 77. *Flow cytometry analysis of Annexin-V binding by a) CRL-1790, b) SW480, c) SW620 and d) HCT116 cells after addition of Au NPs, followed by PIr. Dot plots FL1-H (green fluorescence) vs FL2-H (red fluorescence) show percent of apoptotic cells (green).*
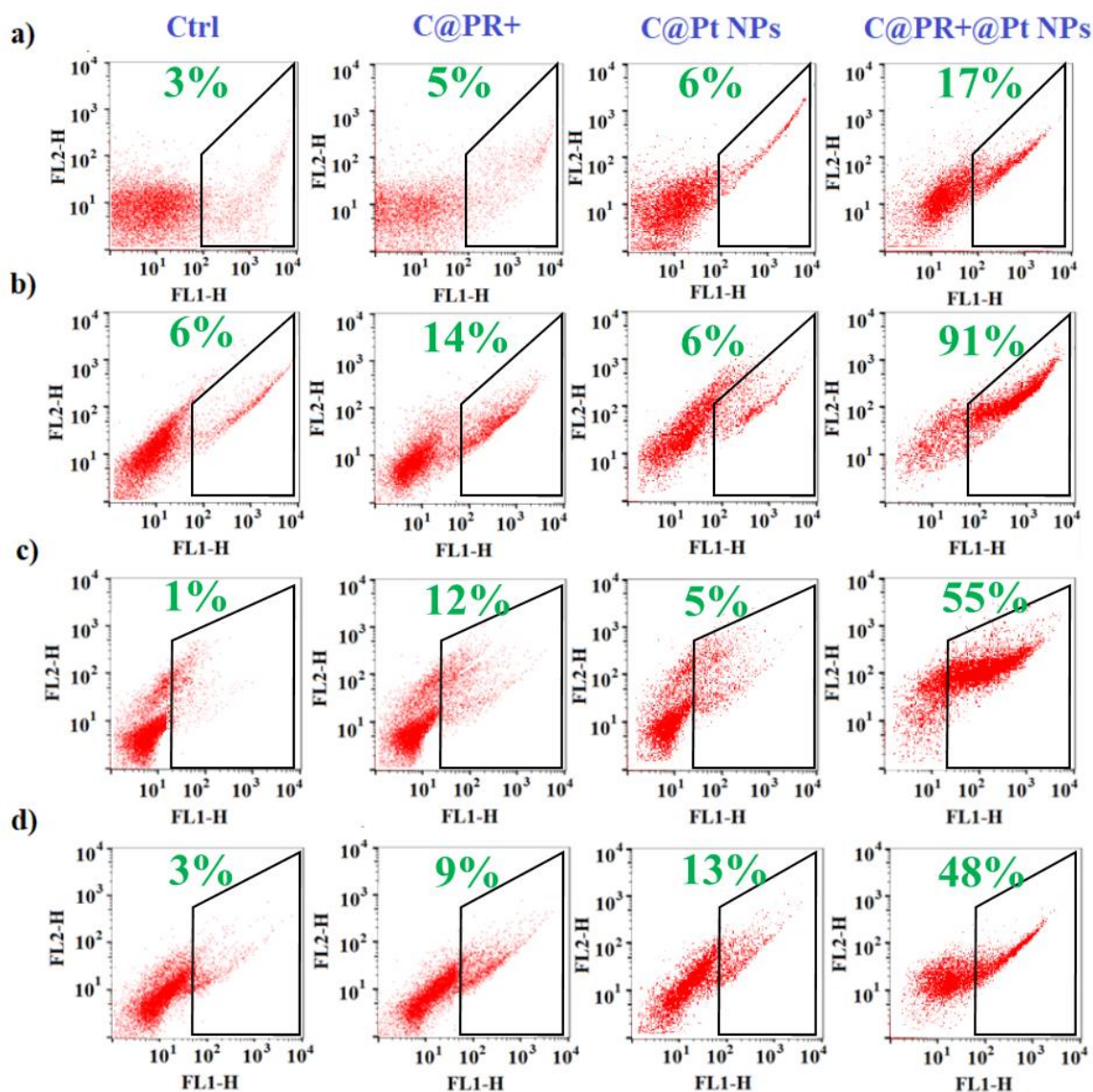
Figure 78. *Flow cytometry analysis of Annexin-V binding by a) CRL-1790, b) SW480, c) SW620 and d) HCT116 cells after addition of Pt NPs, followed by PIr. Dot plots FL1-H (green fluorescence) vs FL2-H (red fluorescence) show percent of apoptotic cells (green).*
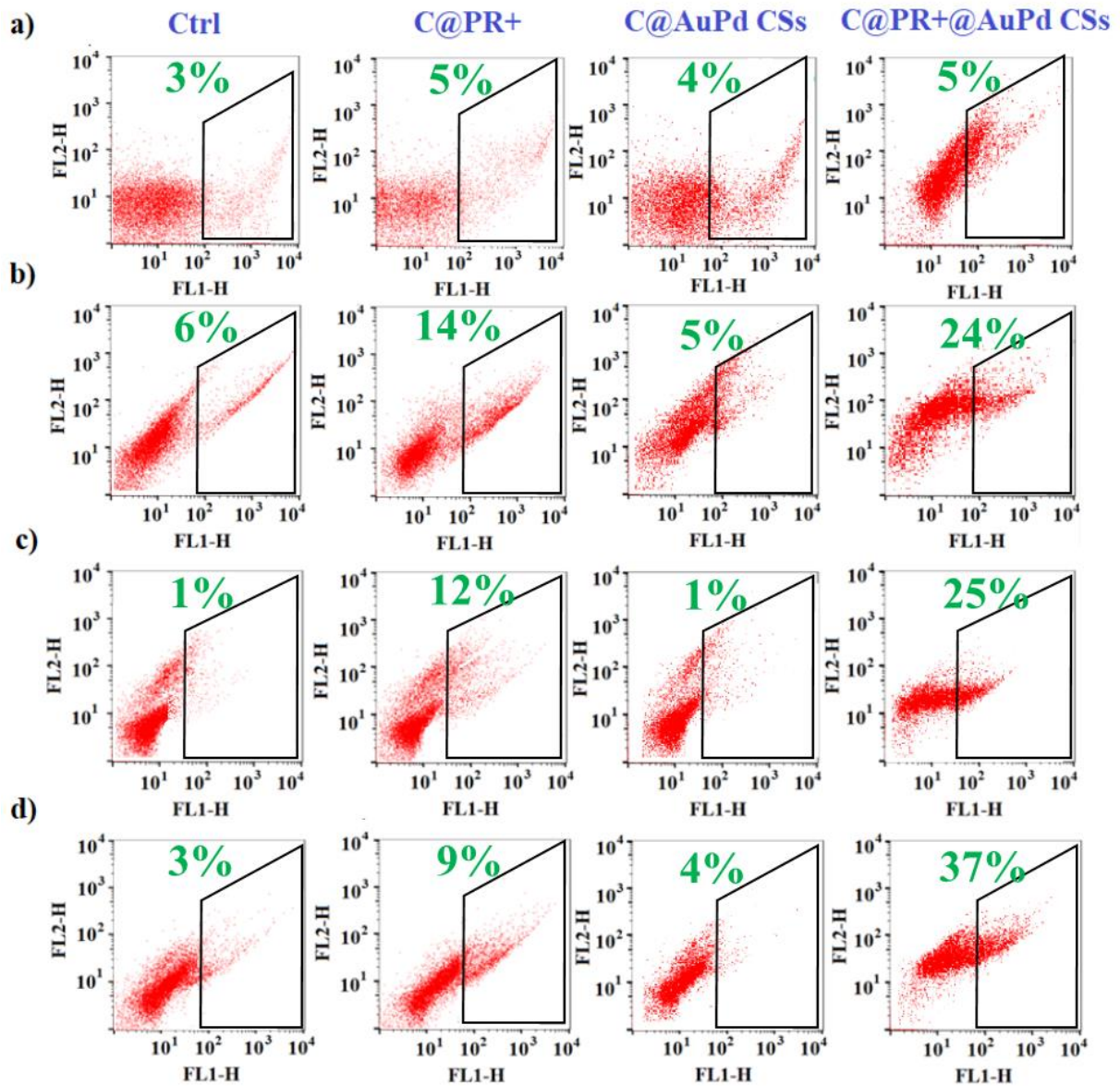
Figure 79. *Flow cytometry analysis of Annexin-V binding by a) CRL-1790, b) SW480, c) SW620 and d) HCT116 cells after addition of AuPd CSs, followed by PIr. Dot plots FL1-H (green fluorescence) vs FL2-H (red fluorescence) show percent of apoptotic cells (green).*
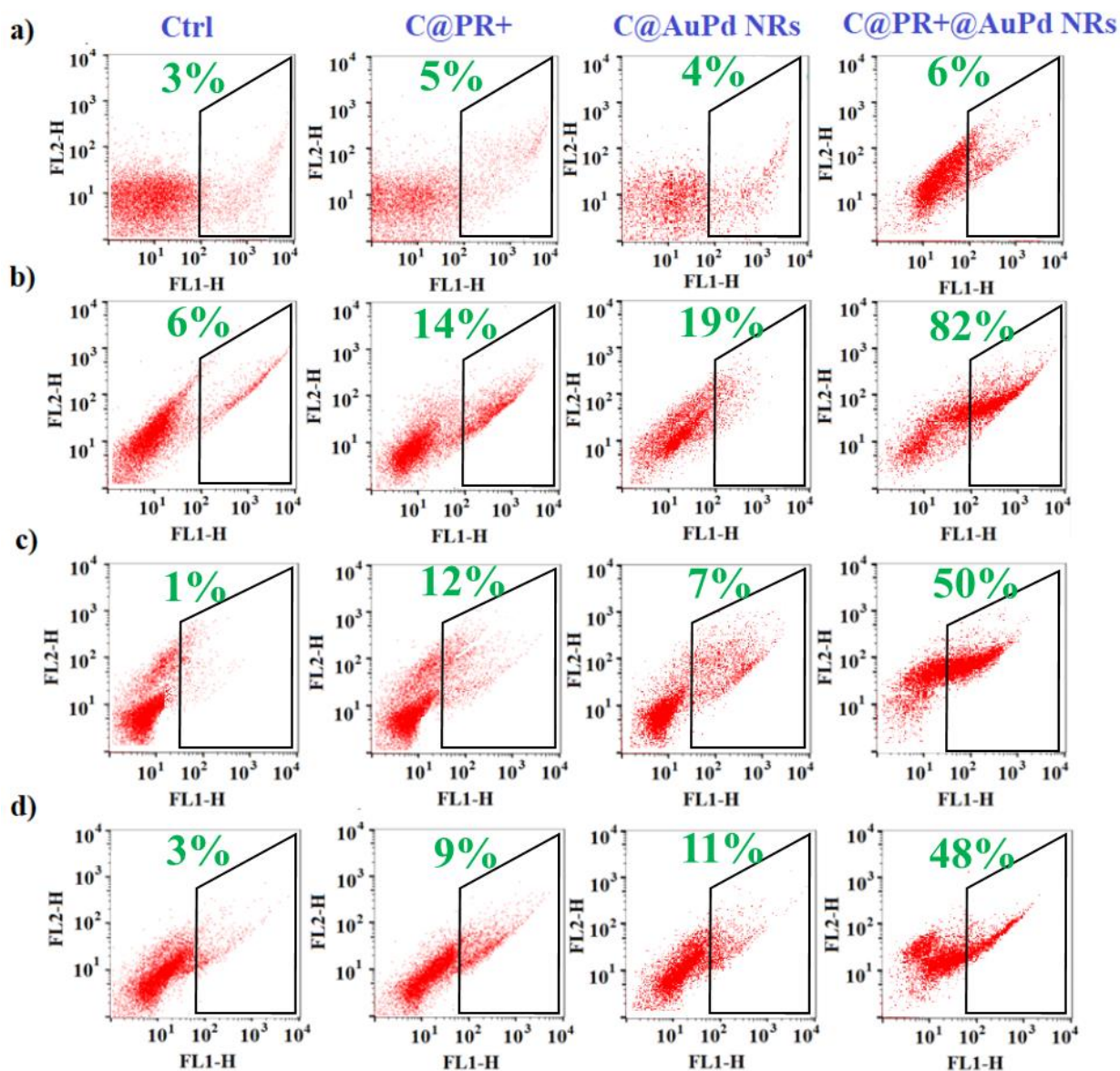
Figure 80. *Flow cytometry analysis of Annexin-V binding by a) CRL-1790, b) SW480, c) SW620 and d) HCT116 cells after addition of AuPd NRs, followed by PIr. Dot plots FL1-H (green fluorescence) vs FL2-H (red fluorescence) show percent of apoptotic cells (green).*
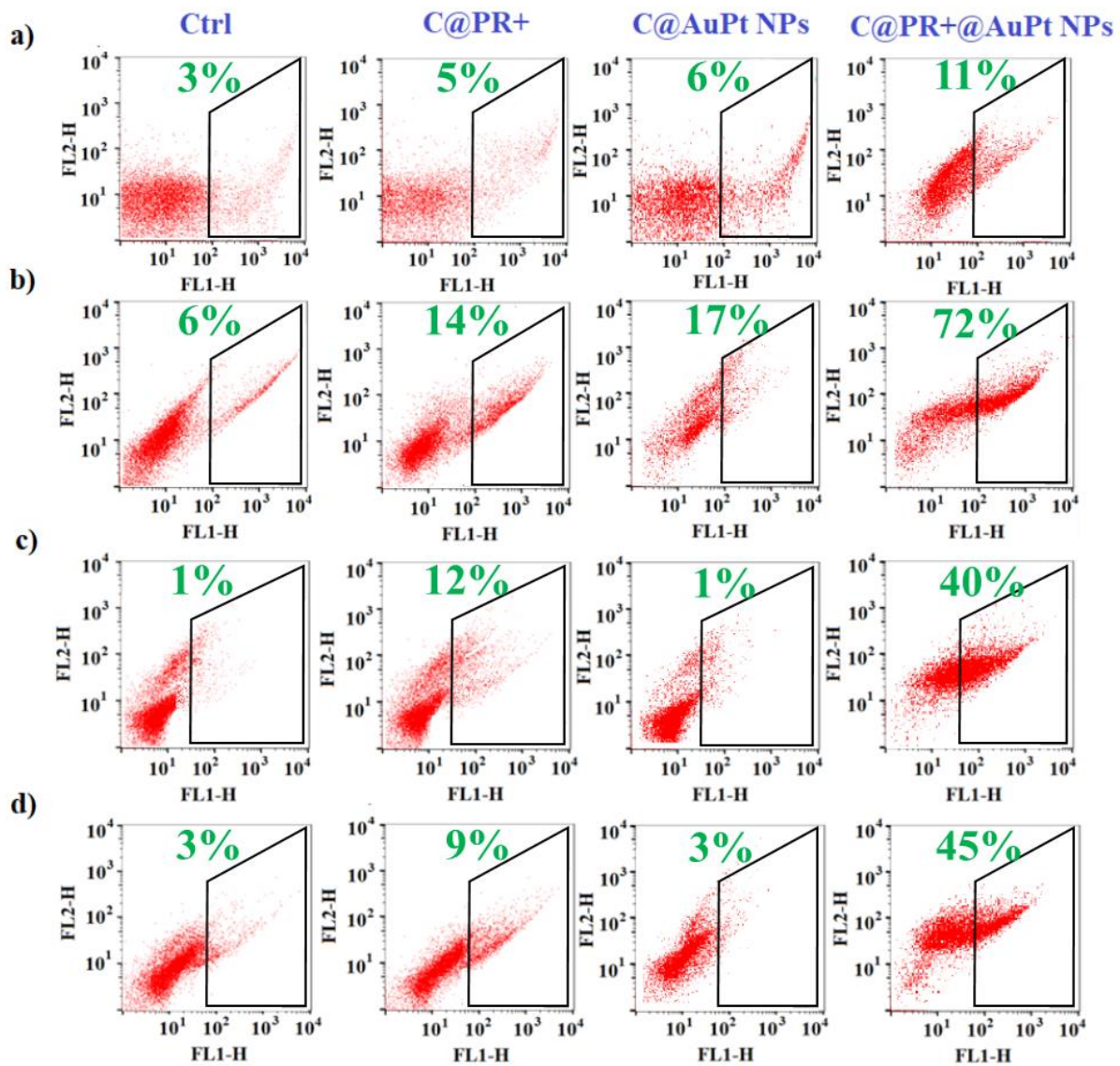
Figure 81. *Flow cytometry analysis of Annexin-V binding by a) CRL-1790, b) SW480, c) SW620 and d) HCT116 cells after addition of AuPt NPs, followed by PIr. Dot plots FL1-H (green fluorescence) vs FL2-H (red fluorescence) show percent of apoptotic cells (green).*
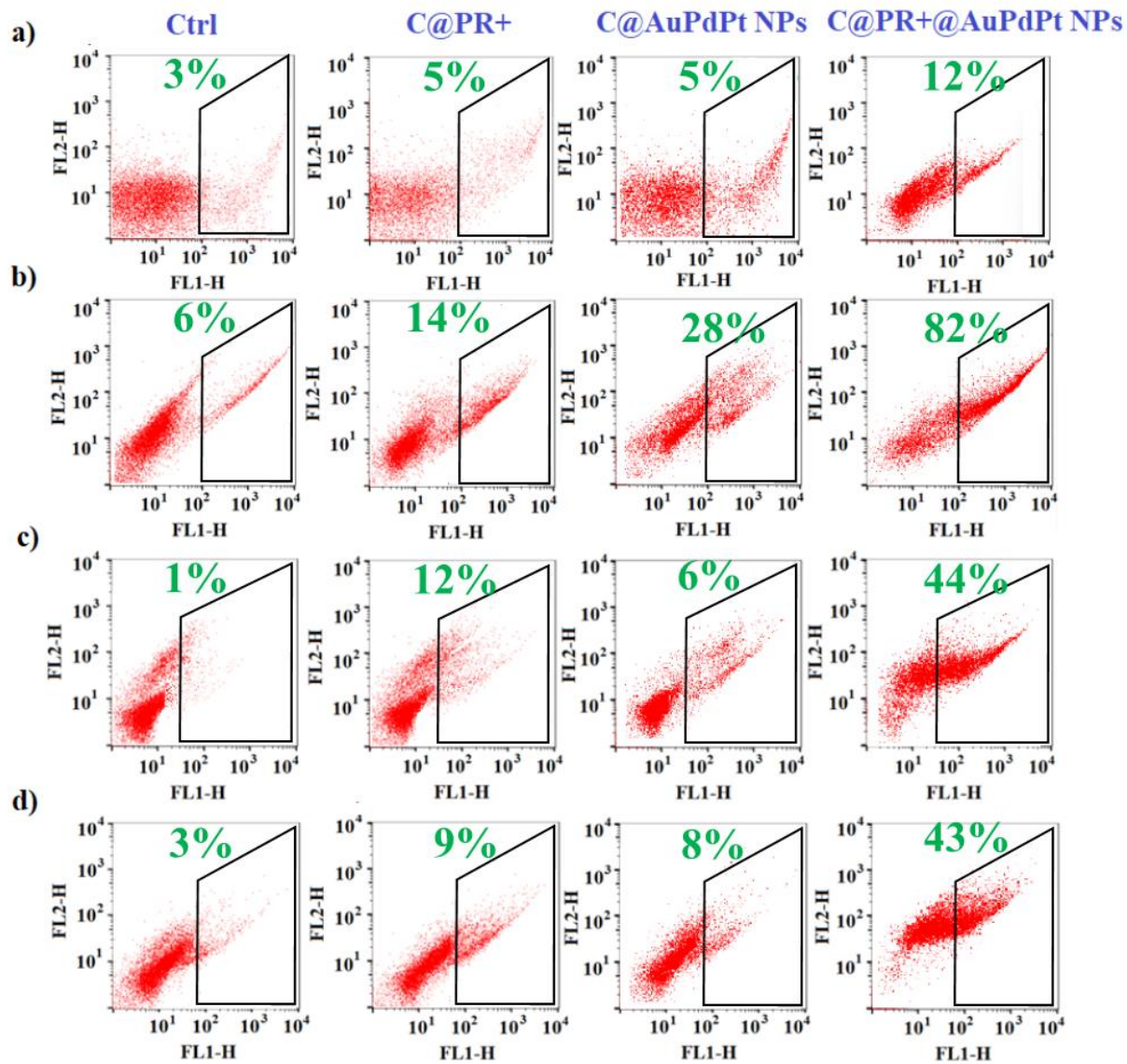
Figure 82. *Flow cytometry analysis of Annexin-V binding by a) CRL-1790, b) SW480, c) SW620 and d) HCT116 cells after addition of AuPdPt NPs, followed by PIr. Dot plots FL1-H (green fluorescence) vs FL2-H (red fluorescence) show percent of apoptotic cells (green).*

3) Impact of NPs on enhancement of the X-ray irradiation effect for selected cancer cells

Table 9. *MTS viability test results for NPs-assisted X-ray irradiation (total dose 15 Gy). Comparison of the survival of normal CRL-1790 (green) and cancer SW480 (red) cell lines.*

	C@NPs	C@X-ray	C@NPs@X-ray
Au NPs	95/85	101/96	82/49
Pt NPs	93/88	101/96	70/33
Pd NPs	93/83	101/96	77/35
AuPt NPs	91/83	101/96	82/51
AuPd CSs	98/91	101/96	91/76
AuPd NRs	96/89	101/96	84/46
AuPdPt NPs	96/84	101/96	82/45

Table 10. *MTS viability test results for NPs-assisted X-ray irradiation (total dose 15 Gy). Comparison of the survival of normal CRL-1790 (green) and cancer SW620 (blue) cell lines.*

	C@NPs	C@X-ray	C@NPs@X-ray
Au NPs	86/83	101/96	75/50
Pt NPs	81/85	101/96	71/31
Pd NPs	90/84	101/96	67/33
AuPt NPs	87/83	101/96	70/40
AuPd CSs	93/87	101/96	82/64
AuPd NRs	93/87	101/96	84/45
AuPdPt NPs	92/84	101/96	85/49

Table 11. *MTS viability test results for NPs-assisted X-ray irradiation (total dose 15 Gy). Comparison of the survival of normal CRL-1790 (green) and cancer HCT116 (violet) cell lines.*

	C@NPs	C@X-ray	C@NPs@X-ray
Au NPs	86/88	101/97	81/66
Pt NPs	81/89	101/97	73/49
Pd NPs	90/84	101/97	73/50
AuPt NPs	82/86	101/97	85/65
AuPd CSs	93/87	101/97	82/77
AuPd NRs	93/83	101/97	70/64
AuPdPt NPs	92/84	101/97	82/61

List of Figures

List of Tables

Scientific output

1) Articles

a) Related to the PhD dissertation

1. **Klębowski B**, Depciuch J, Parlińska-Wojtan M, Baran J. Applications of noble metal-based nanoparticles in medicine. *Int. J. Mol. Sci.* **2018**, *19*(12), E4031, IF = 5.924 (140 pkt).

2. **Klębowski B**, Depciuch J, Stec M, Krzempek D, Komenda W, Baran J, Parlińska-Wojtan M. Fancy-shaped gold-platinum nanocauliflowers for improved proton irradiation effect on colon cancer cells. *Int. J. Mol. Sci.* **2020**, *21*(23), 9610, IF = 5.924 (140 pkt).

3. **Klębowski B**, Stec M, Depciuch J, Pajor-Świerzy A, Baran J, Parlińska-Wojtan M. Gold-decorated platinum and palladium nanoparticles as modern nanocomplexes to improve the effectiveness of simulated anticancer proton therapy. *Pharmaceutics* **2021**, *13*(10), 1726, IF = 6.321 (100 pkt).

4. **Klębowski B.** et al. Does the nanostructure of bimetallic palladium-platinum nanoparticles affect their radiosensitizing properties in anticancer X-ray- and proton radiotherapy? (**in preparation**).

5. **Klębowski B.** et al. Comparison of radiosensitzing properties of individual gold or platinum nanoparticles and the bimetallic Au-Pt nanocomplexes in the *in vitro* model of proton radiotherapy of colon cancer. (**in preparation**).

6. **Klębowski B.** et al. Effectiveness of proton irradiation assisted with gold (Au NPs), palladium (Pd NPs), Au@Pd core-shell and Au-Pd nanoraspberries on colon cancer cell lines (**in preparation**).

b) Other publications

1. Depciuch J, Stec M, **Klębowski B**, Baran J, Parlińska-Wojtan M. Platinum-gold nanoraspberries as effective photosensitizer in anticancer photothermal therapy. *J. Nanobiotechnology* **2019**, *17*(1), 107, IF = 9.151 (140 pkt).

2. Depciuch J, **Klębowski B**, Stec M, Szatanek R, Węglarczyk K, Baj-Krzyworzeka M, Baran J, Parlińska-Wojtan M. Similarities in the chemical composition of colon cancer cells and their microvesicles investigated by spectroscopic methods – potential clinical relevance. *Int. J. Mol. Sci.* **2020**, *21*(5), E1826, IF = 5.924 (140 pkt).

3. Depciuch J, Stec M, **Klębowski B**, Maximenko A, Drzymała E, Baran J, Parlińska-Wojtan M. Size effect of platinum nanoparticles in simulated anticancer photothermal therapy. *Photodiag. Photodyn. Ther.* **2020**, *29*, 101594, IF = 3.631 (70 pkt).

2) Chapters in the book

1. **Klębowski B**, Depciuch J, Baran J, Parlinska-Wojtan M. „An overview of noble-metal nanoparticles in medicine" in: „Current Advances in Chemistry and Biochemistry", 2021, Book Publisher International.

3) Conferences

1. **Klębowski B**, Depciuch J, Baran J, Parlinska-Wojtan M. Złoto-platynowe nanokalafiory jako radiouczulacze w modelu in vitro radioterapii protonowej raka jelita grubego – **oral presentation**. XIII Ogólnokrajowa Konferencja Młodzi Naukowcy w Polsce – Badania i Rozwój, Poznań, 22.03.2021 r.

2. **Klębowski B**, Depciuch J, Baran J, Parlińska-Wojtan M. Synthesis and evaluation of radiosensitizing properties of bimetallic nanoparticles: PtPd core-shell versus PtPd nano-alloy – **oral presentation**. 6th International Symposium on Surface Imaging/Spectroscopy at the Solid/Liquid Interface, Kraków, 6-9.06.2021 r.

3. **Klębowski B**, Depciuch J, Baran J, Parlinska-Wojtan M. Bimetallic gold-decorated platinum and palladium nanoparticles as potential radiosensitizers in proton radiotherapy – **oral presentation**. iNanoTheRad – Advanced strategies for radiotherapy, Paris, 15-17.11.2021 r.

4. **Klębowski B**, Depciuch J, Baran J, Parlinska-Wojtan M. Effect of the palladium shell porosity in bimetallic Au-core Pd-shell nanoparticles on their radiosensitizing properties in anticancer proton radiotherapy– **poster**. 5th International Conference on Applied Surface Science, Palma, the conference will be held on 25-28.04.2022 r.